UNIVERSITY OF CALIFORNIA,
IRVINE

Investigation of Atomization and Combustion Performance of Renewable Biofuels and the
Effects of Ethanol Blending in Biodiesel

THESIS

submitted in partial satisfaction of the requirements for the degree of

MASTER OF SCIENCE

in Mechanical and Aerospace Engineering

by

Adam Gregory Silver

Thesis Committee:
Professor G. Scott Samuelsen, Chair
Professor Derek Dunn-Rankin
Adjunct Professor Vincent McDonell

2015

UMI Number: 1586185

UMI

Dissertation Publishing

UMI 1586185

ProQuest

ProQuest LLC.
789 East Eisenhower Parkway
P.O. Box 1346
Ann Arbor, MI 48106 - 1346

www.manaraa.com

Table of Contents

List of Figures

List of Tables

Nomenclature and Symbols

ULSD – Ultra-low Sulfur Diesel

B99 – 99% Biodiesel, 1% Diesel Fuel

GHG – Greenhouse Gases

NO_x - Oxides of Nitrogen

CO – Carbon Monoxide

CO_2 – Carbon

PM – Particulate Matter

O_3 – Ozone

EPA – Environmental Protection Agency

UHC – Unburned Hydrocarbons

SMD – Sauter Mean Diameter

D32 – Sauter Mean Diameter

D10 – Average Droplet Diameter

ASTM – American Society for Testing and Materials

HRD – Hydrotreated Renewable Diesel

HRJ – Hydrotreated Renewable Jet-Fuel

ALR – Air-to-Liquid Ratio

LVB – Low Velocity Burner

MSGC – Mass Spectroscopy Gas Chromatography

LBOL – Lean Blow Off Limit

ppm – Parts Per Million

DF2 – Distillate fuel number 2

FAA – Fuel Atomizing Air

www.manaraa.com

SI – Spark Ignition

CI – Compression Ignition

PDPA – Phase Doppler Particle Analyzer

LDV – Laser Doppler Velocimetry

CCD – Combustion Chamber Deposits

Greek Symbols

Φ – Equivalence Ratio

σ –Surface Tension

ρ – Density

μ - Viscosity

ΔP_{FAA} – Fuel Atomizing Air Differential Pressure Drop

η_C – Combustion Efficiency

$\dot{m}$ - Mass Flow Rate

$\dot{\forall}$ - Volumetric Flow Rate

Units

K – Kelvin

μm – micron (1×10^{-6} m)

kPa – Kilopascals

mol – Mole

psid – pounds per square inch, differential

Subscripts

A – Air

L – Liquid

R – Relative

Acknowledgements

I would first off like to thank Dr. Vince McDonell for providing guidance through the entirety of my thesis work and for supporting me along the way. His teachings and the opportunities he has provided me with have developed me as a professional engineer and made my graduate experience one not to be taken for granted.

I would also like to thank Dr. Scott Samuelsen for accepting me into the Advanced Power and Energy Program. This institution is marvelous in the way it promotes free thinking and continual learning, and I am extremely grateful to have been a member for so many years. His, as well as Dr. McDonell's and the other directors, all work extensively to make this an exceptional research facility.

The third member of my thesis committee, Dr. Derek Dunn-Rankin, is acknowledged for his support and guidance. I have taken a number of courses with Dr. Dunn-Rankin in which he continually challenges my conventions in order to expand my critical thinking capabilities.

Lastly, I must thank my loving fiancé Cassandra Adams, my family, and all my friends at APEP for their support and positive reinforcement through this program.

Abstract of the Thesis

Experimental Investigation of Atomization and Combustion Performance of Renewable Fuels
and Biodiesel-Ethanol Blends

By

Adam Gregory Silver

Master of Science in Mechanical and Aerospace Engineering

University of California, Irvine, 2015

Professor Scott Samuelsen, Chair

This thesis presents results from an experimental investigation of the macroscopic and microscopic atomization and combustion behavior of B99 biodiesel, ethanol, B99-ethanol blends, methanol, and an F-76-Algae biodiesel blend. In addition, conventional F-76 and Diesel #2 sprays were characterized as a base case to compare with. The physical properties and chemical composition of each fuel were measured in order to characterize and predict atomization performance. A variety of B99-ethanol fuel blends were used which demonstrate a tradeoff between lower density, surface tension, and viscosity with a decrease in the air to liquid ratio. A plain jet air-blast atomizer was used for both non-reacting and reacting tests. The flow rates for the alternative fuels were set by matching the power input provided by the baseline fossil fuels in order to simulate use as a drop in replacement. For this study, phase Doppler interferometry is employed to gain information on drop size, SMD, velocity, and volume flux distribution across the spray plume. A high speed camera is used to gather high speed cinematography of the sprays for observing breakup characteristics and providing additional insight. Reacting flow tests captured NO_x, CO, and UHC emissions along with high speed footage used to predict soot levels based on flame luminosity. The results illustrate how the fuel type impacts the atomization and

spray characteristics. The air-blast atomizer resulted in similar atomization performance among the DF2, F-76, and the F-76/Algae blend. While methanol and ethanol are not suitable candidates for this air-blast configuration and B99 produces significantly larger droplets, the addition of ethanol decreased drop sizes for all B99-ethanol blends by approximately 5 microns. In regards to reacting conditions, increased ethanol blending to B99 consistently lowered NO_x emissions while decreasing combustion efficiency. Overall, lower NO_x and CO emissions were achieved with the fuel blends than with conventional diesels, while the neat biofuels emitted overall less NO_x per CO than the baseline fuels. This research clearly demonstrated that blends of two renewable fuels (B99 and ethanol improved (1) atomization and (2) emissions performance for the burner studied when compared to the baseline fossil fuels DF2 and F-76.

1. Introduction

1.1.   Overview

In the last century worldwide energy consumption has increased 17-fold, bringing with it continuously increasing levels of atmospheric pollutants such as CO_2, CO, SO_2, and NO_x. Concerns over adverse health impacts and ecological damage associated with such emissions has led to a number of anti-pollution regulations such as the US Clean Air Act of 1963 and its subsequent amendments which introduced standards to regulate vehicle emissions and the combustion of high sulfur coal. As of 2012, 83.6% of the total energy consumed by the United States was produced from fossil fuel combustion such as coal, oil, petroleum, and natural gas products and oil products provide 93% of the energy demand for the transportation sector (Agency 2014). Since the beginning of modern motored transportation when gasoline transitioned from being a byproduct of kerosene production to the driving force in the U.S. petroleum industry, the growth and development of oil production has been ever increasing. In 2012, the world demand for oil was placed at 89.2 million barrels of oil per day. This demand is equivalent to 43,400 gallons per second, roughly the discharge rate of a moderate sized rive such as the Charles or Connecticut Rivers in the northeast United States. Within the United States, 46% (by volume) of supplied oil is converted to gasoline, while 31% is used in manufacturing middle distillates such as diesel fuel, jet fuel, and fuel oils (EIA, 2014a).

Increased demand on these fossil fuels impacts human health and the environment and drives a need to explore alternative energy sources. Biologically derived fuels show feasibility in not only shifting the dependence of fossil fuels to a renewable source, but also in providing energy at a lower cost to the environment. Although climate change is usually the main topic of

1

concern, other environmental concerns need to be addressed. The development of a large biofuel industry could have consequences on land and water usage, as well as other environmental concerns that cannot be neglected if overall sustainability is the true end goal. The use of biofuels not only present challenges from an operability standpoint, but these fuels also include their own obstacles to large-scale commercial production and economic feasibility, namely the lifecycle levels of greenhouse gas (GHG) reductions. Life cycle analysis is a technique used to assess the environmental impacts of all stages of a product's life, including raw material extraction, processing, manufacturing, distribution, use, and disposal or recycling. Sources of feedstocks play a crucial role, where CARB reports average GHG reductions for soybean derived biodiesels at 57% and 21% reductions from corn derived ethanol. Contrary to this, ethanol derived from sugarcane and switchgrass provide average GHG reductions of 61% and 110%, respectively (U.S. DOE 2015). Innovative solutions are constantly emerging that provide more effective renewable pathways for various renewable fuels. For instance, advanced methods are emerging that enable use of existing production facilities to produce chemically similar fuels to conventional fuels. One method includes hydro-processing of vegetable oils to yield jet and diesel fuel alternatives.

Biofuels have previously been considered for their applications in reciprocating internal combustion engines. Recently more work is being done on expanding the use of renewable fuels into use in gas turbine systems for transportation. As energy from renewable sources such as solar, wind, geothermal, and hydroelectric penetrate the market, these sources generally are not well suited for transportation purposes. Typically, transportation vehicles such as those in aviation and marine applications prefer to carry energy-dense liquid fuels in order to provide power for use over long distances.

Renewable fuels such as methanol, ethanol, and biodiesel have received attention. However, all of these renewable fuels exhibit relatively significant different physical properties (viscosity, density, surface, tension, etc.) that affect their atomization performance compared to the traditional fossil fuel. Biodiesel exhibits difficulty during cold start due to its crystallizing property at low temperatures. In addition, pump and filter life in the biodiesel fuel system is shortened due to long term storage issues as unsaturated components present in biodiesels lead to susceptibility of oxidative degradations (Christensen & McCormick 2014). Even with these weak points, numerous attempts have been made to use biodiesel in reciprocating engines because of its low emission characteristics (Kim, Suh et al., 2008). The feasibility of using biofuels in gas turbine systems is heavily dependent on meeting strict air quality standards for carbon monoxide, oxides of nitrogen, oxides of sulfur, and hydrocarbons (Board 2010). While studies have been done on biodiesels, emission results are inconsistent. Most studies show increased levels in CO with varying NO_x outputs. However, oxygen present in biodiesels is often cited as an important factor in promoting more complete combustion (Legg, McDonell et al 2010). With improved atomization, gas turbines operating on biodiesels can realize improved emissions as compared to those using conventional diesel.

The most limiting factor in biodiesel atomization is the relative increase in dynamic viscosity and surface tension. Both of these fluid properties are heavily tied to atomization behavior in that the increased viscosity and surface tension limit droplet breakup and lead to larger average droplet sizes which in turn increase residence time and NO_x formation. Although there are other modes of improving emissions, improved fuel injector design and mixing has been shown to reduce NO_x, CO, and HC outputs (Bryden 2011). Among the noted efforts to achieve improved atomization, ethanol is regarded as a viable option as a fuel additive. Ethanol

3

is derived from the fermentation of sucrose from either sugar cane or corn and is a well-established and understood biofuel. On its own, ethanol has demonstrated lower emissions, but has only 63% the heating value of diesel, presenting its own challenges. The decreased emissions from ethanol are partly due to its superior atomization quality as compared to that of diesel. Biodiesels on their own present their own benefits and drawbacks, but it is speculated that blending with ethanol can create a more ideal fuel possessing advantages associated with each fuel. In terms of making biodiesel a more viable fuel, this makes blending an advantageous GHG reductions strategy if using ethanol derived from feedstocks other than corn.

Currently, more research is required in order to develop new designs to accommodate and optimize the performance for these relatively new fuels. While more optimal designs are under development, the use of biofuels in existing gas turbines is already taking place, and the current performance levels can still be improved upon in an effort to make the use of renewable liquid fuels more commonplace.

1.2.   Goal

The goal of this thesis is to establish the viability of various alternative fuels as replacements for baseline fossil fuels (F-76 and DF2) in the context of atomization and combustion performance. The alternative fuels of interest include B99, ethanol, methanol, and an algae-derived HRD (F-76/Algae) blend, in addition to B99-ethanol blended fuels.

1.3.   Objectives

In order to achieve this goal, the following steps will be taken:

1. Select renewable fuels of interest according to background information regarding the status and prominence of each.

4

2. Determine the fluid properties of the fuels under investigation.

3. Create a test bed with diagnostic tools for data collection.

4. Conduct non-reacting experiments for a variety of test conditions.

5. Contrast data with empirical models to gain insight on observed phenomena.

6. Test each fuel in a reacting flow situation.

7. Optimize biofuel performance by determining ideal fuel blending ratios.

2. Background

2.1.   Gas Turbines Review

The conventional gas turbine system operates on the principles of the Brayton cycle. In this process, air is drawn into a compressor where both the pressure and temperature of the gas increases. The next step involves adding in and combusting a fuel with the air. The fuel combustion drastically increases the temperature of the working fluid. The combustor is one of the most challenging components in a gas turbine to design; it has to mix the air and fuel, ignite the mixture, and control the temperature distribution to the exit section. Traditional combustors are comprised of three main operation zones, as depicted in Figure 1.
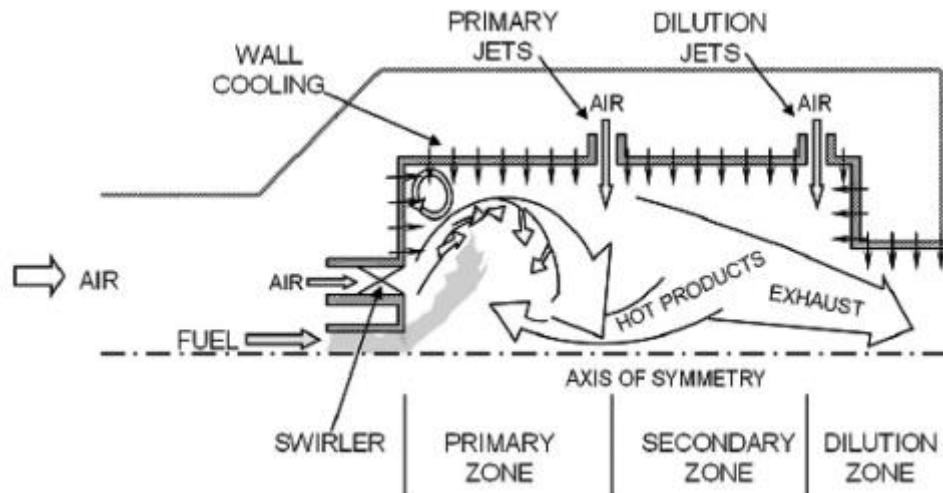
Figure 1: Traditional Combustor Cross-Section (U.S. DOE 2006)

In the primary zone, air enters via a swirler creating a low pressure recirculation region along the centerline. Most of the combustion reaction takes place here as the fuel is ignited by the existing reaction. Primary air jets enter the combustion zone through ports in the wall that help to restrict the flame to within the primary zone. Typically the primary zone operate at a fuel rich condition ($\Phi > 1.0$). The products then enter the secondary reaction zone where CO is oxidized to CO_2 by

adding more fuel and reducing the global equivalence ratio to $\Phi < 0.8$. In the dilution zone, compressor discharge air is added to the combustion products to control the profile of the temperature as they enter the turbine nozzle. From then, the thermal energy is extracted and converted into either thrust using a nozzle (for aero applications), or electrical energy via driving a rotating shaft of a generator (ground based applications). In real applications, gas turbines must satisfy a range of operation requirements such as high combustion efficiency, wide stability limits, low emissions of smoke and gaseous pollutant species, and low operation and maintenance costs (Ballal and Lefebvre 2010).

Current gas turbines are found to be increasingly useful in marine and land based transportation applications as compared to reciprocating internal combustion engines. A list of advantages includes: high power-to-weigh ratios, smaller relative sizes, absence of required liquid-cooling systems, good cold start characteristics, and cleaner emissions due to lower equivalence ratios. In addition, robust mechanical design coupled with multipurpose combustion systems make many gas turbine systems "fuel flexible," making them operable on a variety of liquid fuels for a wide range of operability (Gupta, Rehman, et al., 2010). One of the shortcomings of the gas turbine, poor operating efficiency at low loads, a large reason why gas turbines are not used in automobiles, is overcome with integration of co-generation systems. The combined cycle technology simultaneously produces power and thermal energy from energy bound in exhaust gases, greatly increasing the overall efficiency of the system.

The majority of modern turbine systems operate on conventional diesels and various non-renewable fuels. Oil products for use in industrial gas turbines are comprised of heavy distillates and residual oils of different distillate fractions, as well as naphtha. These fuels typically have complex compositions ranging from average chemical formulae of $C_{10}H_{20}$ to $C_{15}H_{28}$. Roughly

7

75% of petroleum-derived diesel is composed of saturated hydrocarbons, primarily n, iso, and cycloparaffins, while the remaining 25% includes aromatic hydrocarbons such as naphthalenes and alkylbenzenes (Agency 1995). Sulfur is included as a natural component in crude oil that if left alone impairs the effectiveness of emission control systems and contributes to air pollution in the form of SO_x. These compounds have been linked to a number of adverse effects on the respiratory system as well as contribute to production of acid rain. EPA's Clean Air Nonroad Diesel Rule phases in ultra-low sulfur diesel (ULSD) for non-road, locomotive, and marine engines from 2007-2014, calling for more stringent fuel preparation techniques such as hydrodesulfurization, oxidation, and adsorption (OTAQ 2012).

Fuels for aviation purposed gas turbines must meet more strict guidelines. For civil aviation, leading guidelines for fuels are safety, cost, reliability, and ease of handling. For military aircraft fuels, cost factors are overtaken by availability, supply logistics, and reliability over a wide range of operation conditions. Jet fuel is composed largely of alkanes, cycloalkanes, aromatics (~25% by volume), olefins (~5% by volume), and small amounts of sulfur compounds comprising less than 4000 ppm (Butnark et al., 2004). Such classes of fuels have between 8 and 16 carbons depending on the feedstock which varies by well location (Belot 2009). This variety makes it unrealistic to define an exact fuel composition standard for a given aviation fuel. As such, specification ranges have been established to evaluate fuels based on their properties and performance. These fuels for must meet strict specifications, which in the United States are ASTM D1655 and D7655 (ASTM, 2009a and ASTM, 2009b). Viable fuels must have an array of characteristics that include:

- High energy density (energy per unit volume), which facilitates long-range flight.

- High specific energy (energy per unit mass), which decreases takeoff weight and improves fuel efficiency.

- High flash point, the temperature above which the fuel produces a vapor that can ignite, which ensures safe operation.

- Low freezing point and vapor pressure, which facilitate safe operation at cruise altitudes.

- High thermal stability, prevents chemical decomposition of the fuel within the gas turbine engine preventing fuel line blockage.

- Adequate lubricity, ensures proper functioning of fuel pumps.

- Sufficient aromatic compound content, ensures adequate seal swell within fuel system to prevent fuel leaks.

These fuel requirements are much softer for ground based turbine fuels geared towards transportation and power generation.

2.2.   F-76 Distillate and Low Sulfur Diesel

Conventional petroleum fuels in use today are derived from crude oil that has been drilled from the earth's surface. As dead organisms accumulated on the bottom of oceans, riverbeds, and swamps they became mixed with and covered by sand and mud. Over time, as subsequent layers accumulated, the resulting heat and pressure on the lower layers transformed the organic material into a dark waxy substance called kerogen. With more time, kerogen molecules decompose into smaller more simple molecules composed solely of carbon and hydrogen. The resultant hydrocarbons formed a range of compounds in gaseous, liquid, and solid forms such as natural gas, petroleum, and solid hydrocarbons having molecular weights of 300 or more. These

9

wide array of hydrocarbons vary greatly in composition, and can include paraffins, cyclo-paraffins, and aromatics (Odgers and Kretschmer 1986). In order to create a useful product, these various hydrocarbon species must be separated, and each component is used for different applications. Crude oil is refined into finished petroleum products through distillation, wherein the raw crude oil is heated and sent into a distillation column. As the oil heats up, different products boil off and are recovered at different temperatures. Lighter products such as butane, liquid petroleum gas, gasoline blending components, and naptha are recovered at the lowest temperatures. Jet fuel, kerosene, and distillates (e.g. home heating oils and diesel fuel) comprise the mid-range products, and heavy products such as residual fuel are recovered at the highest temperatures (U.S. 2012). The two conventional fuels used in this study are ultra-low-sulfur diesel #2, also referred to as DF2, and a naval purposed F-76 military distillate.

In a major effort to reduce SO_x emissions, the Environmental Protection Agency (EPA) has imposed regulations on sulfur content, enabling engine manufacturers to implement advance emissions control systems. Enacted from 2006 – 2010, ULSD specifications limit sulfur content to 15 parts per million (ppm). The F-76 distillate falls under diesels purposed for marine vessels and may contain up to 1000 ppm sulfur (EPA 2012). As these fuels are produced, it is impossible to specify one specific physical and chemical requirement for each type of fuel, hence the American Society for Testing and Materials (ASTM) determines the appropriate ranges for many fuels. Specifications for DF2 and F-76 are listed in the appendix section under ASTM D 975 and ASTM and MIL-DTL-16884L.

2.3.   Atomization

Combustion of liquid fuels in engines is dependent on achieving effective atomization quality. The goal of atomization is to increase the specific surface of the fuel, enabling high rates of mixing and evaporation. In most systems, a reduction in drop size leads to easier light off, wider burning range, higher volumetric heat release, and lower pollutant concentrations in exhaust streams, namely NO_x, CO_2 and UHC since ignitability and flame stability are dependent on the droplet size and air-fuel mixture properties. The mixing mechanism in combustion chambers involve the disintegration of the liquid phase, forming a homogeneous mixture to avoid single droplet combustion and to create an advantageous spatial distribution of the liquid spray within the combustion chamber.

For many applications, it is useful to characterize drop sizes by not only the mean drop size, but by a more representative diameter. In the context of this study, the representative diameter used is termed the Sauter Mean Diameter (SMD), also referred to as D32; it is mathematically represented below with N and D representing the number of droplets and droplet diameter, respectively.

$$\text{SMD} = \frac{\sum N_i D_i^3}{\sum N_i D_i^2} \qquad (2\text{-}1)$$

The SMD is the diameter of a drop whose ratio of volume to surface area is the same as that of the entire spray. Atomization is usually accomplished by ejecting the fuel at high velocity into a relatively slow-moving stream of air, or vice versa. The surface area of a spray before breakup is simply that of the liquid cylinder as the fuel emerges from an orifice. The action of one high velocity fluid impinging on another causes disruptive turbulence and critical shearing of the

liquid, breaking the fluid into smaller droplets. Physical properties (surface tension, viscosity, and density) of both fluids is critical in the atomization process. For one, larger viscosity of the fuel impedes formation of perturbations on the surface sheet caused by turbulent shearing, prolonging the breakup process. Surface tension (μ) is also an important liquid physical property because it represents the force that resists deformation of the liquid jet. Of the three physical properties, density effects are the least significant as most liquids exhibit only minor differences, i.e. the process is dominated by surface tension and viscosity.

2.3.1. Plain Air-blast Atomizer

Air-blast atomizers, identified in Figure 2, are well suited in continuous flow engines such as gas turbines. In this configuration, the liquid jet is exposed to a high velocity stream of air. As the liquid jet leaves the fuel orifice, an annulus of air impinges on the jet to shatter the fuel into ligaments and then drops. Air-blast nozzles differ from air assist nozzles by using a relatively small air flow rate at very high velocities.
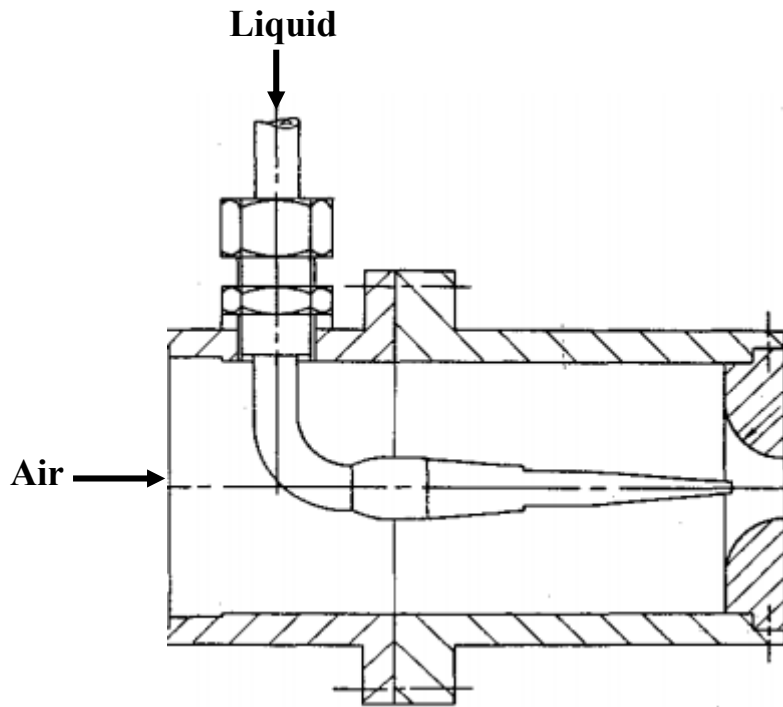
Figure 2: Plain-jet air-blast atomizer (Lefebvre et al., 1977)

Air-blast atomizers have a number of advantages over pressure atomizers, especially in high pressure combustion applications as found in gas turbines. These nozzles produce a finer spray with lower required injection pressures. In this configuration, the atomization process ensures thorough mixing of air and fuel, leading to typically lower soot formation. This is characterized by relatively low flame radiation and minimization of exhaust smoke. Due to the inherit simplicity, the air-blast nozzle lends itself to a wide array of design configurations (Lefebvre 1989). Various designs can be found from literature, such as a) pre-filming, b) piloted, and c) plain jet atomizers as shown in Figure 3.
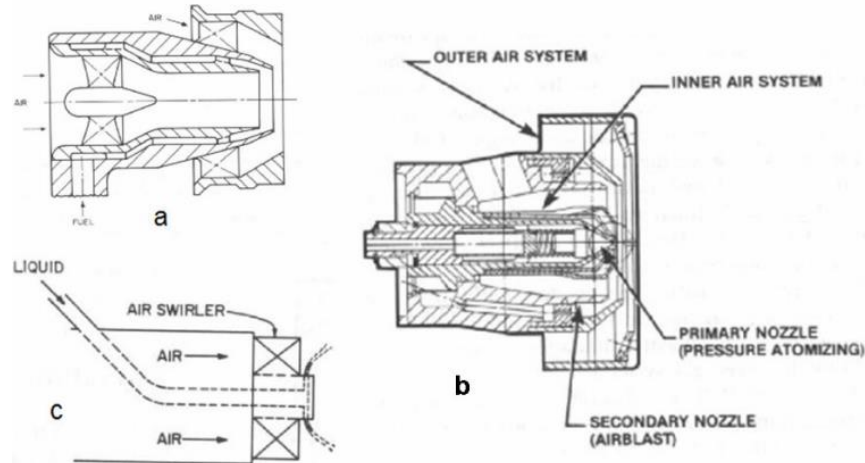
Figure 3: Different Types of Air-blast Atomizers (Lefebvre 1989)

The atomizer featured in Figure 3.a flows the liquid through a number of tangential equally spaced openings onto a pre-filmer before being discharged at the atomization lip where it is impinged by two separate air flows. To overcome the challenge of low air velocities in some designs, a simplex nozzle can be coupled with the air-blast design as shown in Figure 3.b. Lastly, the liquid jet can be introduced directly into the high-velocity swirling air stream shown in Figure 3.c.

2.4. Emissions Control

In recent years, increasing regulatory pressure to drastically reduce emissions continually challenges gas turbine designers to innovate designs required to meet these new legislation requirements. Industry must include designs that minimize a number of harmful emissions species such as nitrogen oxides (NO_x), carbon monoxide (CO), carbon dioxide (CO_2), unburned hydrocarbons (UHC), and soot (PM).

14

Of the listed emissions, NO_x receives a large amount of attention. NO reacts with O_2 in the atmosphere to form NO_2 which is a main contributor to acid rain, causing irritation in mucus membranes such as the eyes, nose, and throat (De Nevers 2000). In addition, NO_x is involved in the formation of photochemical oxidant (smog), and ozone (O_3) which has been linked to respiratory problems such as reduced lung capacity, aggravated asthma, and increased susceptibility to respiratory illness (CARB 2004).

The Environmental Protection Agency notes that CO can cause mild to severe adverse health effects on humans. When inhaled, CO is absorbed into the bloodstream and will combine with hemoglobin to form carboxyhemoglobin (COHb). As CO binds more strongly than O_2 into red blood cells, overall O_2 transport through the bloodstream is inhibited. Chronic exposure to low levels of CO can lead to a number of symptoms including headaches, nausea, vomiting, and fatigue. Fetuses in pregnant mothers are at high risk for CO poisoning and face risks during development (Services 2007).

PM is a mixture of extremely small particles and liquid droplets made up of a number of components such as: nitrates, sulfates, organic chemicals, metals, and soil or dust particles. The size of these particles is directly linked to their health effects. PM_{10}, particulate matter that is 10 micrometers or smaller in diameter, is of concern because it is small enough to pass through the nose and throat and enter the lungs. Numerous studies have linked PM inhalation to a variety of problems including premature death in people with lung or heart disease, nonfatal heart attacks, asthma, other respiratory symptoms. Despite the progress made in the last 30 years, millions of people continue to live in countries with monitored air quality data showing one or more of the common air pollutants (EPA 2012).

The formation of these emission species is well understood and there exist a series of control strategies to mitigate various emissions. NO_x formation occurs by three fundamental mechanisms. The first mechanism, thermal NO_x formation, arises from thermal dissociation and is described by the Zeldovich mechanism

$$O_2 = 2O$$
$$N_2 + O = NO + N$$
$$N + O_2 = NO + O$$
$$N + OH = NO + H$$
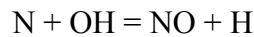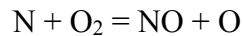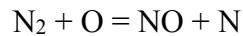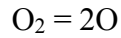
The thermal-NO route is one of the major sources of NO_x in practical combustion systems with flame temperatures exceeding 1800 K.

The second mechanism, the N_2O intermediate mechanism is favored at low equivalence ratios ($\Phi < 0.8$) as found in ground based gas turbine applications.

$$N_2 + O + M \Leftrightarrow N_2O + M$$
$$N_2O + O \Leftrightarrow NO + NO$$
$$N_2O + H \Leftrightarrow NO + NH$$
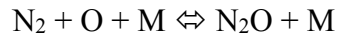
However, N_2O can also react with O and H atoms through alternative channels, and the proper branching of these reactions can be modeled.

$$N_2O + O \Leftrightarrow N_2 + O_2$$
$$N_2O + H \Leftrightarrow N_2 + OH$$

In prompt-NO formation, smaller hydrocarbon radicals such as CH are available to react with molecular N_2; this is noted as the Fenimore mechanism. This reaction occurs close to the burner surface in smaller residence time scales than for the thermal pathway.

$$N_2 + CH \Leftrightarrow HCN + N$$

$$N_2 + CH \Leftrightarrow NHC + H$$

$$NCN + OH \Leftrightarrow NO + HCN$$

$$NCN + O \Leftrightarrow NO + CN$$

$$N_2 + C \Leftrightarrow CN + N$$
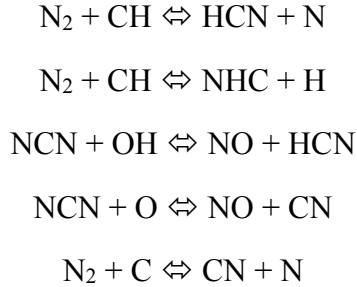
The key points in controlling NO_x lie with respect to thermal NO production as this is the main mode of NO formation in lean combustion environments as investigated in this study. Thermal NO is controlled largely by flame temperature, or equivalence ratio, and NO increases with residence time for most practical combustors. In addition, fuel atomization, along with equivalence ratio, is linked to NO formation. Figure 4 illustrates that NO emissions increase with an increase in SMD, especially at low equivalence ratios.
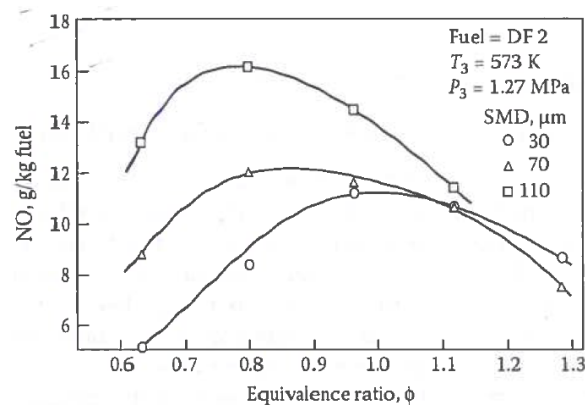
Figure 4: Influence of fuel atomization on NO emissions (Rink, Lefebvre 1989)

Larger droplets in the flame can support "envelope" flames in which the entire droplet surface is engulfed in flame, creating a local diffusion burning region at near stoichiometric air/fuel ratios. These stoichiometric conditions produce high temperatures in which NO_x is formed in appreciable quantities.

In the study of carbon monoxide production, it is crucial to couple the oxidation of CO and hydrocarbons. Hydrocarbon combustion can be characterized by a simple two set process:

17

the breakdown of fuel to CO, then the oxidation of CO to CO_2. CO oxidation is a relatively slow

process, which can be accelerated with the presence of hydrogen species such as H_2O or H_2.

Assuming water is the primary source for hydrogen, the following steps describe the oxidation of

CO:

$$CO + O_2 \rightarrow CO_2 + O$$
$$O + H_2O \rightarrow OH + OH$$
$$CO + OH \rightarrow CO_2 + H$$
$$H + O_2 \rightarrow OH + O$$

The chemical reactions involving the oxidation of CO are exothermic, meaning that left

over CO found in exhaust streams is essentially wasted fuel bound energy, constituting a drop in

the combustion efficiency. CO production is largely influenced by the amount of wall cooling

air used in the combustion zone. Some CO formed in the primary combustion zone can migrate

towards the wall and become entrained in the wall-cooling air. The relative temperature of this

air is so relatively low that the oxidation reaction essentially freezes. UHC production precedes

early CO formation during the initial reaction stages where long H-C chains decay into more

simple species. Like CO, UHC found in exhaust also constitute as remnants of incomplete

combustion. CO and UHC emissions are reduced by redistributing the airflow to bring the

primary-zone equivalence ratio close to $\Phi = .8$, increase the primary-zone residence time, reduce

airflow to the line wall-cooling air, and improve fuel atomization as seen in Figure 5. CO and

UHC production is linked to mean droplet size due to influence of volume required for fuel

evaporation. During the droplet evaporation and combustion stage, a significant portion of the

total combustion volume is occupied in fuel evaporation, meaning there is less available volume

for the chemical reaction to take place in (Ballal, Lefebvre 2010).
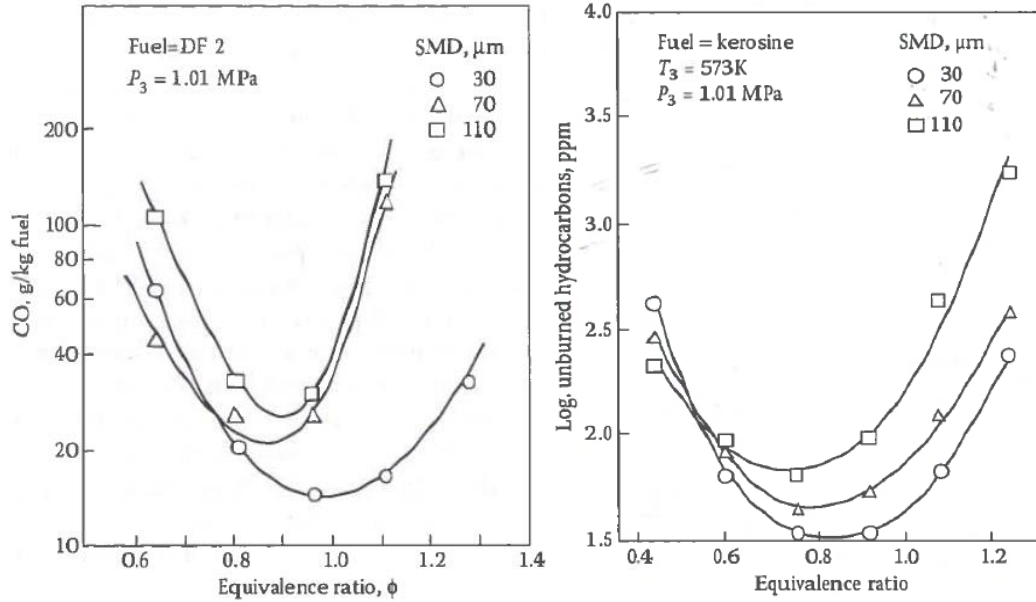
Figure 5: Influence of fuel atomization on CO (L) and UHC (R) emissions (Rink, Lefebvre 1989)

PM, also known as soot, is frequently present in hydrocarbon flames, giving out the typical orange or yellow appearance. With sufficient time, soot is formed on the fuel side of the reaction zone and consumed as enters an oxygen rich zone. Figure 6 illustrates the locations of soot formation and destruction zones in a simple jet flame.
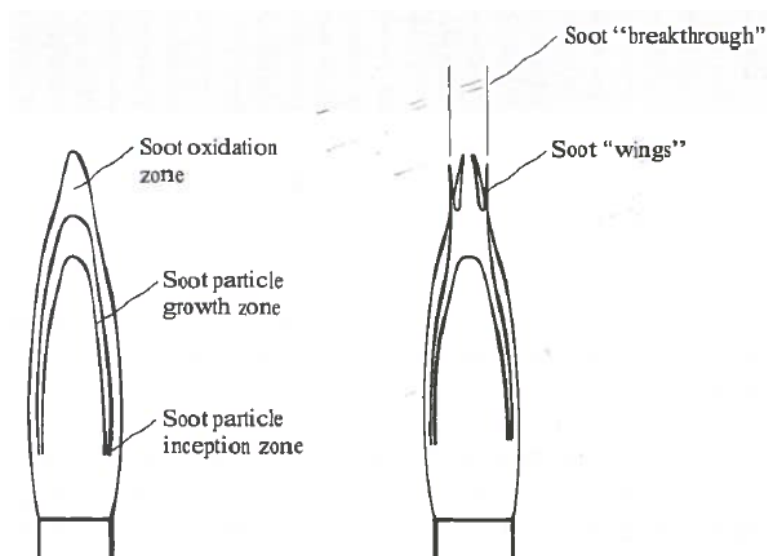
Figure 6: Soot Formation and Destruction Zones in Laminar Jet Flames (Turns 2012)

19

Depending on residence times and fuel type, not all the soot may become oxidized on its way out of the high-temperature oxidizing regions, creating soot wings. The excess soot that leaves the flame is generally referred to as smoke (Turns 2012).

In the scope of this scientific investigation, the main modes for emission control include very-lean combustion, and superior atomization quality. It is ideal to achieve lean premixed pre-vaporized combustion wherein the liquid spray completely vaporizes and mixes with the air prior to entering the combustion environment. This strategy is accompanied by reasonable risks as pre-vaporized fuel is subject to auto ignition due to short ignition delay times. However, lean direct injection is used in this study as a method to control emissions. The study of emissions production is used as a guide to indicate combustion quality and help identify trends linked to atomization and fuel properties/chemical makeup.

2.5. Biofuels and Fuel Flexibility

In the wake of future uncertainty of existing fuel supplies, gas turbine developers must incorporate their designs to run off a wide range of fuels, not only conventional fuels. The necessity for combustor designs that are fuel flexible and lead to environmentally friendly energy systems have driven combustion engineers to develop novel techniques for achieving ultra-low pollutant emissions (Khalil, Gupta 2013). Due to the differences from conventional fuels in properties such as density, viscosity, surface tension, and energy density, these fuels can present changes (both positive and negative) in the engine operability in regards to fuel consumption, efficiency, and emissions. Most notably, varying fuel properties have a direct effect on fuel

www.manaraa.com

atomization quality. It is well known that atomization performance is closely linked to combustion efficiency and emissions. However, when it comes to applications of liquid biofuels, gas turbines show good potential to cope with alternative fuels, while reciprocating engines face more challenges such as clogging and delayed ignition.

Still, there is a need for more attention devoted towards renewable liquid fuels. This area has received less consideration than turbines utilizing gaseous fuels due to not only their relative complexity between correlating atomization, fuel chemistry and properties, and emissions, but also the required investment in post combustion treatment systems primarily associated with ground based applications. For transportation purposes, the volumetric energy density of the fuel is an important parameter since it directly affects the size of the fuel storage system in the vehicle. A major challenge in implementing alternative fuels is the inherent reduction in energy density as compared with conventional diesels. In order to make more renewable fuels more economically feasible and operate at low emissions standards, a deeper understanding of the fuel preparation and aerothermochemistry is required. This understanding is key in identifying strategies to be implemented in future turbine designs and enable widespread use of renewable fuels while achieving superior emissions performance (Bolszo, McDonell et al., 2007).

2.6.   Fuels of Interest

By definition, biofuels are those generated from biological material. In more recent years, this concept has been narrowed down to renewable sources of carbon. The usage of biofuels is not a new concept. Use of ethanol for lamp oil and cooking has been reported for decades before it was tested by Samuel Morey in an internal combustion engine in the early 19th century. By the end of the 19th century, ethanol usage had expanded into farming machinery and

the automobile market. Before being replaced by distilled petroleum products, ethanol had become the replacement for whale oil. However, over the course of the 20th century, oil-derived products largely replaced biofuel usage. With climate change and sustainability of growing concern, renewable fuels of all types are emerging (Lee and Lavoie, 2013).

Biofuels are typically classified into two categories, primary and secondary, and three generations. While primary biofuels such as firewood are used in an unprocessed form for heating or cooking, secondary biofuels are processed in order to be used in vehicles or industrial machinery. First generation biofuels are directly related to biomass derived from edible sources. These fuels are typically made from sugars, grains, or seeds and requires relatively simple processing to provide a finished fuel. First-generation biofuels are being produced in significant commercial quantities around the world. Production of these fuels has been met with challenges due to required energy for production, and competition for arable land. This plays into the "food-vs-fuel" issue wherein the ever increasing fuel demand could potentially drive up food prices. For the United States, it is unlikely that conventional food-based feedstocks would be able to meet the fuel demand, and attempting to do so could lead to serious social implications (Balat and Balat 2010). To avoid this issue, second generation biofuels were developed. This generation of fuels are derived from non-edible sources of food production (e.g. rice husks or corn stalks) or whole plant biomass (e.g. grasses or trees). Biomass used for biofuel production is separated into three main categories: homogeneous (e.g. wood chips), quasi-homogeneous (e.g. agricultural and forest residues), and non-homogeneous (e.g. municipal solid waste). The price for these biomass sources are significantly less than for first-generation sources, making these fuels more desirable. However, non-edible biomass sources require more complex refining techniques (Lavoie et al., 2011). Lastly, third generation biofuels are derived from algae

sources, which has a very distinctive growth yield as compared with classical biofuels. A summary of biofuels and their classifications is presented in Figure 7 below.
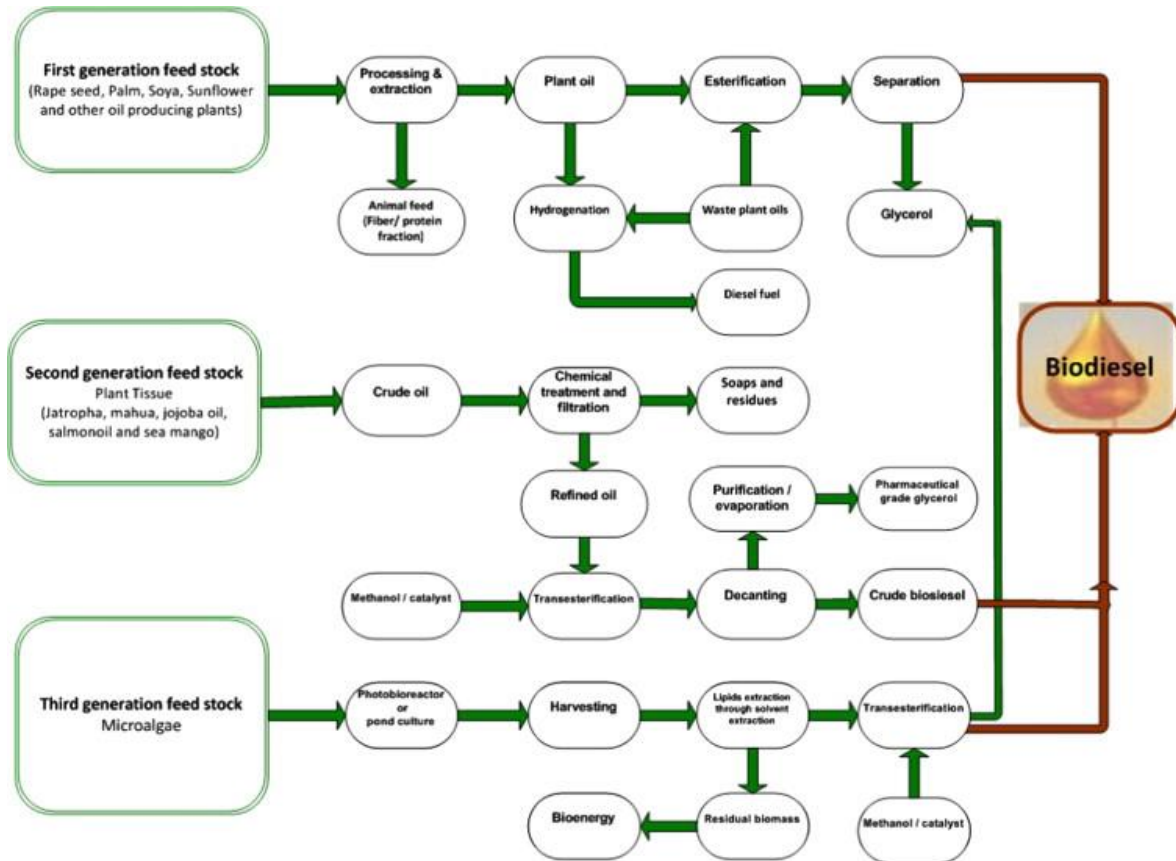
Figure 7: Processes of Biodiesel Production from Various Feedstocks (Rashid et al., 2014)

2.6.1. Algae Derived Fuels

Associated land issues for first and second generation biofuels has led to the development of biofuels derived from algae. Algae derived biodiesel has emerged as one of the most promising biodiesels for a few main reasons. (1) It is produced with high photosynthetic efficiency and growth rates as compared to those derived from conventional land based crops. In comparison to conventional crops used in biodiesel production, algae yields 30 times more oil

per acre (Kumar & Varun et al., 2013). (2) The production process is one that does not compete with food sources and does not require as large area of land. Algae cultivation is highly tolerable to growing conditions and can be grown almost anywhere, including sewage or salt water (Ahmad et al., 2011). Other advantages include their relative simplicity as compared with other biofuels, fast reproduction capabilities, and large scale production of useful oils.

The overall production of algae consists of the cultivation of algae, followed by the extraction of oils produced, then refinement of the oils into biofuel. The general process utilized in microalgae consists of converting solar energy, water, and CO_2 into lipids or triglycerides. Microalgae are able to obtain CO_2 from various sources. The most straightforward CO_2 allocation method comes from the atmosphere which relies on the mass transfer of air to the microalgae in their aquatic environments. However, due to the overall relatively low concentration of atmospheric CO_2 (0.036%), the use of these types of algae are not economically feasible. Other alternative methods include capture from flue gas, which contains up to 15% CO_2, providing a rich source for microalgal cultivation and potentially a more efficient path for cell growth (Brennan & Owende et al., 2010).   Although there are thousands of different strains of microalgae, there exist three main categories that describe the processes used to produce oils. Photoautotrophic algae grows in the conventional manner by undergoing photosynthesis to convert sunlight and CO_2 into energy for the plant. Often, photoautotrophic algae produce more sugars and proteins than useful oils. Heterotrophic algae do not use photosynthesis to grow, but do so by consuming externally supplied organic substances. These algae utilize carbonates such as Na_2CO_3 and $NaHCO_3$ for cell growth. Some of these species have high extracellular carbohydrate activities which converts carbonate to free CO_2 to facilitate CO_2 assimilation. Several species have also been found to directly utilize bicarbonate by an active transport system

24

(Wang & Wu et al., 2008). Mixotrophic algae use elements from both photoautotrophic and heterotrophic algae in their growth process. For some strains, higher volumes of lipids and triglycerides can be produced by depriving the algae of nitrogen (Nigam and Singh 2011).

Cultivation of microalgae has been done since the 1950's using open-air systems. These classical systems come in the form of lakes, natural ponds, circular ponds, raceway ponds, and inclined systems (Figure 8). Open air systems are the most widespread types for a few reasons: they are easy and inexpensive to build, durable, lead to larger scales of production than closed systems, and utilize free water runoff from nearby lands of channeled sewage/water from treatment plants. These systems present significant technical challenges. Open systems are susceptible to weather conditions do not allow for temperature, evaporation, and lighting controls; making them dependable on the regional climate conditions. Furthermore, contamination of these systems by predators and other fast growing heterotrophs has restricted the commercial production of algae to certain fast growing or naturally occurring species.
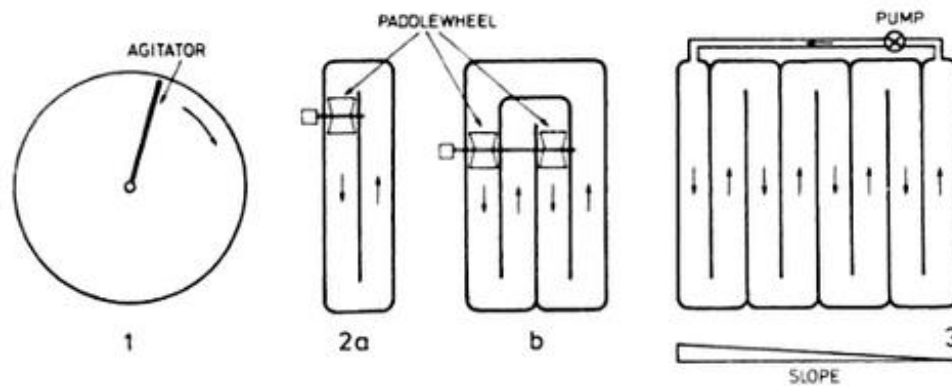
Figure 8: Schematic outline of major algal pond designs. 1) Circular pond with rotating agitator, 2a) Single oblong raceway with paddle wheel, 2b) Joined oblong ponds with paddle wheels, 3) Sloped meandering pond with circulating pump (Becker 1994)

Closed-system photobioreactors are characterized by the regulation of nearly all the biotechnologically important growth parameters, as well as reduced contamination risk, no CO_2 losses, reproducible cultivation conditions, and flexible technical design. Algae in these systems receive sunlight through transparent container walls or via light transmitting fibers connected to sunlight collectors. Figure 9 shows a schematic of a photobioreactor system.
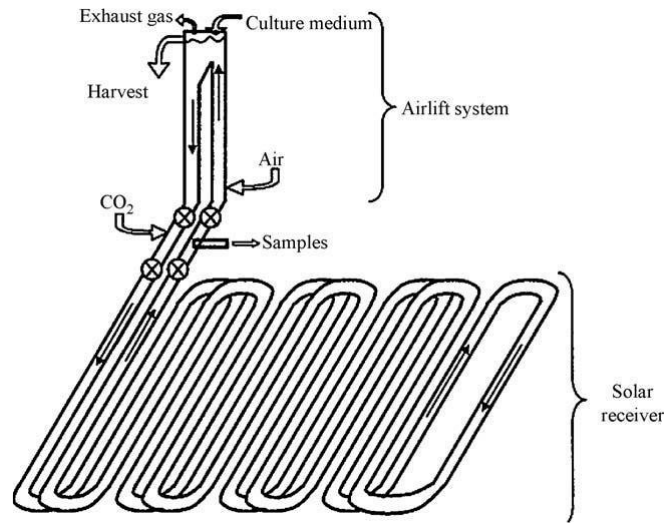
Figure 9: Schematic of Photobioreactor System (Brennan and Owende 2010)

Over their lifetime, algae produce lipids that can be extracted for conversion to fuel. The most common methods are expeller/oil press, liquid-liquid extraction (solvent extraction), supercritical fluid extraction, and ultrasonic techniques. These extraction techniques can be energy intensive and expensive, reducing some of the benefits. After the extraction process is complete, the resulting oil can be converted into biodiesel through a process called transesterification. In this reaction, triglycerides are transformed into fatty acid alkyl esters in the presence of an alcohol (methanol or ethanol) and a catalyst (such as alkali acid) to produce glycerol. Biodiesel produced from microalgae, termed hydrotreated renewable diesel (HRD),

has similar physical and chemical properties to petroleum diesel (Dragone & Antonio et al., 2010).

Blakey et al. reviewed a wide range of alternative fuels used in aviation based gas turbines, as well as demonstrated some combustion characteristics in their own study. They found a general decrease in NO_x emissions of 12% when using hydrotreated renewable jet-fuel (HRJ). CO emissions varied for different alternative fuels and ranged from a 20% reduction to an 8% increase. It was shown that CO emissions is significantly dependent on fuel aromatic content. Increasing aromatics and molecular weight of the fuel reduces the combustion efficiency, hence an increase in CO. In the same way, UHC emissions varied similarly, ($\pm$44%) to CO emissions due to aromatic content. CO_2 reductions of nearly 4% were typically found using alternative fuels due to higher calorific values, resulting in lower fuel consumption. A study conducted with an aviation Allison/Rolls Royce T56-A-15 gas turbine, and algae derived HRJ had shown to reduce UHC emissions as compared with Jet A-1, again attributed to the reduction in aromatic content. Researchers also found the algae HRJ to reduce NO_x emissions by 96%, CO by 26%, and CO_2 by 13%. With algae synthetic fuels being relatively new, there is not a large amount of published literature on its usage in gas turbines. Listed studies show slightly better emissions than for conventional fuels, which is expected as researchers detail their similarities in physical properties.

2.6.2. Methanol

A renewable fuel not specifically classified into any of the three generations of biofuels is Methanol, CH_3OH, a simple alcohol. Methanol is one of the most produced commodity

chemicals and is made via four primary renewable pathways. The first three pathways rely on gasification of the feedstock to syngas followed by catalytic conversion to methanol. These three sources include: municipal waste such as trash and construction materials, industrial waste such as pulp and paper waste, and lastly form biomass feedstocks such as agricultural residues, forest trimmings, and crop residuals. Syngas is typically composed of 30 to 60% CO, 25 to 30% H_2, 0 to 5% methane, and 5 to 15% CO_2. The catalytic conversion utilizes components in the syngas to form methanol:

$$CO + 2H_2 \Leftrightarrow CH_3OH$$
$$CO_2 + 3H_2 \Leftrightarrow CH_3OH + H_2O$$
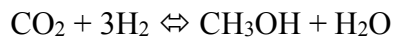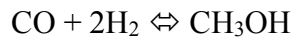
The fourth pathway consists of CO_2 flue gas capture wherein methanol is produced with the addition of hydrogen and a catalyst. It is ideal to produce the hydrogen via water electrolysis using electricity generated from renewable resources (Law et. al 2013). Methanol had been heavily investigated as a transportation fuel in the 1970's during the gas crisis, but had then received less attention once oil sources became more abundant, hence much research on methanol use in gas turbines was conducted in the 70's and 80's.

A report on methanol viability in gas turbines cites a number of field tests. In 1974, Turbo Power and marine ran a 20 MW gas turbine on liquid methanol and recorded a 74% reduction in NO_x with comparable CO levels to diesel #2. GE conducted methanol testing in a MS6001B combustor and observed an 80% reduction in NO_x emissions. The report notes that the gas turbine systems required modifications to accommodate higher mass and volumetric flow rates. Methanol's low flash point necessitated a secondary fuel be used during start up to avoid engine damage as well as modifications to existing seals in the fuel system due to deterioration caused by methanol (GE 2001). More recent work on methanol use in gas turbine systems has been explored

by Hain et al., in a FT4C Twin PAC 50 MW GT turbine. They report being able to run the system at 70% load due to pump capability limitation; methanol has roughly half the heating value of conventional diesel, requiring higher flow rates. At full methanol load, researchers reported 75% NO_x reductions, SO_2 elimination, roughly 80% more CO, and 90% reductions in PM (Hain et al., 2012). Overall NO_x reductions found using methanol have been attributed to the lack of fuel bound nitrogen, and decreased physical properties which leads to better atomization quality.

2.6.3. Ethanol

Ethanol, also known as ethyl alcohol C_2H_6O, is currently the most widely used biofuel. Over the past 30 years, a robust ethanol industry has developed in the United States, leading to new methods for large scale ethanol production. One of the oldest biotechnological processes employed by humans is the generation of ethanol from starch and sugars. This mode of ethanol production depends on saccharomyces to efficiently and rapidly ferment the glucose, fructose, and sucrose in sugars of the maltose and glucose in starches into ethanol at high concentrations. In the fermentation of wet sucrose, the invertase enzyme in yeast catalyzes the hydrolysis process to form glucose and fructose as shown below:

$$C_{12}H_{22}O_{11} + H_2O \rightarrow C_6H_{12}O_6 + C_6H_{12}O_6$$
Sucrose   Water   Glucose   Fructose
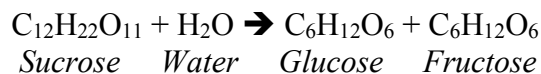
A second enzyme, zymase, in the yeast converts the glucose and fructose into ethanol and carbon dioxide.

$$C_6H_{12}O_6 \rightarrow 2C_2H_6O + CO_2$$

First-generation ethanol production utilizing sucrose and starch based biomass represent nearly 90% of global biofuel production, with the majority of production feedstocks supplied by corn. Synthetic ethanol manufacturing is becoming more developed in a means to ease the pressure on farmers to devote crop space to food production. Cellulosic biomass materials such as grasses, trees, and agricultural residues are treated using hydrolysis processes to extract sugars, followed by fermentation into ethanol (Haggstrom & Rova et al, 2014). Although producing cellulosic ethanol is currently more costly than that made from starch crops, the U.S. government has launched a Biofuels Initiative with the objective of quickly reducing the cost. In 2009, more than 7.3 billion gasoline-equivalent gallons were added to gasoline in the United States in order to meet implemented biofuel usage requirements in an effort to reduce air pollution. In many parts of the U.S., ethanol is blended with gasoline to form E10, a 10% ethanol and 90% gasoline blend, however higher ethanol concentration blends exist such as E85, or even neat ethanol E100. Currently, all automobile manufacturers doing business in the U.S. must design to allow use of E10 in their engines, but only certain flex fuel vehicles can operate on E85. In general, ethanol addition aids combustion by reducing CO, UHC, and NO_x in automobile engines (U.S. DOE 2014). The use of ethanol has been investigated in gas turbine engines due to certain advantages over conventional fuels. These include fuel bound oxygen, lower viscosity and surface tension, higher cetane number, and lower flame temperatures.

In a study conducted by Alfara-Ayala et al., a gas turbine was operated on two conventional fuels (natural gas and diesel) and one bioethanol fuel. They showed that in matching the mass flow of each fuel that the power output of the turbine was not matched with ethanol, due to its lower heating value. However, after matching power output for all fuels, CO_2 emissions for bioethanol, matching that of diesel, were 19.5% higher than natural gas.

30

Bioethanol led to reduced NO_x levels by 65% and 92% as compared with natural gas and diesel, respectively (Alfaro-Ayala et al., 2013).   In Brazil, the 87 MW Juiz de Fora power plant initially designed for natural gas is being run on pure ethanol derived from sugar cane. This power plant utilizes two GE LM6000 PC gas turbines in a simple cycle configuration. Relative to natural gas, they have reported CO_2 reductions of 6%, elimination of SO_2, and NO_x reductions by 3.3% (GE 2010). Ethanol was also examined in a 6B Frame GE GT in Gao, India as a naptha substitute. They reported higher mass flow rates for ethanol to match power output, but report 50% lower NO_2 levels, higher CO_2, and other operability issues such as higher nozzle pressure requirements, and handling problems due to low vapor pressure (Kallenberg 2013). Lupandin et al., successfully operated a GT2500 turbine on ethanol and found similar results, decreased NO_x followed by increased CO emissions. Although they were able to run their system at full load, it required 68% greater volumetric flow rate than diesel #2.

2.6.4. Biodiesel

The last renewable fuel of interest in this study is biodiesel which is defined as monoalkyl esters of fatty acids from vegetable oils and animal fats (ASTM D6751). Several different feed stocks can be used to produce biodiesels. These sources can come from edible and non-edible feedstocks, making biodiesels both first and second generation biofuels. Some common sources include rapeseed, sunflower, palm, and soybean oil, depending on the region. Non-edible oils used can be jatropha oil, waste cooking oil, and animal fats. These oils are all composed of a variety of fatty acids from which the variation of biodiesel properties arises (Balat & Balat 2010). It is common to find that biodiesels are comprised of a mixture of biodiesels derived from different feedstocks.

Biodiesel is most commonly produced from feedstocks by a process termed transesterification. This is a reaction (Figure 10) in which a vegetable oil or animal fat is catalyzed with a simple alcohol such as methanol to produce a mixture of fatty esters and glycerin.
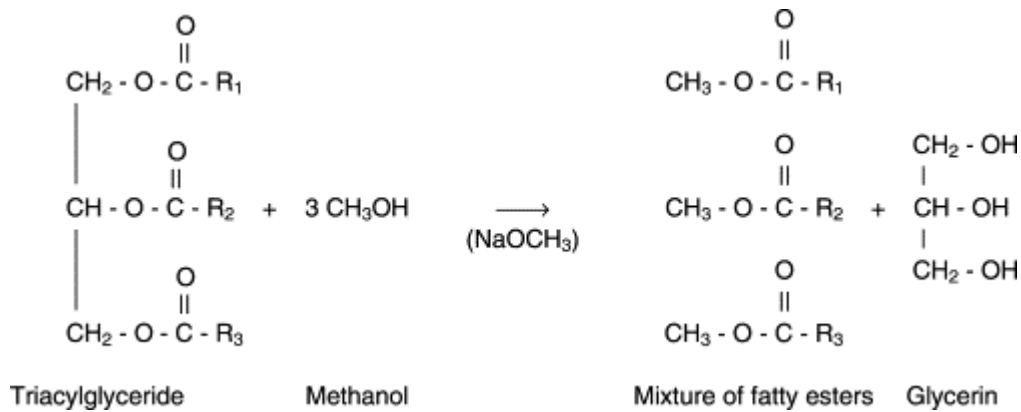
Figure 10: Transesterification of a Triacylglyceride (Van Gerpen et al., 2014)

As the transesterification reaction is an equilibrium process it requires an excess of methanol, leaving residual methanol that is removed by flash evaporation. The remaining glycerin is removed by either settling in a decanter, centrifugation, or possibly a coalescer. The final product is then subject to further filtration and additives such as antioxidants and pour point depressants before the fuel is sold (Van Gerpen et al., 2014). The major components of biodiesels are straight chain fatty acids and common fatty acids; the influence of fatty acid composition structure on biodiesel properties has been demonstrated in previous studies. Research has found that biodiesels with a high level of methyl oleate (monounsaturated fatty acid) may have excellent characteristics in ignition quality, fuel stability, and flow properties at low temperature (Pinzi & Garcia et al., 2009). Rapid ignition characteristics of biodiesels is attribute to higher cetane numbers due to longer chain lengths and more saturation. Drawbacks to biodiesel are higher viscosity and surface tension, lower energy content (roughly 11% less

www.manaraa.com

energy than Diesel #2), and higher cloud and pour point, which can lead to engine compatibility issues. There is a larger body of information on biodiesel usage in gas turbine systems than available for methanol and ethanol.

Biodiesel use in a 30 kW Capstone C30, as well as in atomization tests has been examined by Bolszo & McDonell. Spray diagnostics showed consistently larger SMD values for biodiesel than conventional diesel due to the increased viscosity. This, along with the lower fuel volatility required 56% more evaporation time for the biodiesel. After coupling atomization results with emissions, B99 emissions were found to vary with the air to liquid ratio (ALR), a ratio between the nozzle atomizing air and fuel mass flow rate. Optimized operation settings resulted in no change in CO levels at full power, but produced 39% more NO_x than the conventional diesel (Bolszo & McDonell 2009). Chiaramonte et al. experimented with biodiesels and pure vegetable oil (VO) in a Garrett GTP 30-67 micro gas turbine. They found that CO emissions from biodiesel and vegetable oil were 28% and 118% larger than for diesel #2 and reported no change in NO_x for all fuels. It was noted that even with fuel pre-heating, the microturbine could not run at idle state when run on pure VO (Chiaramonte et al., 2013). A waste cooking oil derived methyl ester biodiesel (WME) was tested on a low NO_x gas turbine combustor at atmospheric pressure and 600K pre-heat. Li et al. found that WME biodiesel produced more NO_x and less CO and UHCs than kerosene. The biodiesel had lower flame extinction limits which was attributed to the oxygen content in the fuel. Other tests performed on real systems have required modifications to allow for use of alternative fuels. Lupandin et al. modified a GT2500 turbine to run liquid alternative fuels in order to (1) provide sufficient atomization for the relatively viscous fuels, (2) avoid fuel nozzle clogging due to PM in the fuel, (3) ensure that the acidic nature of some fuels would not corrode hardware, and (3) redirect

compressor air for use in the atomizing nozzle. They found that biodiesel produced equivalent NO_x emissions as compared to DF2, but led to increased CO emissions (1 to 4.1 ppm). Overall, the group showed that they were able to run their system on a variety of biodiesels and ethanol at full power while meeting local emissions limits.

2.7.   Fuel Blending Strategies

Biodiesels consistently display problems during atomization by producing relatively larger drop sizes than conventional fuel; along with low fuel volatility, this leads to longer evaporation times. The energy density of biodiesel is much greater than for ethanol and methanol, which could lead to less reduction in vehicle range. Still, limited emissions studies report somewhat inconsistent finding for biodiesels, with the only trend appearing to be increases in NO_x. Review of background literature (Table 1) for renewable fuel usage in gas turbines leads to some conclusions for the pure alcohols. The advantages are:

- Lower life cycle carbon production

- Lower carbon content and freeze point

- Higher flash point, octane rating, and latent heat of vaporization

- Reduced PM and NO_x

The main disadvantages for methanol and ethanol are:

- Methanol is highly toxic

- Highly corrosive, with poor lubricity in pumps and injectors

- Methanol's lower cetane rating enables spark knock

- Generates aldehyde emissions

- Lower specific energy and energy density (Lefebvre & Ballal 2010)

In transportation based gas turbines, methanol and ethanol usage would result in approximately a 53% and 37% reduction in vehicle range, respectively. These points, summarized in Table 1, suggest that there are pros and cons to each renewable fuel, and that none have really been a proved technology as a drop in fuel to an existing system without requiring system modifications.

Table 1: Past Emissions Studies

			Change in Emissions (relative to base fuel)		
Source	Test Platform	Fuel	NO_x	CO	CO_2
Blakey et al., 2010	Unspecified Engine	Jet A-1 HRJ	-12%		
	P&W 4 Burner	Jet A-1 HRJ		-20%	
	CFM65-7B	Jet A-1 HRJ		+8%	
Pucher, Allan et al., 2011	T56-A-15 Combustor	Jet A-1 HRJ (Algae)	-96%	-26%	-13%
Alfaro-Ayala et al., 2013	Not specified	Natural Gas Ethanol	-65%		+19.5%
GE Energy 2010	GE LM6000 PC	Natural Gas Ethanol	-3.3%		-6%
Kallenberg 2013	6B Frame GE GT	Naptha Ethanol	-50%		
Hain et al., 2012	FT4C Twin PAC 50 MW GT	Oil #2 Methanol	-75%	+80%	
GE 2001	Unspecified 20 MW Turbine MS6001B	Diesel #2 Methanol	-74%	0%	
		Diesel #2 Methanol	-80%		
Bolszo & McDonell 2009	Capstone C30	Diesel #2 B99	+39%	0%	
Chiaramonte et al., 2013	Garrett GTP 30-67	Diesel #2 B100 VO	0% 0%	+28% +115%	

35

Li et al., 2010	Unspecified Low NO$_x$ Combustor	Kerosene B100 (WME)	+27%	-30%	
Lupandin et al., 2005	GT 2500	DF2 Biodiesel Ethanol	0% -69%	410% 1.4×10^3%	

In an effort to incorporate renewable fuels into gas turbine operations as well as lower emissions, biodiesel has been blended with conventional diesels in various proportions. Nascimiento et al. experimented with diesel/biodiesel in blends of 5%, 20%, 30%, 50%, 75%, and 100% biodiesel respectively in a 30 kW micro-turbine engine. They report an 18% increase in volumetric flow to match the power output between diesel and B100, thus all blends required less volumetric flow than the B100. At various loads, they found higher CO emissions for B100 than diesel; these emissions were cut for all blending ratios. Inversely, B100 produced less NO$_x$ pollutant than diesel, thus the addition of B100 to diesel successfully decreased NO$_x$ levels (Nascimiento et al., 2008). Rehman et al. found different conclusions when experimenting with diesel-jatropha oil blends in a IS/60 Rovers gas turbine at various loads. They initially determined that while jatropha oil shares similar characteristics to diesel oil, its viscosity is much higher and can be lowered with blending with diesel; specifically blends of 15% and 25% biodiesel. Emissions results showed a decrease in CO and UHC emissions and increased NO$_x$ emissions for higher concentrations of biodiesel (Rehman et al. 2011). Inconsistencies in emissions results from various sources can be attributed to a variety of factors such as: various biodiesels and chemical compositions, systems with and without fuel pre-heating, nozzle configuration, and turbine sizes. Regardless, there is consistent evidence that blending of oxygenated fuels enables more control between CO, UHC, and NO$_x$ emissions.

With the associated faults of pure ethanol well known, ethanol has been recognized as a viable additive to petroleum fuels in small quantities for spark ignition and compression ignition engines (Agarwal, 2007, Lapuerta et al., 2008a, Canakci et al., 2008 and Huang et al., 2004). Addition of up to 10% ethanol in diesel fuel can reduce NO_x and PM emissions with a negligible drop in energy density. Alcohol-diesel blends have disadvantages such as reduction in lubricity, cetane number, and ignitability. In order to solve these problems, additives such as cetane-enhancers have to be applied. (Ren et al., 2008). Ethanol-biodiesel blends in internal combustion engines have been investigated in limited studies. Park et al. investigated blends of biodiesel with 10%, and 20% volumetric ethanol addition under various injection conditions for a single-hole injector intended for use in a CI diesel engine. Droplet size measurements across the spray plume illustrate consistent decreases in SMD with increased ethanol blending ratios (Park et al., 2009).

2.8.   Prior Work and Current Motivation

Bolszo and McDonell too speculated that atomization behavior of biodiesel can be improved with the addition of ethanol; miscibility between the two can create a fuel blend with viscosity and surface tension values closer to DF2. Viscosity and surface tension testing was performed on B99-ethanol blends with 5%, 10%, 20%, and 40% ethanol. The results shown in Figure 11 display a steep decay in viscosity and surface tension with increasing ethanol concentration.
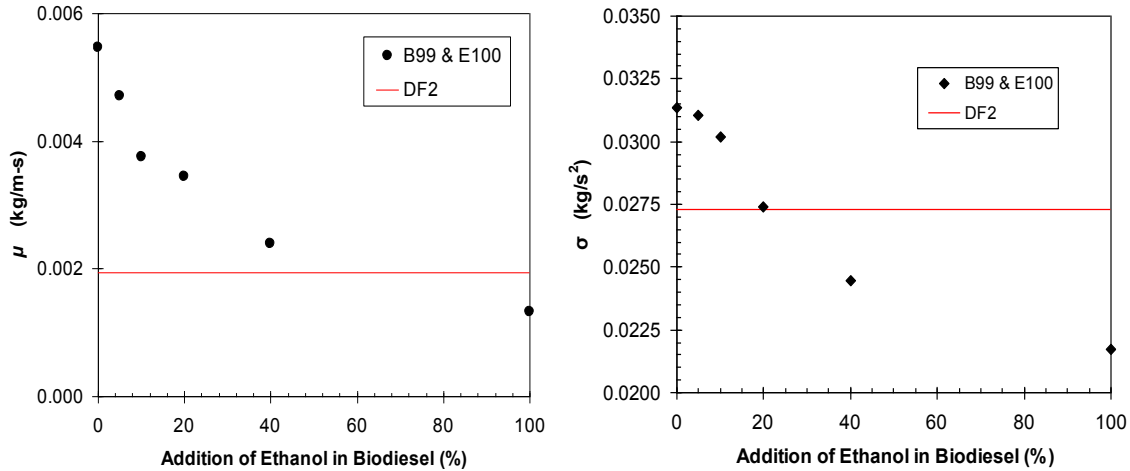
Figure 11: Viscosity [L] and Surface Tension [R] for 95/05, 90/10, 80/20, and 60/40 Percent Blends of B99 and Ethanol (Bolszo & McDonell 2008)

The fuel blends were tested in a Capstone C30 micro-turbine across a range of operation loads. Their results show that, with the addition of ethanol, the NO emissions decrease (-25% at high loads) while the change in CO remained constant within experimental uncertainty.
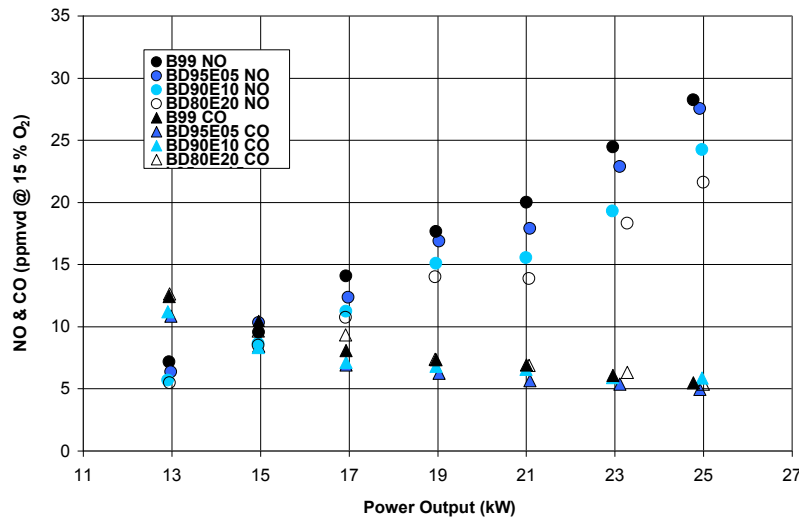
Figure 12: Emissions Reduction of NO for B99 with Addition of Ethanol in Percentages of 5, 10, and 20 (Bolszo & McDonell 2008)

Researchers speculated that the decrease in NO emissions was caused by improved atomization quality through the air-blast atomizer due to the drop in fuel viscosity. However, atomization data were not gathered for the B99-ethanol blends and thus remains unconfirmed for the air-blast atomizer, as well as for various other nozzle types.

In summary, the majority of effort investigating renewable fuel combustion and atomization has mainly focused on CI and SI engines for diesel and Otto cycles for transportation applications. It is of interest to identify fuels that can be used in existing transportation based gas turbines that do not require major system modifications. Currently, only a handful of studies on renewable fuels have been aimed towards gas turbine applications where each fuel has unique limitations that inhibit most from acting as functional replacements for petroleum fuels. Further, the potential for combining individual types of renewable fuels as means of optimizing overall performance by balancing drawbacks and advantages of each has yet to be systematically studied. Thus, the present research effort aims to characterize the combustion performance of various biofuel *blends* in order to identify a more ideal fuel derived solely from renewable resources. Further, to help elucidate the observations regarding combustion performance, detailed atomization performance studies are also carried out.

3. Approach

Task 1: Select renewable fuels of interest according to background information regarding the status and prominence of each.

Numerous factors have prompted increasing levels of research focusing on renewable fuels. As such, an extensive literature review is critical to understanding the current state of the field including recent developments, ongoing work, state of the art fuels being developed, and unresolved challenges. New knowledge is used in proposing solutions to existing questions that is to be studied in the current thesis. Investigating concurrent research will also provide insight on successful experimental techniques, methods for data collection, and analytical methods.

Task 2: Determine the fluid properties of the fuels under investigation.

Understanding the chemical makeup of each fuel is crucial in setting up conditions for testing, as well as predicting performance outcomes. Data previously collected from UCI's Mass Spectroscopy Gas Chromatography (MSGC) facility is used to identify the molecular composition of B99, DF2, F-76 distillate, and the F-76/Algae HRD blend. These findings are used in compiling an averaged chemical formulation for each fuel and, using trusted sources, unmeasured properties such as the lower heating value can be reasonably calculated. The physical properties of each fuel largely govern the atomization quality, directly impacting combustion performance. Comprehensive understanding of each fuel is gained by measuring the viscosity, surface tension, and density via falling ball viscometer, stalagmometer, and volumetric weighing. The additional fuels tested are as follows: B99, ethanol, and methanol. Details on the measured physical properties for each fuel are discussed in section 5.1.

<u>Task 3: Create test bed with diagnostic tools for data collection.</u>

This test facility must use equipment fit for precise low flow rates in order to provide consistency between tests. Experiments require mounting of air-blast atomize on a movable traverse which will allow for various measurements of both atomization and combustion data. Such measurement tools will capture high speed imaging, non-intrusive point velocity and droplet size measurements, still photography, and emissions sampling.

<u>Task 4: Conduct non-reacting experiments for variety of test conditions.</u>

Establish desired testing conditions for each fuel to simulate a "drop in" scenario for a gas turbine system, then match flow rates accordingly between fuels. In order to fully characterize the atomization behavior of each fuel, a plain-jet air-blast atomizer is used. High speed shadowgraphy and PDPA measurements will provide droplet sizing, velocity, and spray plume distributions. Combustion tests will be additionally be performed where emissions consoles will record pollutant concentrations from exhaust plume, while color photos are taken that will be used in image averaging analysis.

<u>Task 5: Contrast data with empirical models to gain insight on observed phenomena.</u>

PDPA and LDV data points across each traverse are plotted for each run so that details within the spray plume are observable and easily contrasted between fuels and the various test conditions. Size data are computationally consolidated in order to become easily compared with theoretical predictions derived from various sources. The results are compared to the measured

physical properties in order to draw conclusions of their impact on atomization performance. This helps describe the limitations and inherit assumptions set forth in employing theories for calculating droplet sizes.

<u>Task 6: Optimize biofuel performance by determining ideal fuel blending ratios.</u>

Upon completing testing for the six baseline fuels laid out in Task 4, the optimum air-blast atomization technique is chosen to be used on additional fuel mixtures. Four B99-ethanol fuel blends are created for a range of mixing ratios. The physical properties of the blends are measured and compared with fuel preparation standards set forth for the DF2 and F-76 distillate fuels. The blended fuels are tested in cold-flow conditions in order to determine differences in spray behavior. Combustion analysis of B99-ethanol blends are performed in order to contrast with results of pure fuels.

The objectives of task 1 are largely fulfilled in Chapter 2, the results of the remaining objective are presented in the following chapters. The results of Task 2 are presented in Chapter 5, Section 1. Equipment and setup elements of Task 3 are presented in Chapter 4. Finally, the outcomes of Tasks 4-6 are presented in Chapter 5.

4. Experiment

4.1.   Fuels of Interest

4.1.1. Base Fuels

This study investigated a total of 6 base fuels: five pure fuels and one diesel-HRD (see Figure 13). Serving as the control fuel for the study, an F-76 military distillate was provided by the office of Naval Research (ONR). ONR also provided the study with a 50-50 blend of Algae-derived HRD and F-76 distillate (F-76/Algae). In addition, ultra-low sulfur diesel #2 (DF2) was obtained from a local gas station. The three pure renewable fuels are methanol and industrial grade ethanol (obtained from the UCI Chemical Store) and B99, a 99% biodiesel 1% DF2 blend which was purchased from Downs Energy in Corona, Ca.
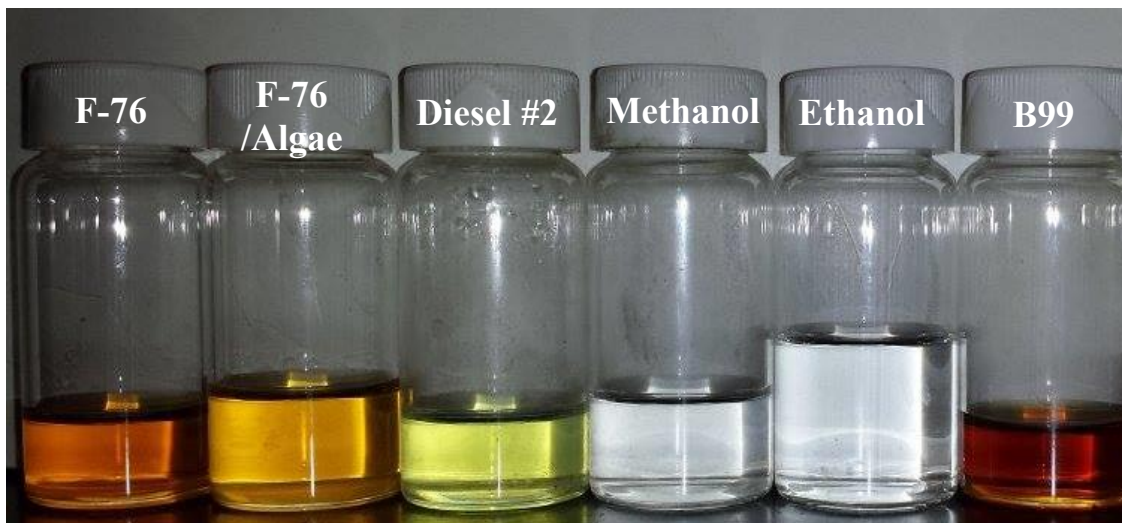
Figure 13: Fuels Studied for Baseline Tests

4.1.2. B99-Ethanol Blending

In addition to the 6 base fuels mentioned in section 4.1, four B99-ethanol blends were mixed in house on the following mass fractions: 80/20, 60/40, 40/60, and 20/80 B99/ethanol

respectively. Nomenclature of the blends are termed BE%B99; for example, BE80 represents a B99-ethanol mixture comprising 80% B99 by mass. Each fuel was weighed into a beaker and mixed via a magnetic stir plate for 5 minutes. Bolszo conducted simple laboratory experiment to determine whether B99 and ethanol are miscible with agitation. Blends of 90/10, 80/20, and 60/40 were fully mixed in closed containers and monitored for 48 hours as the blends' temperatures were decreased to 3° C for over four hours and raised back to room temperature with no component separation (Bolszo 2008). Similarly for this study, all four B99-ethanol blends were mixed and sealed in closed containers and let sit at room temperature for one week, where after no separation was observed.

4.1.3. Physical Properties

Four physical properties were measured at ambient conditions for each fuel: density, surface tension, viscosity, and refractive index. Density was calculated using a mass balance to weigh a measured volume of liquid indicated by a graduated cylinder. Surface tension was found using a stalagmometer. This device is essentially a pipette with a broad flattened tip which permits large droplets of reproducible size to slowly form and finally drop. The stalagmometer determines surface tension based on the number of drops that fall and the density of the liquid, all standardized to water as the reference liquid. Viscosity was found using a falling ball viscometer. This device is a high precision bore glass tube with two horizontal red lines fused into the glass. The tube is filled with a liquid of interest, and a ball (glass, steel, or tantalum) is inserted. The viscometer allows for viscosity calculations given the density of the fluid, density of the chosen ball, and time of descent between the two red markers. For each

44

fluid, three trials were performed using two different balls to provide experimental redundancy. The refractive index of each fluid was additionally measured using a refractometer. Information on fuel composition was obtained from researchers Bolszo and Legg using Mass Spectroscopy Gas Chromatography (MSGC).

4.2. Combustion Hardware

4.2.1. Low Velocity Burner

Under partnership with the UCI Chemical Engineering and Materials Sciences Department and the Office of Naval Research (ONR), a stainless steel low velocity burner (LVB) was developed by Legg & Narvaez et al. in order to simulate the effluent from a conventional gas turbine combustor for use of advanced materials testing for turbine blades and coatings. Materials testing required continual operation of the burner for tests lasting from 500 to 1000 hours while using less than a (55-gallon) drum of candidate fuel. To accomplish this, the burner was scaled to produce a combustion zone requiring a nominal flow rate of 4 ml/min. A picture of the burner is depicted in Figure 14, and a cross section drawing is shown in Figure 15.
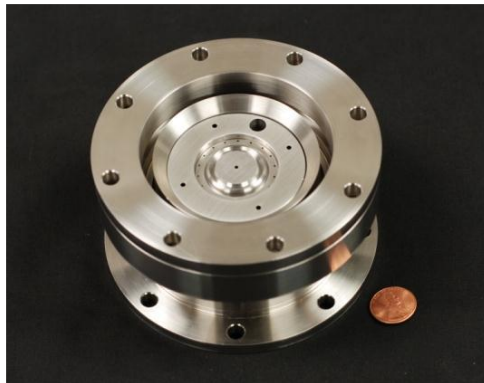
Figure 14: Low Velocity Burner (Legg 2012)
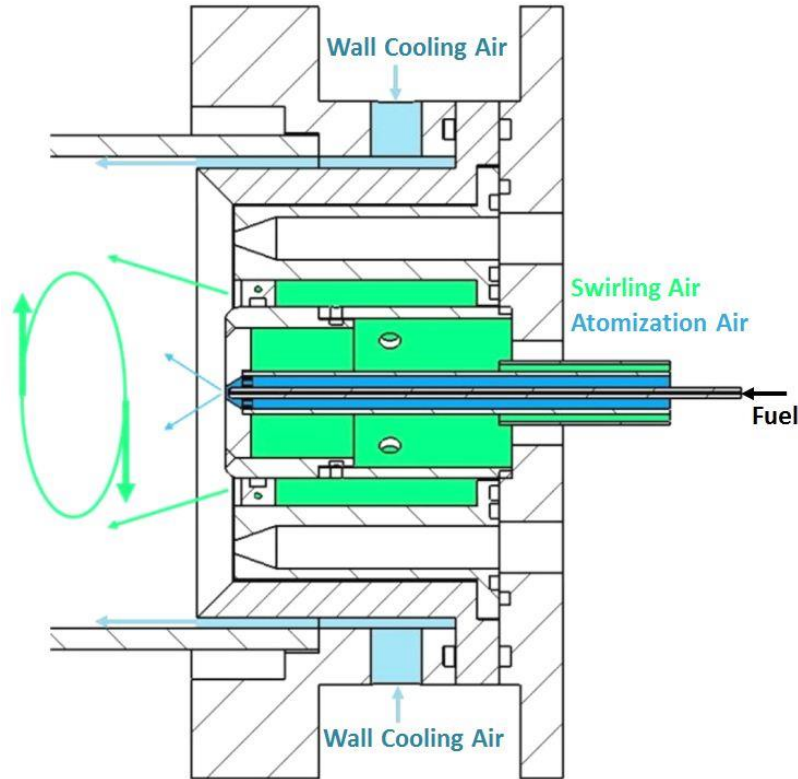
Figure 15: Cross-Section of Burner with Colored Air Circuits

Several features typically found in real gas turbine combustors were incorporated into this burner design. This air-blast combustor utilizes three distinct air circuits. One air circuit, the wall cooling air (light blue), forms an annulus of air around the perimeter of the burner. This serves to keep wall temperatures low, as well as dilute the reaction to lower the equivalence ratio. Surrounding the center injector is the swirling air circuit (turquoise) which flows into the combustion chamber via 12 0.792 mm diameter holes drilled at 55º from vertical. This introduces additional air into the reaction zone for combustion. The angled vanes introduce the air in a swirling cone which stabilizes the reaction, improves fuel and air mixing, and serves to provide recirculation zones for the flame to anchor on. The fuel atomizing air-line (blue) runs through the center of the combustor. In this design, the fuel tube runs concentrically through the

www.manaraa.com

air line by a centering ring near the nozzle exit. A close up cross-section view of the nozzle exit is depicted Figure 16 with the relevant dimensions listed in Table 2.

Table 2: Air-Blast Atomizer Parameters

Parameter	Value
Liquid Orifice Diameter	0.3048 mm
Air Orifice Diameter	3.175 mm
Atomizing Air Cone Angle	57.79 degrees
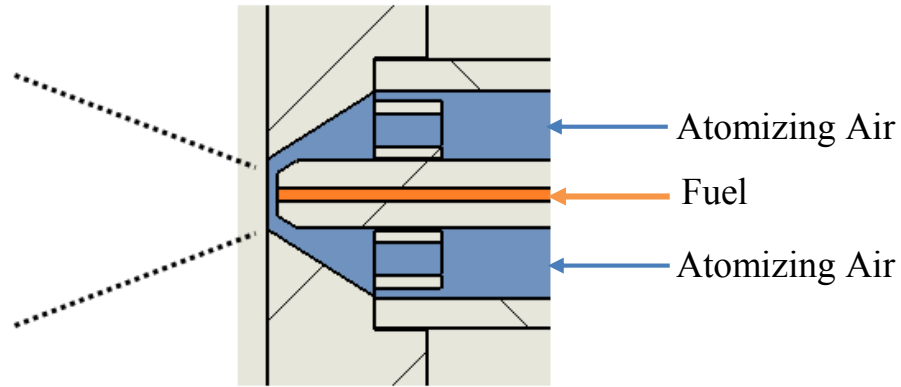
Figure 16: Cross-Section Close Up of Air-blast Nozzle

This configuration allows for repositioning of the fuel tube from the exit orifice. In moving the fuel tube, the effective area of the fuel atomizing air (FAA) through the nozzle changes. This feature allows researchers to control the velocity of the impinging air on the fuel stream. It must be noted that the work presented in this thesis uses a modified version of the same low velocity burner used by Legg. The major modification made is in the streamlining of the fuel tube near the nozzle exit wherein the chamfer feature runs parallel to the nozzle wall. This geometrical difference has been found to improve the atomization quality for this air-blast atomizer, with more details found in section 5.3.1.

4.2.2. Combustor and Controls

Combustion tests involved use of the LVB with a cylindrical quartz tube to contain the reaction while providing optical access for a Nikon J-1 Camera. Emissions data and temperature readings were sampled from the tail end of the exit pipe as depicted in Figure 17.
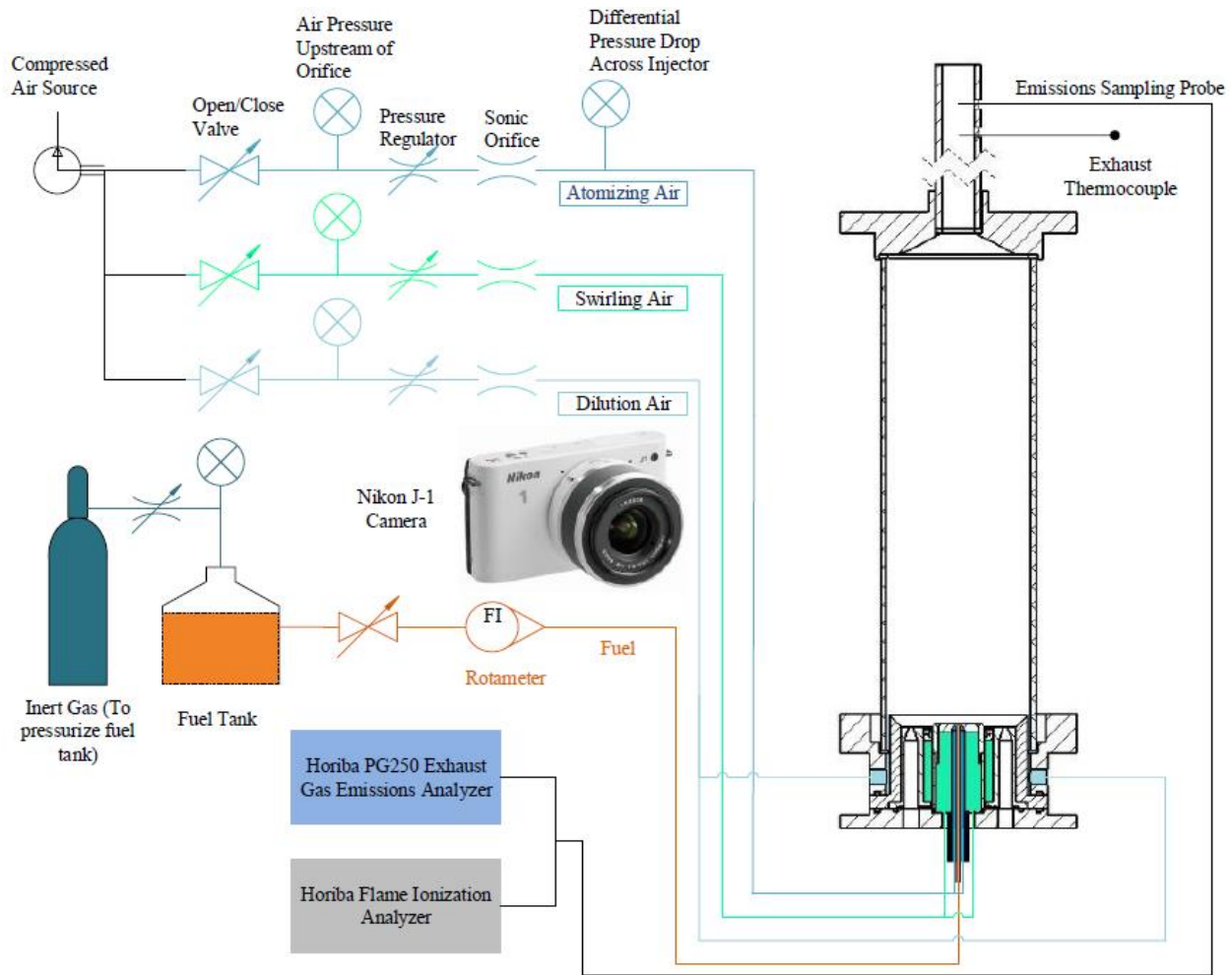
Figure 17: Combustion Rig Layout

An exhaust contraction section was developed to fully mix exhaust products funnel them through an exit pipe. The test combustor is mounted in an upright orientation. A graphite gasket was fit to the rim of the contraction flange in order to seal the reaction zone between the quartz tube and steel wall. Four all-thread posts shown in secured the contraction flange in place with

48

spring loaded nuts to absorb any expansive shocks that could damage the quartz liner.

Combustor setup and design specs are listed in below.

Table 3: Combustion Hardware Specifications

Part	Specification
Quartz Liner	9.0 in. length 2.95 in. OD x 2.75 in ID
Contraction Flange	137º
Exhaust Pipe	11.5 in. length 1.0 in. OD x 0.78 in ID
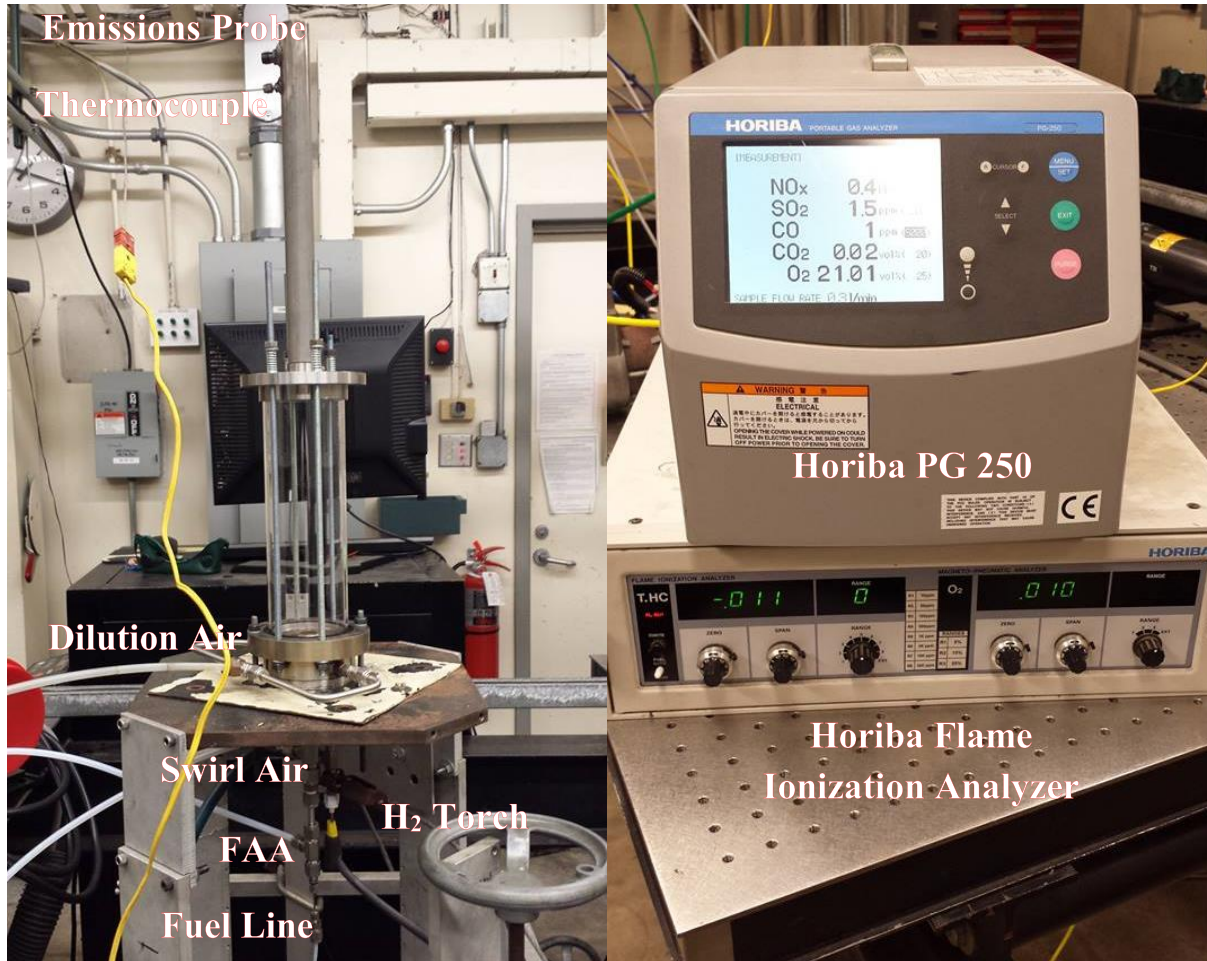
Figure 18: Combustion Layout (L) and Emissions Consoles (R)

Fuel was filtered on its way to the nozzle, fed via a tank pressurized with nitrogen. The mass flow rates were regulated by a Brooks R-2-15B rotameter. Rotameter calibrations were carried out for each fuel using a "catch and weigh" method. Trials at seven different rotameter settings took place in which fuel was poured into a graduated cylinder for 60 seconds, then weighed with a digital scale.

The three combustion air streams (FAA, swirl, and dilution air) are fed via a 150 psi compressed air manifold. From here, three lines branch out leading to pressure regulators and then appropriately sizes sonic orifices. With the pressure regulators controlling the upstream pressure to the sonic orifices, the three air lines were calibrated using laminar flow elements. In addition, the FAA line used a mercury manometer to measure the FAA differential pressure drop (ΔP_{FAA}) across the nozzle.

4.2.3. Emissions Consoles

This burner was commissioned to run long term tests in the lean combustion region. As such, a 30:1 fuel to air ratio was selected for operating with F-76. Researchers Legg & Narvaez appropriated flow rates for each air circuit to give the following operation conditions:

Table 4: Combustion Operating Conditions

ΔP_{FAA}	Fuel Atomizing Air	Swirl Air	Dilution Air	Total Air	F-76 Flow Rate		Global Equivalence Ratio	Heat Rate
kPa	kg/min	kg/min	kg/min	kg/min	kg/min	ml/min	--	kW
40.6	0.00368	0.0571	0.0402	0.101	0.0034	4.0	0.501	2.4

For each fuel in this study to be simulated in a "drop in" situation, the air flow rates listed in Table 4 are used for each fuel. Additionally, combustion tests took place under one optimal ΔP_{FAA}. In accordance with matching power output in the "drop in" scenario, fuel flows were set to match the 2.4 kW heat rate; these are based on the lower heating value (LHV) found for each fuel from MSGC analysis.

Prior to each test, the quartz liner was removed in order to clean the burner face, quartz tube, and contraction section with acetone wipes. This removed residual fuel and soot deposits which had been found to effect emissions readings. The burner was lit using a hydrogen torch and let run for 20 minutes to reach steady state operation. Emissions were pumped from the exhaust stream to a water dropout system to provide a dry sample to two emissions consoles. A Horiba PG250 emissions analyzer recorded CO, NO_x, O_2, and CO_2 measurements. NO_x and CO accuracy was noted as $\pm.25$ ppm and ±25 ppm respectively. A Horiba Flame Ionization Analyzer (FIA) was used to measure UHC emissions at ±10 ppm. After 20 minutes of operation, temperature and emissions measurements were recorded at 1-minute intervals for a 10 minute duration.

4.2.4. Flame Imaging

After obtaining emissions and temperature data, high speed videos of the flame were recorded. A Nikon J1 camera was used to capture color videos at 400 frames per second. A Matlab code was created to convert these high speed videos to grayscale and then produce a time averaged image. The code utilized 400 frames recorded over a 1s interval to create average images. In addition, the pixel intensities for each image were summed to provide a quantitative number for total image intensity which is related to the sooting propensity of a flame. The full code can be found in Appendix B.

4.2.5. Reaction Stability

Following high speed video capture, reaction stability for each fuel was determined based on the lean blow off limit (LBOL). To do this, researchers incrementally closed the fuel line control valve, while watching the rotameter float, until the reaction reached the extinction limit and ceased to fire and the fuel shut off valve was engaged. The burner was then re-lit with the hydrogen torch and allowed to reach its steady state temperature reading before another LBOL reading was recorded. Two researchers each recorded 3 LBOL points in order to remove observational bias.

4.3.   Atomization

Literature review from section 2.4 details the importance of atomization performance on combustion emissions. Fuels must be sprayed into droplets to aid in vaporization leading to combustion; this process is influenced by the physical properties of the fuel and the atomizer design and operation settings. In order to determine atomization quality for each fuel, the air-blast atomizer was mounted in a downward facing position wherein the spray plume was captured by a low velocity vacuum. From this, the fuel condensed into droplets through layers of steel wool wherein the droplets then accumulate into a dropout tank. The air-blast atomizer mounted in such a way to allow for optical access for a Phase Doppler Particle Analyzer (PDPA) and high speed camera, as seen in Figure 19.
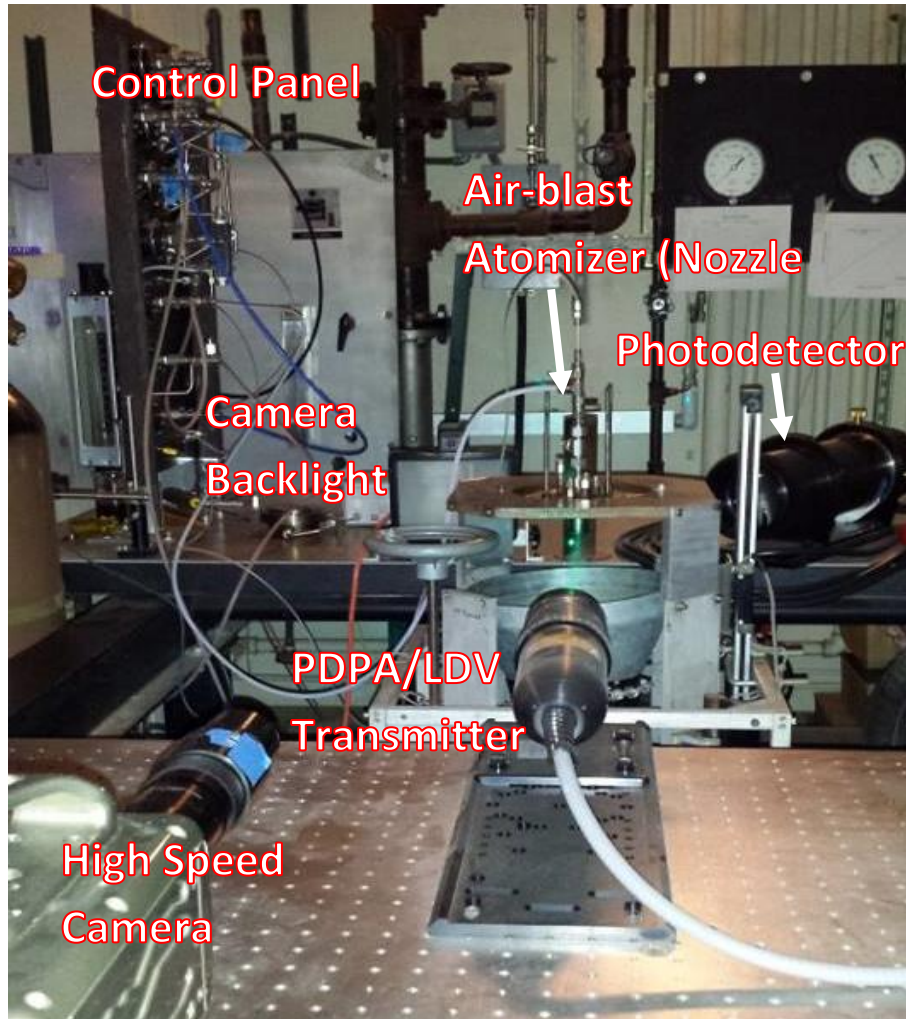
Figure 19: Picture of Atomizing Test Rig

Additionally, a traverse system was used to position the spray plume in various

locations relative to the laser system and camera. Spray behavior for the air-blast atomizer is

captured at three various pressure drop settings. This pressure drop was controlled by

repositioning the fuel rod and monitoring a mercury manometer. With the FAA regulating valve

held constant for each test, changing effective area is coupled with changing air mass flow rates,

listed in Table 5, which was measured with an air rotameter, shown in Figure 20.

Table 5: Atomizing Air Parameters for Spray Testing

Parameter	Units	Low	Medium	High
FAA Flow Rate	g/min	4.19	3.88	3.68
FAA ΔP	kPa	13.5	27.1	40.6
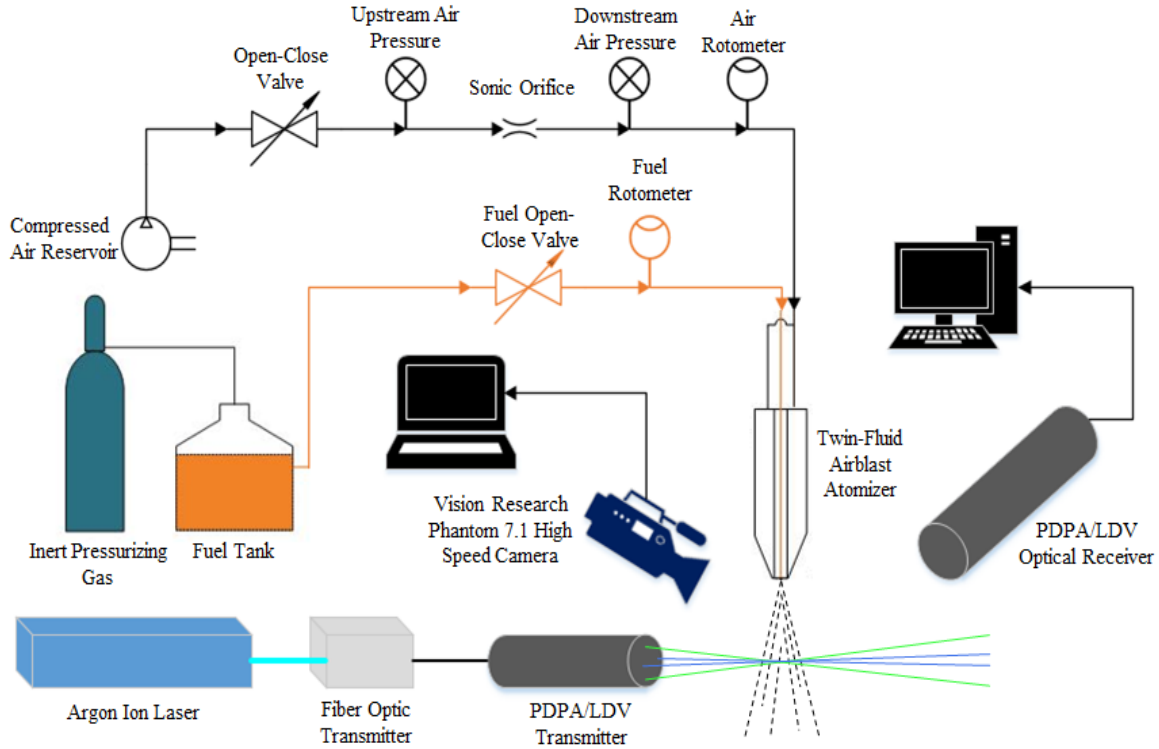
Figure 20: Schematic of Atomization Test Rig

4.3.1. Phase Doppler Particle Analyzer & Laser Doppler Velocimetry

Detailed atomization information was captured using a TSI FSA-4000 Phase Doppler Particle Analyzer (PDPA)/Laser Doppler Velocimetry (LDV) system. An Innova 90C Argon-Ion laser channels a beam into the TSI Fiberlight box where the beam is split into three pairs at specific wavelengths: green (514.5 nm), blue (488 nm), and violet (476.5 nm). Each wavelength corresponds to a velocity component measurement, wherein using all available beams enables

54

size measurements and 3-component velocity. A TSI fiberlight box focuses the beams into fiber-optic cables that connect to transmitters. The green and blue beams follow fiber-optics to a separate transmitter than that for the violet lasers; this secondary transmitter was not used in this study. The primary transmitter emits the laser pairs spaced 20 cm apart with the green and blue along the vertical and horizontal axes, respectively. A 500 mm lens focuses all four beams onto a single sampling point as depicted in Figure 21. The intersection point of each laser pair results in a fringe pattern – a series of light and dark fringes. Table 6 displays the relevant dimensions for the measurement volume, with the green and blue beams referred to channel 1 and channel 2, respectively. Equations used in calculating measurement volume dimensions can be found in Appendix A.
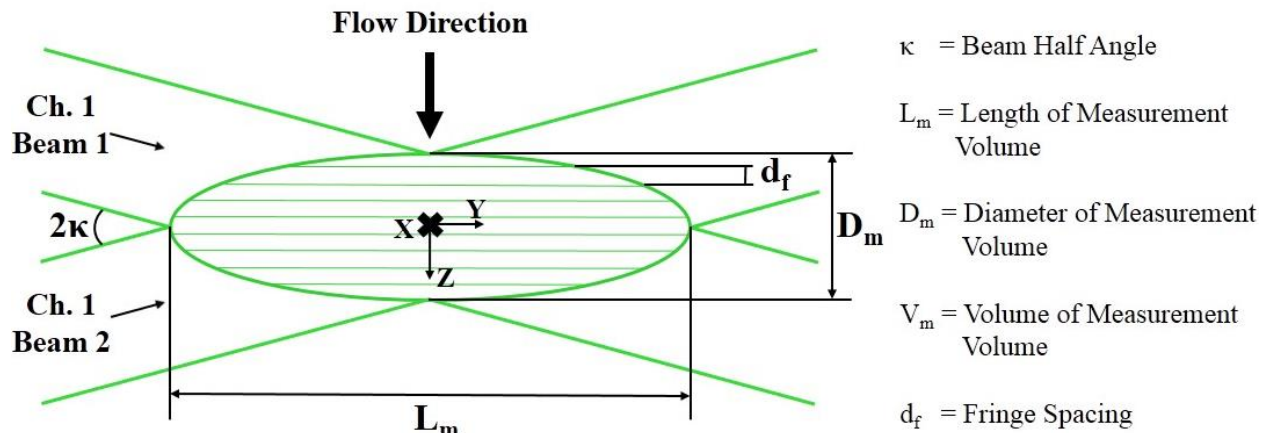
Figure 21: Channel 1 Measurement Volume Schematic

Table 6: Measurement Volume Parameters

Parameter	Channel 1	Channel 2
λ (nm)	514.5	488.0
κ (degrees)	1.145	1.145
L_m (mm)	9.254	8.777
D_m (mm)	0.1850	0.1755
V_m (mm^3)	0.1659	0.1416
d_f (μm)	12.86	12.20

A photodetector module set at 30º off axis of the transmitter captures light refracted off droplets passing through the sampling volume. For these experiments, the photodetector was equipped with a 500 mm front lens and a 50 μm slit. The scattered light is collected by the photodetector and converted to electric signals by photomultiplier tubes.

LDV data are captured as particles move over the fringe pattern in the control volume. This resultant fluctuating pattern of scattered light intensity is received as a frequency. However, to enable differentiation of flow direction, a Bragg cell shifts the frequency of one beam by 40 MHz, resulting in fringes moving at 40 MHz in the reverse flow direction. Frequencies transmitted from the photomultiplier tubes have a frequency of either above or below 40 MHz, depending on their direction. The calculated Doppler frequency (f_d) difference between the particle and Bragg cell frequencies is proportional to the particle velocity (u) and the fringe spacing.

$$u = d_f \, f_d \qquad\qquad (4\text{-}2)$$

PDPA for particle sizing is an extension of the LDV techniques. To gather LDV data, only one detector is required. However, sizing measurements require at least two detectors and the TSI photodetector is equipped with three detectors within the receiver. This allows for two independent size measurements for redundancy as well as an improved dynamic size range with high sensitivity. The PDPA technique calculates size information based on the spatial frequency of the scattered fringes. Another important sizing feature provided by the PDPA system is a measurement of the scattered light intensity for each particle. These measurements are important in eliminating erroneous size measurements and providing a better characterization of the measuring volume size, which is useful in calculating certain flow parameters.

56

The traverse system was calibrated to place the coordinate origin at the nozzle orifice. Traverses were performed sufficiently downstream of the nozzle in a region where the spray had become fully developed with spherical droplets as is a requirement for the PDPA system to record valid readings.
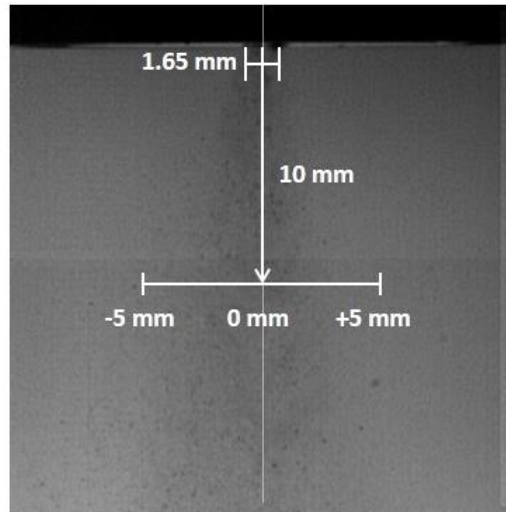
Figure 22: Scaled View of Spray Traverse Paths

Due to the low flow density for the air-blast nozzles, axial traverses were taken across the entire width of the spray plume. Data were collected at each point until the software recorded $1x10^5$ samples, or reached 90 seconds of data collection.

4.3.2. Phantom High Speed Camera

High speed shadowgraph images were captured using a Vision Research Phantom 7.1 digital high speed camera. Videos were recorded in 256x256 pixel resolution at 26143 fps. High speed videos and extracted stills were used to provide qualitative insight into spray behavior.

5. Results and Discussion

This section details the results of tests performed in this study. All conditions were set to match the operation settings for the F76 distillate. All flow situations occurred at atmospheric pressure, with inlet fuel and air at ambient temperatures 20° C.

5.1.   Fuel Properties

5.1.1. Physical Properties

The three measured physical properties of importance for this study are density, viscosity, and surface tension as they directly relate to the atomization process. Histograms displaying density, surface tension, and viscosity are displayed with their respective standard deviations.
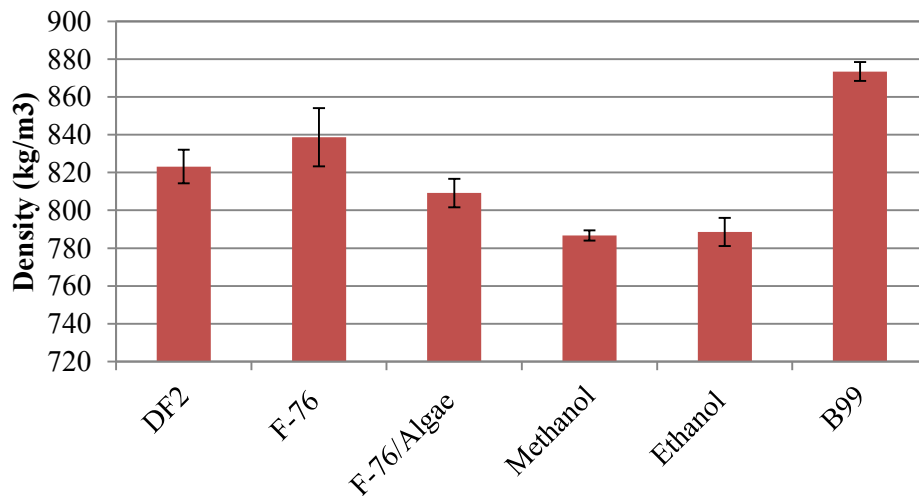
Figure 23: Measured Density for Fuels of Interest
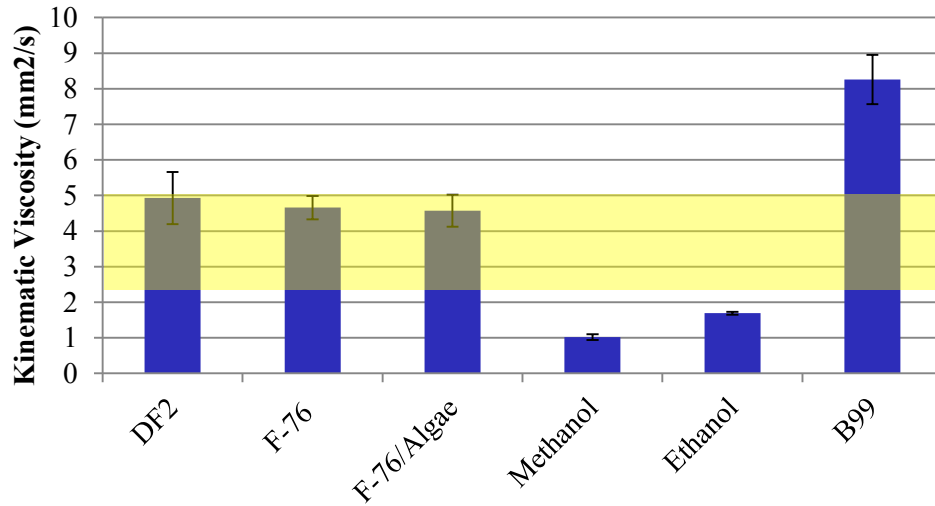
Figure 24: Measured Kinematic Viscosity for Fuels of Interest With the Yellow Band Depicting the F-76 Specification Range for Viscosity
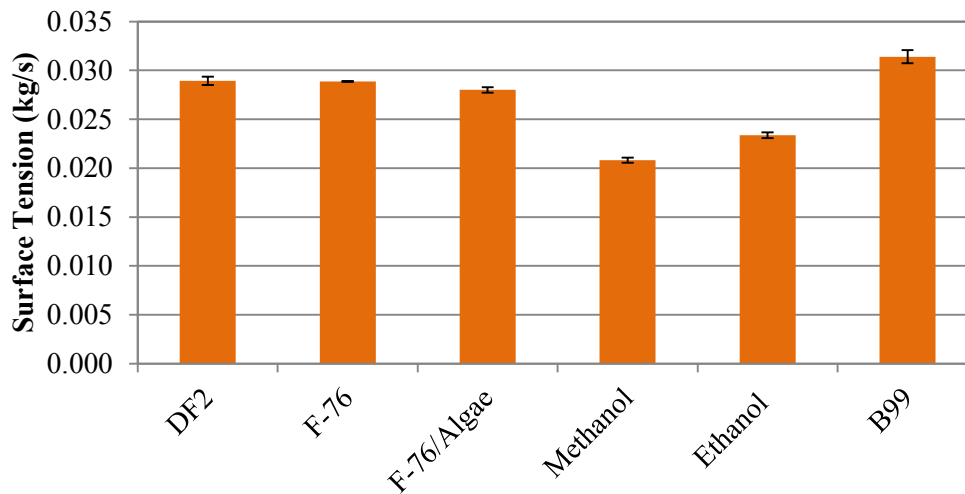
Figure 25: Measured Surface Tension for Fuels of Interest

There are significant density differences between each of the fuels. The two base fuels DF2 and F-76 have essentially similar densities, while that of the F-76/Algae blend is reduced. Methanol and ethanol are the lowest density fuels in this study, and B99 possesses the largest density, implying heavier fuel loads during transport. Thorough review of ASTM fuel standards led to no findings for fuel specifications needing to be met in order to be used as a "drop-in" fuel

in conventional turbine systems. As such, F-76 specification MIL-DTL-16884L (see Appendix D) will be used as a rough guide to compare the renewable fuels with conventional ones, being that most of the specifications relate to operability aspects such as contaminant levels, ignition quality, and corrosion propensity. F-76 distillate specifications provided by ONR place a density ceiling at 876 kg/m^3; all 6 fuels here fall within the acceptable range.

For viscosity and surface tension, it is seen that F-76 and DF2 both exhibit similar values, with the F-76/Algae having slightly lower properties. Methanol shows to be the least viscous fuel along with the lowest surface tension, while ethanol follows closely. In accordance with previous literature review, B99 is highly viscous and has the highest surface tension. While there is no stated acceptability range for surface tension, viscosity is stated to lie between 1.7 and 4.3 x 10^{-3} kg/m s (2.03 – 5.13 mm^2/s) at 40º C. At the ambient measurement conditions, it is seen ethanol, methanol, and B99 do not meet these requirements. These initial findings indicate that B99 will display difficulty during atomization, and that F-76/Algae might possibly atomize more effectively than the base fuels. Methanol and ethanol's low physical properties would indicate superior atomization as compared with the other fuels, however their low densities would indicate higher required volumetric flow rates.

5.1.2. Fuel Composition

Information on the chemical makeup from MSGC collected by researchers Bolszo and Legg is used to characterize all fuels except methanol and ethanol, being single composition fuels. Their results chart the mass fractions of major chemical species present in each sample. Being derived from various feedstocks, the chemical composition of biodiesels can vary greatly.

Presented in Table 7 below is the mass composition of the four main fatty methyl ester chains present in B99 along with their respective enthalpy of combustion (NIST 2011).

Table 7: B99 Mass Composition from MSGC (Bolszo 2008)

Fatty Acid Composition	Species	Enthalpy of Combustion (kJ/kg)	Mass Fraction (%)
Linoleic (C18:2)	$C_{19}H_{34}O_2$	39512	49.49
Oleic (C18:1)	$C_{18}H_{34}O_2$	39574	44.43
Palmitic (C16:0)	$C_{16}H_{32}O_2$	39009	4.35
Stearic (C18:0)	$C_{18}H_{36}O_2$	39751	1.74

The influence of the chemical structure of fatty acids composition on biodiesel physical and chemical properties is crucial in predicting combustion behavior. Correlations between chemical chain length and emissions have been identified. It has been found that NO_x exhaust is reduced with the reduction in mean carbon chain length, while CO and UHC emissions behave inversely. It has also been speculated that the main factor affecting PM formation is oxygen content (Pinzi et al. 2013). The B99 of interest is largely composed of long chain fatty acids which could lead to high NO_x and lower CO and UHC emissions, typical of results from various literature. MSGC results for F-76, DF2, and F-76/Algae produced a much larger array of chemical compositions (over 23 different hydrocarbon constituents). The overall longer carbon chain length in B99 translate to higher carbon-to-hydrogen ratios than for the F-76, DF2, and F-76/Algae, displayed below. Information on the thermodynamic and chemical compositions for methanol and ethanol were obtained from the NIST database (NIST 2011).

61

Table 8: Fuel C-H-O Composition

Fuel	Approximate Chemical Formula	C-H Ratio	Oxygen Content (% Mass)
DF2	$C_{15.43}H_{32.22}$	0.47	0
F-76	$C_{14.64}H_{30.40}$	0.48	0
F-76/Algae	$C_{15.95}H_{33.05}$	0.48	0
Methanol	CH_3OH	0.25	50.00
Ethanol	C_2H_5OH	0.33	34.78
B99	$C_{18.76}H_{34.58}O_2$	0.54	10.97

With the given mass composition of each, approximate chemical formulae were

assembled to represent each fuel (Legg 2012). In addition, an overall enthalpy of combustion

was calculated based on the mass fraction and data from the NIST Chemistry WebBook. Using

this, appropriate flow rates displayed in Table 9 were determined in order to match the

theoretical power output of 2.4 kW. Adiabatic flame temperatures were calculated using an

equilibrium calculator based the equivalence ratio, enthalpy of reactants, and chemical formulae.

Table 9: Chemical Formulae and Flow Rates for Each Fuel

Fuel	Lower Heating Value (kj/kmol)	Volumetric Flow Rate (ml/min)	Φ	Adiabatic Flame Temperature (K)
DF2	9.281E+06	4.10	0.496	1526.1
F-76	8.778E+06	4.06	0.501	1522.7
F-76/Algae	9.583E+06	4.19	0.498	1530.5
Methanol	6.438E+05	9.12	0.458	1483.8
Ethanol	1.242E+06	6.79	0.476	1493.1
B99	1.087E+07	4.34	0.468	1453.8

One can see the similarities between DF2, F-76, and the F-76 algae blend as they share

like heating values and require roughly the same volumetric flow rates. In addition, these three

fuels exhibit the greatest AFTs, correlating with the largest equivalence ratios. Of the alternative

fuels, the F-76/Algae shares the most parallels with the two conventional fuels, indicating that it

is likely to perform comparably. B99 requires only a slight increase in volumetric flow rate, while methanol requires over double the volumetric flow required for F-76. It is noted that methanol has the highest oxygen concentration by mass and the lowest C-H ratio, followed by ethanol and B99. This is reflective of the associated heating values.

5.2.   Base Fuel Combustion Results

This section details the combustion performance of the 6 base fuels in steady state reacting conditions. Note that all reported emissions are corrected to 15% O_2 and are displayed with associated error bars representing a 95% confidence interval.

5.2.1. LVBR Combustion Characterization

Prior to testing all fuels, it was of interest to run the LVBR over a range of operation conditions to note the behavior of the hardware. The gaseous pollutant data displayed in Figure 26 were gathered over a continuous burn period wherein the fuel line was set at three different flow rates with the air circuits unchanged.
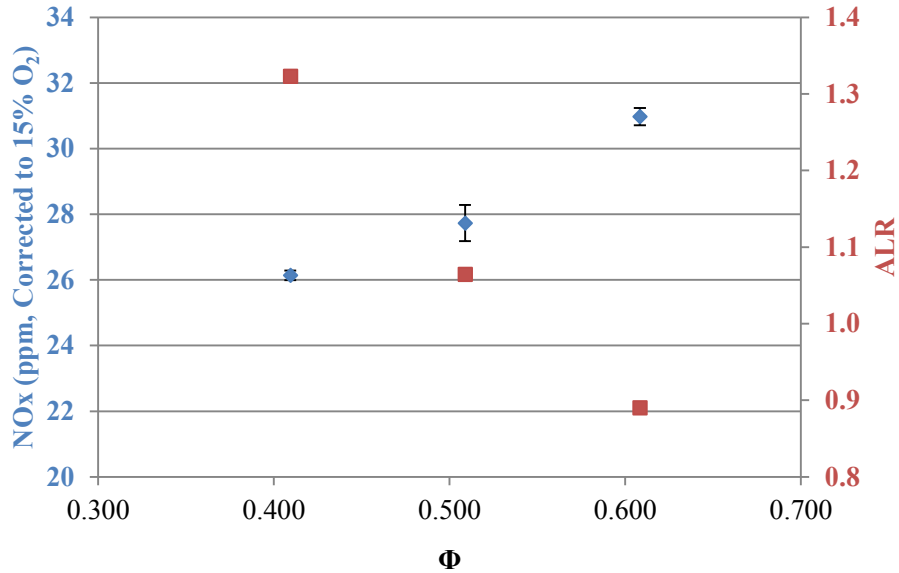
Figure 26: F-76 NOx Emissions and ALR at Varied Φ

Although this study does not specifically investigate the prominence of each mechanism of NOx production, several comments can be made. The increase in equivalence ratio is brought on by increasing the fuel mass flow rate. Increasing the fuel mass flow leads to decreases of the ALR through the nozzle. Equation 5-1 shows en empirical equation found by Rizk and Lefebvre (1984) that predicts SMD values for a plain-jet air-blast atomizer.

$$\frac{SMD}{d_o} = 0.48 \left(\frac{\sigma}{\rho_A U_R^2 d_o}\right)^{0.4} \left(1 + \frac{1}{ALR}\right)^{0.4} + 0.15 \left(\frac{\mu_L^2}{\sigma \rho_L d_o}\right)^{0.4} \left(1 + \frac{1}{ALR}\right) \qquad (5\text{-}1)$$

d_o = Characteristic Diameter

ALR = Air to Liquid Ratio

U_R = Relative Velocity between Fuel Jet and Fuel Atomizing Air

ρ_A = Air Density

ρ_L = Liquid Density

σ = Liquid Surface Tension

μ_L = Liquid Dynamic Viscosity

64

As seen by equation 5-1, decreases in ALR should result in increased droplet sizes. Larger droplets accompanied with "envelope" flames, discussed in section 2.4, create local hot spots at near stoichiometric conditions. These large droplets also require more time for complete evaporation, which in turn sustains the local hot zones for longer durations. In addition, increased fuel flow results in higher AFTs, thus two sources that lead to increased NO_x with Φ through the thermal production pathway. Of the four NO_x pathways, the fuel bound N_2 route can be neglected as there was no N_2 found through the MSGC analysis.

CO and UHC emissions are depicted in Figure 27 on the same graph as the two pollutants are closely linked in their production, with UHC being a precursor to CO.

Figure 27: F-76 CO and UHC Emissions for Varied Φ

As the equivalence ratio is increased for each case, CO and UHC levels both drop, behaving inversely with NO_x formation. CO and UHC emissions are influenced by a few factors, namely combustion zone temperatures and residence times. Increased temperatures

65

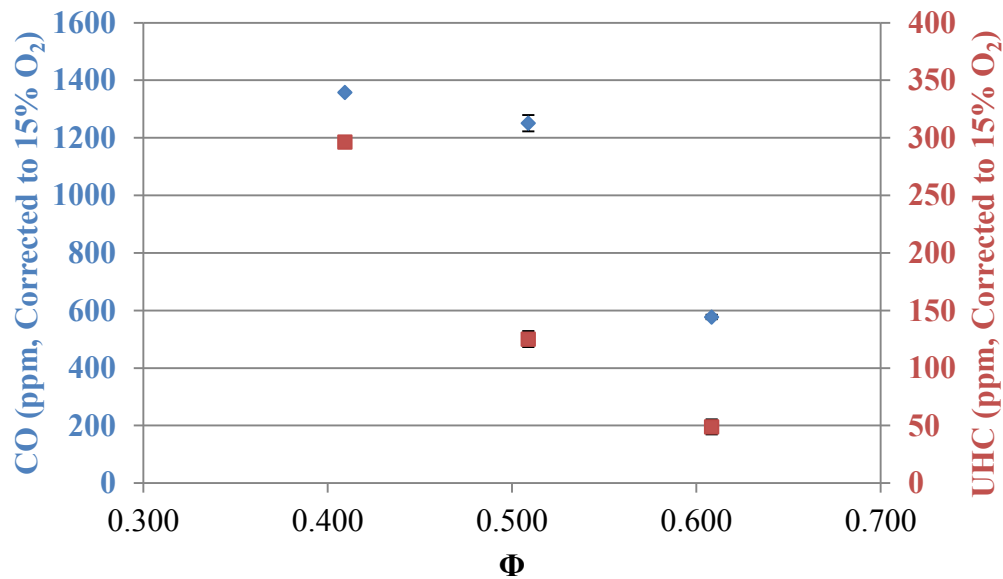associated with higher Φ aid in the destruction of CO and UHC radicals. Figure 26 also illustrates how the ALR is increased for lower Φ, implying that the atomized fluid emerging from the nozzle is imbued with higher velocities due to increased momentum transfer from the FAA to the liquid jet during the prompt atomization process. These faster moving droplets experience reduced residence times where CO has less opportunity to be oxidized to CO_2. CO and UHC radicals have limited time in the main combustion zone before reaching the contraction and exhaust section where unreacted wall dilution air is rapidly mixed exhaust products, effectively quenching any reactions.

The relatively high emissions reported in Figure 27 should not be surprising. The incoming air and fuel lines are not preheated, thus a significant portion of the released thermal energy is devoted towards evaporating the fuel and heating the large amount of air due to the lean operating conditions. This effect is increased by the lack of insulation to the combustion chamber. Heat loss at the quartz liner provides a relatively cool surface wherein reacting droplets escaping the recirculation zone meet the wall and are essentially quenched. Again, small droplets at high velocities have increased likelihood of migrating towards the wall and other cool zones.

A prominent strategy in the abatement of CO, and UHC emissions is operating at elevated pressures. Pressure plays a role in the formation of pollutants through its effect on reaction kinetics. In accordance with Le Châtelier's principle, increased pressures inhibit chemical dissociation and drive greater oxidation rates from CO to CO_2. With this being an exothermic reaction, CO is essentially unburnt fuel. These added reactions increase global temperatures which serves to react UHCs. Overall, this burner displays typical behavior for liquid combustors operating at lean conditions. Emissions follow the standard NO_x-CO (&

UHC) tradeoff, with droplet sizes partially influencing emissions behavior seen in Figure 4 and Figure 5. While most gas turbine combustors operate around 15-30 atm, whereas the LVBR runs at standard atmospheric pressure. The reported cases at ambient conditions serve as a first step analysis, thus experimentation of these fuels in a high pressure environment is suggested for recommendation in chapter 6.3.

5.2.2. Emissions

The most relevant quantitative information pertinent to the feasibility of alternative fuel use is that extracted from its combustion emissions. As gas turbine operators are subject to meet emissions standards set forth by the EPA, any replacement fuels must additionally meet these requirements. However, it is not only of concern in this study to discern the viability of such fuels, but to hopefully discover improved performance in regards to emission levels. As each fuel was testing in identical conditions set for F-76, all results are compared using the F-76 case as the control fuel. The first of such emissions discussed are those of CO and UHC, displayed below.
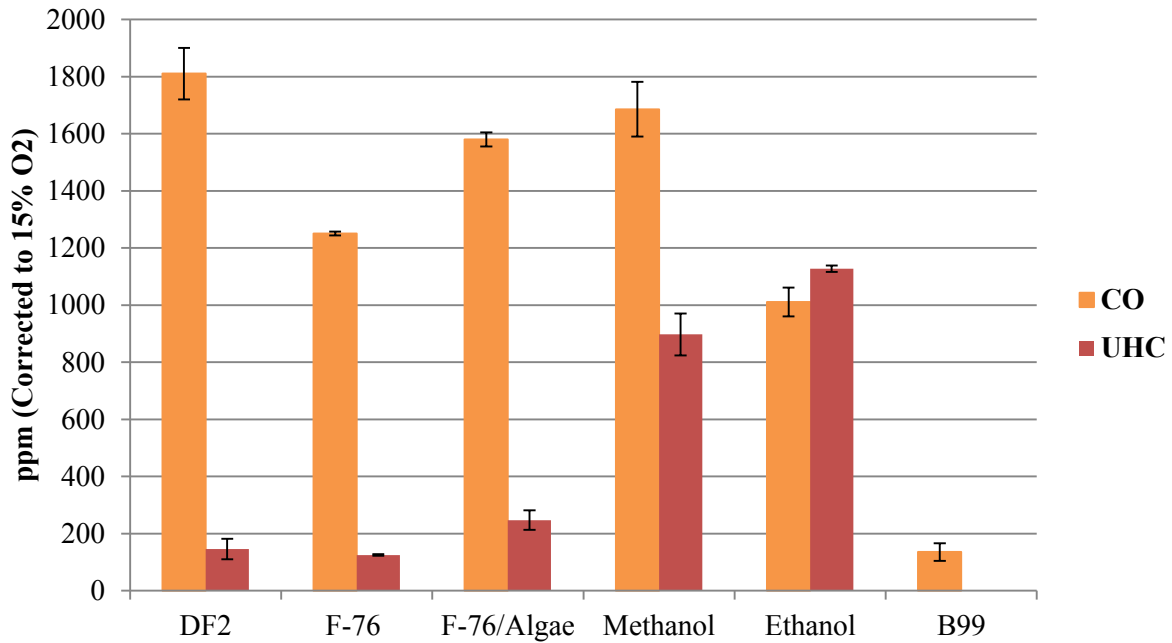
Figure 28: CO and UHC Emissions for Base Fuels

All the above fuels displayed widely varied CO levels. Among the pure petroleum and the F-76/Algae blend, the F-76 displays the lowest CO and UHC emission levels. Among the oxygenated fuels, methanol produced the highest CO emissions, and relatively high UHC. Ethanol additionally has large emissions of both products, while the B99 performs the best out of all the fuels. There are several factors influencing these emissions, namely combustion zone temperatures and residence times. During testing, cold wall interfaces proved to be a large contributor to CO and UHC pollutants due to fuel accumulation. This effect was most evident for the first 3 fuels. Below are photos of a combustor sections before and after a testing session of the F-76.
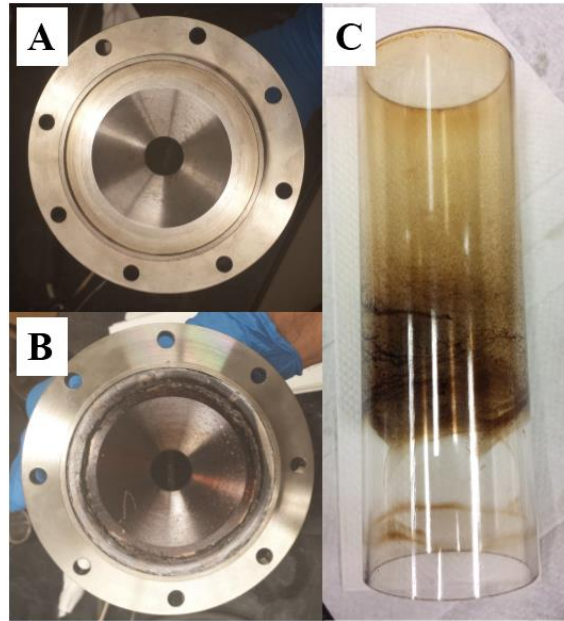
Figure 29: [A] Contraction Flange Before Test [B] Contraction Flange After Test [C] Quartz Tube After Test

In ramping up from light off to steady state conditions, growing fuel deposits on wall surfaces were observed. After sufficient time, CO and UHC levels tapered off and stabilized as combustion chamber deposits (CCD) became saturated. Of the different parameters affecting CCD (fuel type, surface material, pressure, combustion chamber environment), temperature is recognized as one of the most important factors (Arifin & Arai 2010). With this combustor being un-insulated, the effect played a large role in emissions levels for the petroleum based fuels. Caceres et al. found NO_x, CO, and UHC emissions dependence on CCD in a deteriorating manner (Cacares et al. 2003). The two alcohols have considerable CO and the largest UHC emissions, even though they are oxygenated. It is known that fuel bound oxygen typically undergoes more complete combustion, however this effect is overtaken by the sufficiently large flow rates required to meet the power demand. The large amount of fuel volume entering the combustion chamber does not have sufficient residence time to undergo complete reaction kinetics. More details of this outcome can be explained by the atomization performance in

section 5.3.2. Of all the base fuels, B99 has the lowest output, with nearly no UHC products (< 4 ppm). Here the direct effect of fuel bound oxygen is seen for a case coupled with more reasonable volumetric flow rates wherein the majority of the fuel is able to fully react with the incoming oxygen. CO and UHC levels in exhaust can be equated to overall combustion efficiency (η_C) based on the amount of chemical bond energy entering and leaving the system. Figure 30 displays efficiencies for each fuel from the calculation method listed in Appendix C.
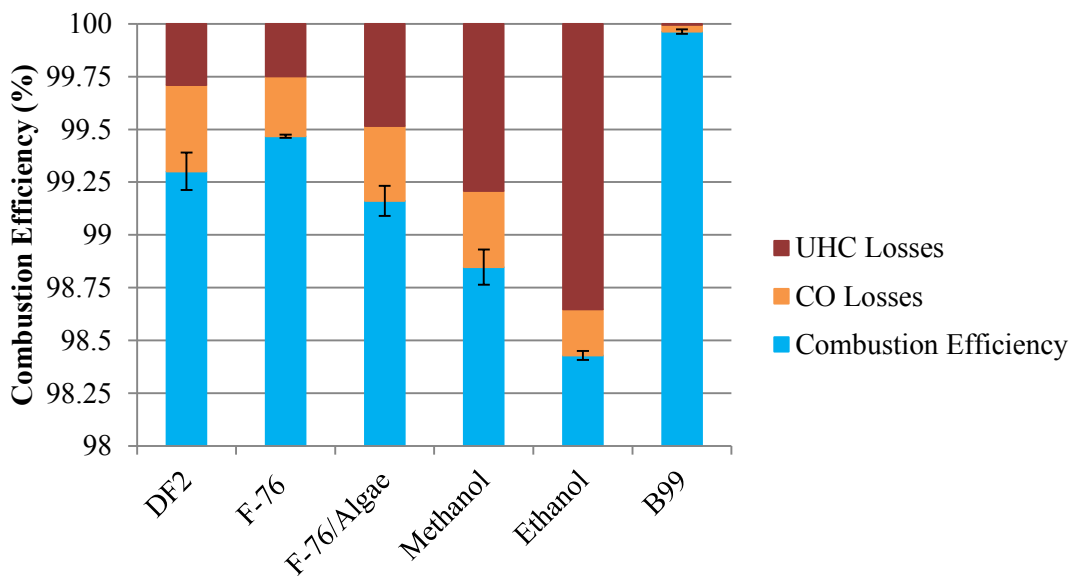
Figure 30: Combustion Efficiencies and Associated Losses

Both CO and UHC emissions correlate with their own efficiency loss term. In comparing the emissions with efficiency losses, one sees greater losses per ppm from UHC compounds. While B99 undergoes the most efficient combustion, F-76, DF2, and F-76/Algae perform similarly. This result is somewhat surprising given the expected larger droplet sizes for B99 due to larger viscosity and surface tension. Methanol and ethanol exhaust the largest amount of unreacted products where the efficiency from ethanol is roughly 1% lower than for F-76, a substantial amount that emerges in fuel utilization and costs. It is expected that all of the

oxygenated fuels would undergo more complete combustion, however the B99 performs better than the two alcohols due to its higher carbon to hydrogen ratio and lower flow rate. The effect of combustion efficiency plays into NO_x formation. Increased η_C results from less unreacted CO and UHC, equating to greater temperatures in the combustion environment and greater opportunity for NO_x production.
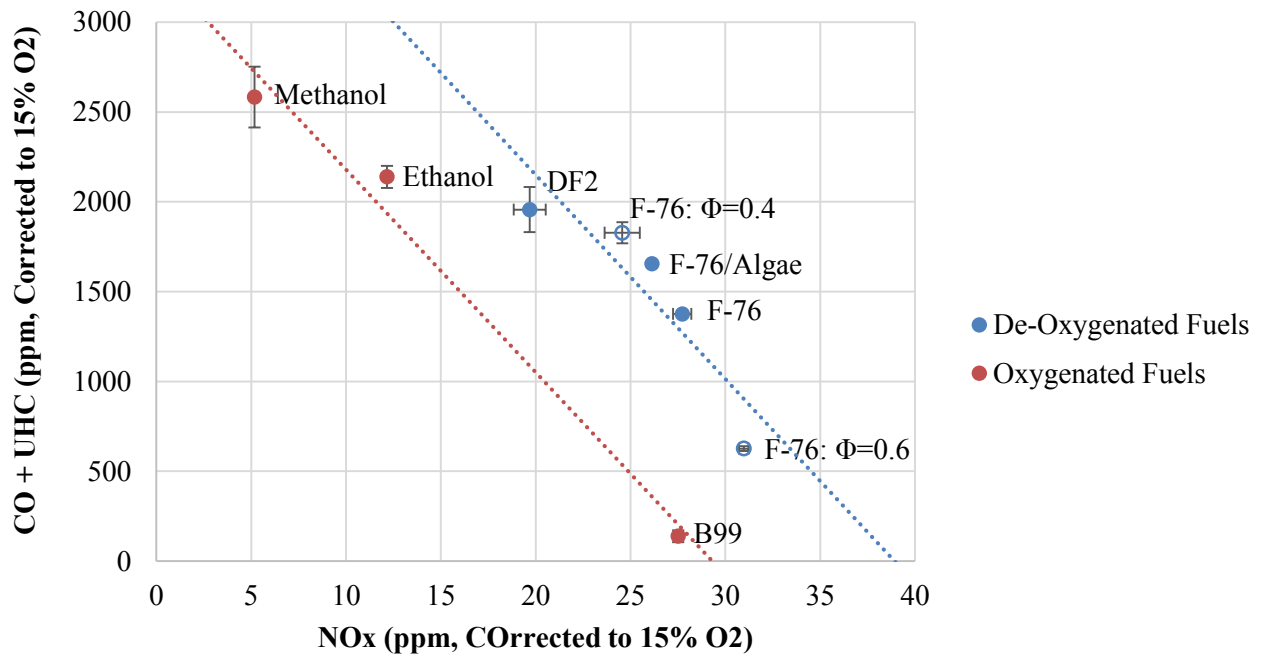
Figure 31: NOx vs. CO & UHC Emissions
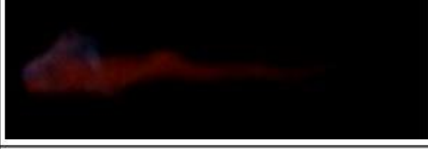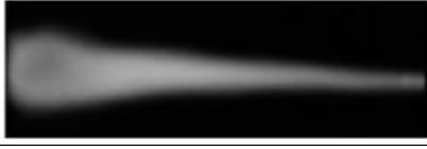
Figure 31 depicts the discussed tradeoff found in most combustion systems between NO_x, CO, and UHC emissions. The other 2 cases for F-76 operation are included in this graph in order to depict the consistent nature of this species exchange and create a better fitting trend line. Of the petroleum fuels, DF2 produces the least amount of NO_x at the cost of greater CO and UHC residuals. The F-76/Algae HRD fuel again performs much like the other petroleum fuels, making it a very suitable candidate as a "drop-in" fuel with predictable performance. Matching

71

with the highest η_C, B99 also produces the greatest amount of NO_x. Its production is statistically identical to that of F-76, however at a much lower CO and UHC. As expected from literature review, methanol and ethanol emit the least amount of NO_x. These two relatively simple compounds are highly volatile; this mixed with fuel bound oxygen promotes fast evaporation time and greater fuel/air mixing which simultaneously reduces temperatures and promotes generally lean conditions (Legg 2012). The roughly approximated trend line for the oxygenated fuels displays a desired effect. The red trend line is shifted directly left on Figure 31, indicating that for equivalent CO and UHC production to a petroleum fuel, the same operation could be achieved at lower NO_x levels.

5.2.3. Flame Visualization and Sooting Propensity

A large concern of combustion systems lies in the minimization of particulate matter, or soot. Specific hardware for quantitatively measuring soot concentrations was not used in this study, however flame imaging techniques do provide insight into soot production levels. Incandescent soot within reaction zones is the primary source of flame luminosity for diffusion flames. Soot also contributes to radiant heat losses from flames, and is generally produced in diffusion flames between 1300 and 1600 K, as are the flames in the current study (Turns 2012). Stills from high speed footage are shown beside a grayscale average of the flame in Table 10.

Table 10: Flame Images and Luminosity

Fuel	Color Snapshot	Gray Average	Total Image Intensity (10^9 Pixels)
DF2			2.45
F-76			1.93
F-76 /Algae			1.79
Methanol			0.28
Ethanol			0.36
B99			1.64

The images above indicate a slender, swirl stabilized flame extending down the length of the combustor. One can see from the color images that the DF2 produces a much more yellow flame than the other two petroleum based fuels. Post testing cleaning of the burner revealed soot deposits along with CCD for the DF2, F-76, and F-76/Algae blend. The F-76/Algae effectively displays less flame luminosity, possibly due to a lower smoke point than for F-76, however this explanation remains unclear as smoke point requirements are not listed in the specifications list in Appendix D.

www.manaraa.com

Soot formation in diffusion flames is strongly dependent on fuel type, which is clearly displayed in these findings. The three renewables methanol, ethanol, and B99 are all oxygenated compounds, leading to less fuel-rich regions where soot formation dominates. Lean premixed combustion environments are characterized by blue flames only seen with the latter three fuels. In addition, these fuels lack aromatic compounds that are found in the petroleum-based hydrocarbon fuels (Ballal Lefebvre 2010). In total, less soot is initially formed in the primary reaction zone, and more soot is oxidized in the secondary region. This is in concurrence with results as methanol has the greatest oxygen content, followed by ethanol, and B99.

5.2.4. Operation Range

From an operation standpoint, practical turbines are expected to run over a series of power output levels. It is desirable for fuels to be operable over a wide range. The lower limit of operation is set by the equivalence ratio at which the combustor can no longer sustain the reaction and the flame is blown out; this is termed the lean extinction limit. This limit sets the lowest power output available for each fuel in the current combustor.

74
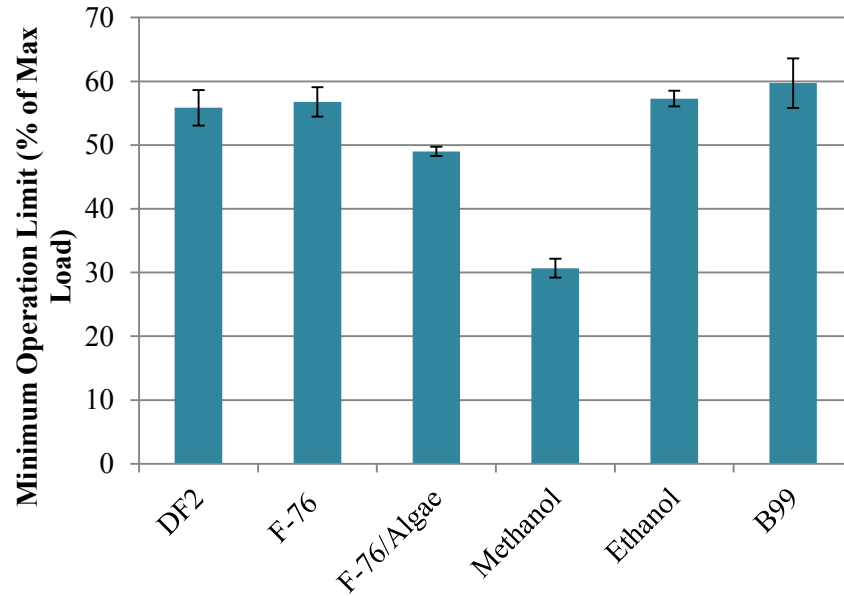
Figure 32: Minimum Power Operation

Lean extinction limits are influenced by a few factors: amount of recirculation induced by swirl, drop size, fuel volatility, combustor temperature, and fuel composition which is compared in Figure 32. Results in display nearly identical blow off limits between F-76, DF2, ethanol, and B99. The similarities between the two conventional fuels is not surprising given their comparable carbon to hydrogen ratios, however more variation between these and B99 and ethanol is expected. Of the many differences between operations of each fuel, temperatures created in the combustor play into these effects.

Table 11: Exhaust Temperatures During Steady Operation

	DF2	F-76	F-76/Algae	Methanol	Ethanol	B99
Exhaust Temperature (K)	962.0	944.7	991.8	902.7	822.8	1055.8
Error (K)	±12.9	±2.5	±7.6	±9.6	±1.1	±9.4

While B99 possesses a high heat of vaporization that aids in increasing temperatures to aid in evaporation, it has a lower fuel volatility. The F-76/Algae is able to operate at leaner conditions most likely due to differences in fuel composition as it relates to specific hydrocarbon compounds. The F-76/Algae is composed primarily of normal and iso-alkanes as compared with the pure petroleums comprised of cyclo-alkanes and benzenes. These reflect the presence of aromatic compounds with relatively complex hydrocarbon formations and increased carbon double bonds (Legg 2012). The reaction of these species creates a hotter combustion environment for the F-76/Algae which helps promotes droplet evaporation. Lastly, methanol exhibits a significantly lower extinction limit than for the other fuels. Initially methanol and ethanol are speculated to perform at near similar extinction levels given their high fuel bound oxygen content similar physical properties. However methanol outperforms ethanol largely due to greater combustor temperatures, the trend is reflected in the combustion efficiencies depicted in Figure 30. Increased oxygen bound in the fuel aids local mixing and promotes evaporation especially at these decreased fuel flow rates where the ALR is increased and atomization is improved. Of great importance here are atomization results, which are discussed later to help shed light on this.

5.3.   Base Fuel Atomization

To gain further insight into the combustion performance of each fuel, the atomization process is investigated. Atomization of liquid fuels plays heavily into the emissions and combustion efficiency as the droplets must be effectively broken up to increase evaporation and mixing rates. This section entails drop size information across the width of the spray plume,

providing detailed information across a region of interest. Additionally, high speed images are examined to provide more insight.

5.3.1. Fuel Injector Optimization

As discussed in chapter 4.4, modifications to the fuel tube geometry were made in order to optimize FAA flow near the nozzle exit. Figure 33 depicts the modified fuel tube after having a chamfered edge feature inserted.

Figure 33: Chamfered [L] and Blunt [R] Fuel Tube Comparison

Both the chamfered design and original blunt fuel tube were tested with F-76 at the high ΔP FAA conditions, with the results of their profiles mapped using the PDPA system displayed in Figure 34 below.

www.manaraa.com
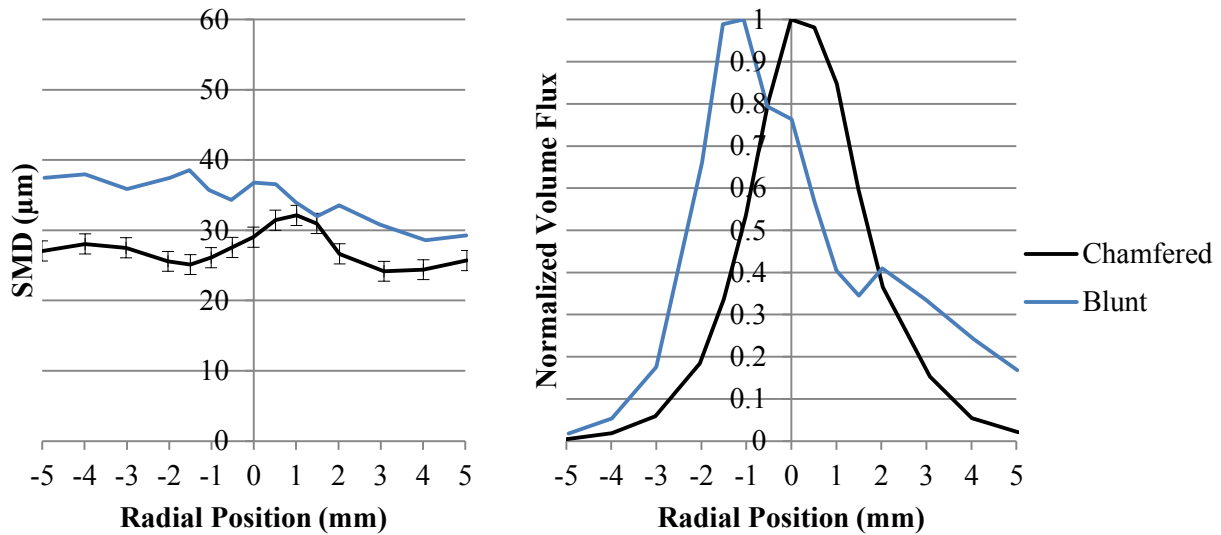
Figure 34: SMD [L] and Normalized Volume Flux [R] Distributions for Both Fuel Tube Geometries for F-76, High ΔP

Both SMD and volume flux distributions depict a more symmetric profile than is found for the blunt fuel tube. While the blunt tube produces a spray plume biasing larger droplets to the left hand side, the chamfered design allows for typical spray distributions found for air-blast atomizers. Volume weighted SMD results display a decrease in drop sizes from 35.1 μm to 28.9 μm, or a 17.6% decrease. Additionally, a less than ideal volume flux distribution is found that too is non-symmetric, with the maxima astray from the centerline. These improvements manifest themselves in the streamlined shape of the chamfered fuel tube. Prior to this alteration, FAA velocity flowing through the nozzle became impeded due to recirculation zones formed downstream of the sharp corner. The optimized fuel tube allows for effectively higher air velocities relative to the fuel jet emerging from the tube, enabling more effective breakup of droplets.

78

5.3.2. Velocity Measurements

Droplet residence time through the combustor is cited as an important factor in emissions and complete combustion. The PDPA system provides 2-component velocity measurements for each spray. As data were collected along the centerline of the spray, all droplets passing through the control volume have zero out of plane motion as they are being ejected radially outward from the nozzle orifice without swirling air. Velocity vector plots, displayed in Figure 35, for all three pressure drop settings were created in MatLab using the QUIVER function.
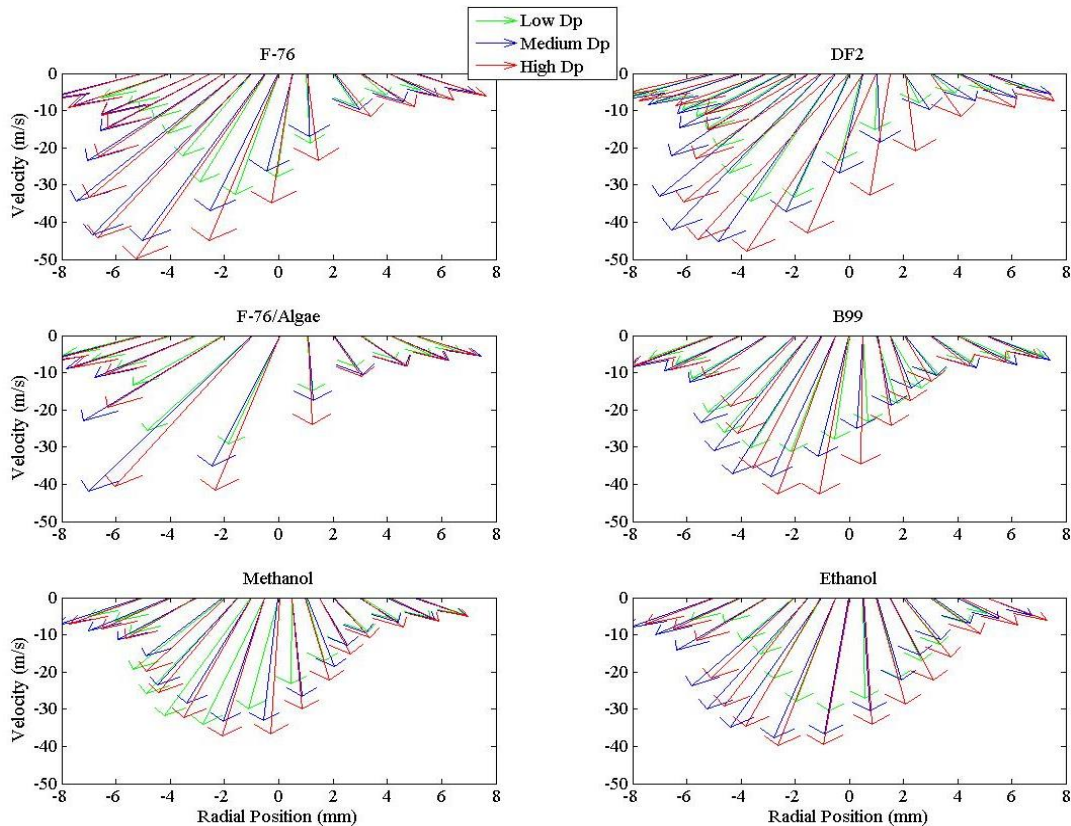
Figure 35: Velocity Profiles for All Three Pressure Drop Settings

The magnitude of the velocities associated with each fuel increase with the nozzle pressure drop, as per the Bernoulli equation. One notices that all fuels are ejected from the nozzle at a slight angle, contradictory to the expected behavior where the fuels would have zero

radial velocity below the nozzle, and then increase outward. This behavior is likely due to slight imperfections on interior surfaces, or imperfect centering of the fuel tube within the nozzle. This burner is scaled for relatively small flow rates, as compared with other experimental setups, and so too must the components be scaled down. Be it so, the behavior is consistent across all fuels. This angled injection could be a factor in elevated CO and UHC levels as droplets are more able to escape from the main recirculation zone and migrate towards the dilution air at the wall. One notices from plots that the vector magnitudes are not equivalent across each case. Similar velocity behavior is observed for DF2, F-76, and F-76/Algae where the maximum axial velocity approaches 50 m/s. As more fuel is injected, droplet velocities decrease as seen for the three oxygenated fuels. With methanol requiring the largest mass flow rate, noticeable slower moving droplets are observed, equating to increased residence times. However, this time is not sufficient to allow for complete reaction of the alcohols. One optimization strategy might be to decrease the nozzle pressure drop in order to allow for longer residence time, however this imparts an increase in drop size.

5.3.3. Droplet Sizing and Distribution

The Sauter Mean Diameter is used as the characteristic length to represent the atomization efficiency of each fuel. Figure 36 displays the SMD distributions for each fuel for each pressure drop setting. It should be noted that changing the nozzle pressure drop required adjustment to the effective area, which consequentially alters the FAA flow rate. However, this change is minimal, thus the effects of ALR on SMD sizing and spray plume distribution across all cases are small in comparison to the FAA relative velocity.

80
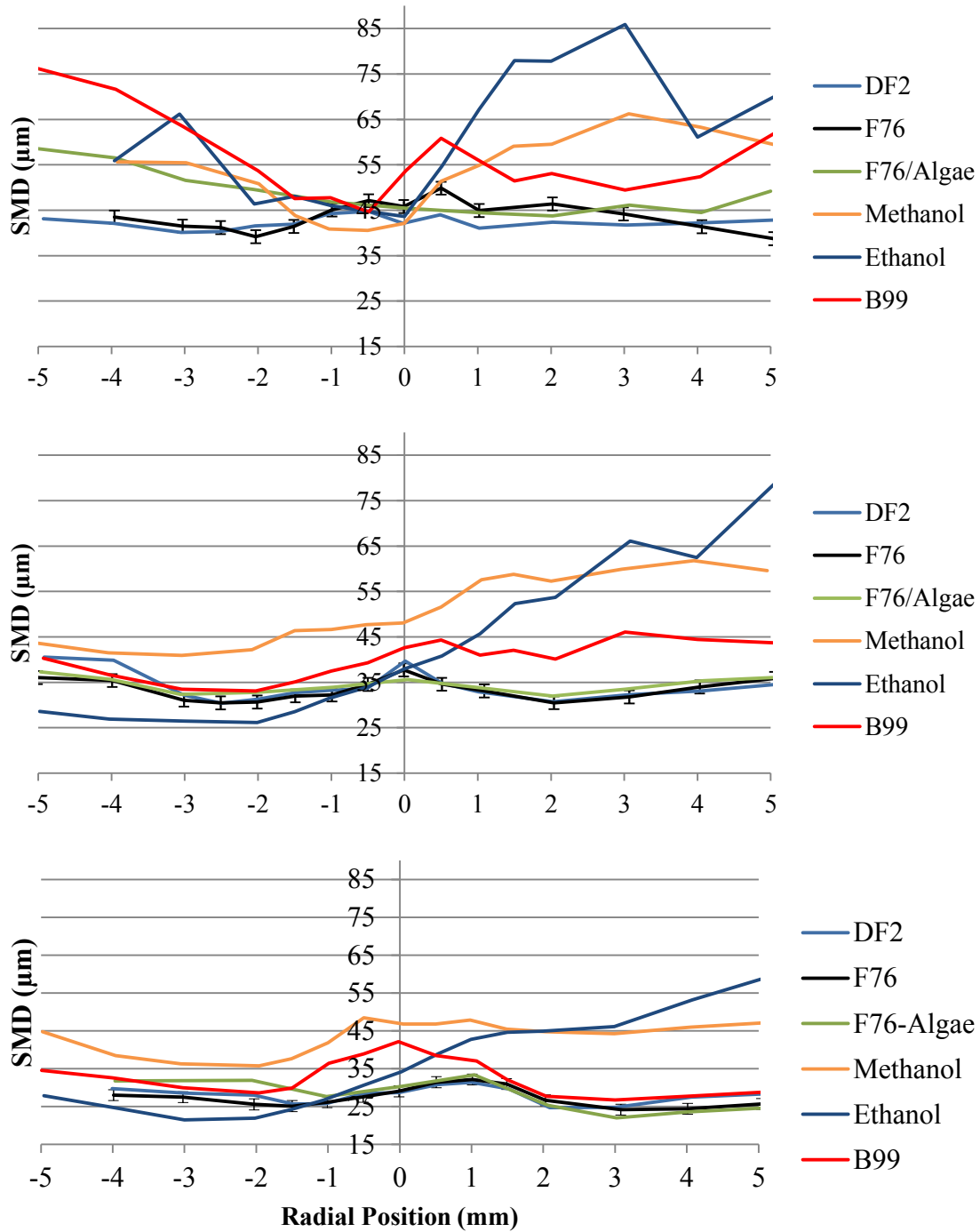
Figure 36: SMD Distributions from Low to High ΔP, Top to Bottom Respectively

Rizk and Lefebvre argue that the main mechanisms for breakup behind air-blast

atomization are mainly momentum and viscous forces. Again equation 5-1 is displayed below.

$$\frac{SMD}{d_o} = \varepsilon \left[0.48 \left(\frac{\sigma}{\rho_A U_R^2 d_o} \right)^{0.4} \left(1 + \frac{1}{ALR} \right)^{0.4} + 0.15 \left(\frac{\mu_L^2}{\sigma \rho_L d_o} \right)^{0.4} \left(1 + \frac{1}{ALR} \right) \right] \qquad (5\text{-}2)$$

Of the physical properties of the liquid, one notices from this equation that viscosity and surface tension are key factors influencing drop sizes. The first term of the equation regarding the aerodynamic breakup contribution, is heavily weighed by the relative velocity between the liquid and atomizing air. Figure 36 effectively demonstrates the impact of increased air velocities on drop sizes and SMD spread. Each fuel displays smaller SMD values with increasing pressure drop, and the size distribution becomes more uniform across the spray plume. Eventually at high ΔP, most fuel distributions assume similar shapes, with the largest SMDs found at the core of the spray. Refer to Figure 16 again in order to examine the physical interactions between the two fluids inside the nozzle. As the liquid fuel emerges as a solid cylinder from the fuel tube, it is impinged upon by an annulus of high velocity air. This air stream effectively shears off the outermost layers of the liquid jet into the smallest droplets, and the remaining air breaks up the rest of the intact core; this process of initial breakup is the prompt atomization stage. This is not the case for methanol and ethanol though. These fuels display unsymmetrical size distributions with greater SMD magnitudes as compared with the other fuels. In contrasting atomization performance with emissions for each fuel, the large CO and UHC contributions become more understood. The asymmetric and large SMD sprays observed with the two alcohols indicate poor mixing in the combustion chamber, with large droplets shed radially outward to the right hand side. These large drops likely escape the swirling air recirculation zone and become quenched by the wall cooling air. The other four fuels with more centered and well behaved sprays, all exhibit improved combustion efficiency. It seems evident that at lower ΔP where atomization effectiveness decreases substantially, increased emissions levels would be found.

The PDPA system is capable of measuring droplet volume flux passing through the control volume. These data, along with their corresponding SMD values are combined to create a volumetric weighted SMD average for the traversed line of sight through the plume.

$$SMD = \frac{\sum_i^n SMD_i \dot{\forall}_i''}{\sum_n^n \dot{\forall}_i''}$$ (5-3)

SMD = Volumetric Weighed SMD (μm)

SMD_i = SMD value at a specific location (μm)

$\dot{\forall}_i''$ = Axial Volume Flux at a specific location (ml/cm^2 s)

These overall SMD values are plotted in Figure 37 to give a more condensed summary of the results from Figure 36.
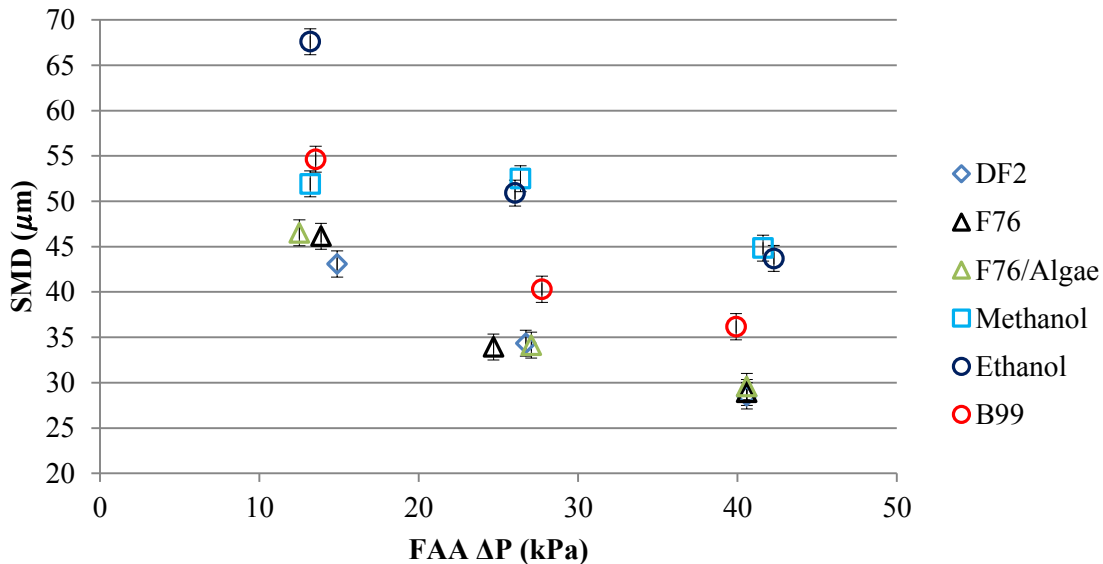
Figure 37: Volume Weighted SMD for All Fuels

The overall weighted SMD values more clearly describe the comparisons in atomization performance. Again, similarities in physical properties and flow rates between DF2, F-76, and F-76/Algae produce equivalent drop sizes across all fuels. Therefore differences in emissions are

83

due to differences in chemical composition. The B99 produces droplets on the order of 5 um

larger than the petroleum derived fuels. These consistently larger droplets, along with a larger

C-H ratio gives rise to the greatest NO_x production for all six fuels.

It is of interest to compare measured data theoretical predictions, namely those predicted

by equation 5-2. Because this equation was empirically derived, researchers have included a

modification constant ε in order to account for differences in experimental setup and data

acquisition techniques. The value for ε is determined by the average ratio between the calculated

and measured SMD values. Figure 38 displays the measured SMD values plotted against the

calculated values using equation 5-2 with the modifying constant ε=1.
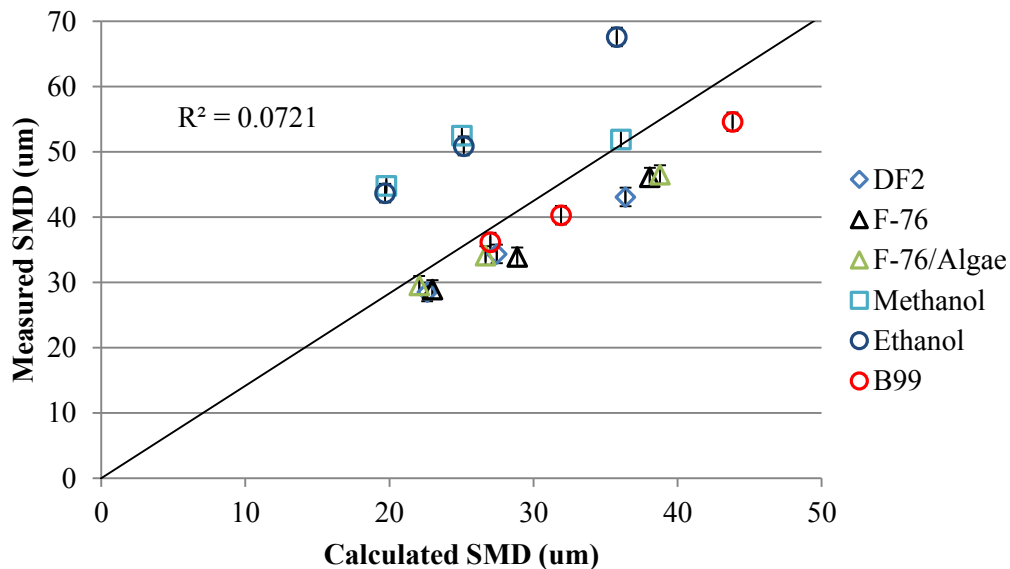
Figure 38: Measured vs Calculated SMD for All Six Fuels

A single trend line does a poor job of characterizing predicted size behavior for all fuels,

where methanol and ethanol deviate far from the trend line. Given the abnormal spray patterns

from the PDPA results, this finding is not entirely surprising. The context in which equation 5-2

was formulated must also be considered. Lefebvre developed this equation for low viscosity

84

fuels in a plain-jet air-blast atomizer for ALR values between 1 and 14 (Lefebvre 1989). The two alcohols are operated at ALR values less than 1 and produce larger SMD values than the specified range listed by Lefebvre. The equation is dimensionless until specified by a characteristic diameter d_o, which this study identifies this quantity as the diameter of the calculated effective area for the nozzle. After removing data points for the two alcohols, the trend collapse well onto a best fit line to provide a ε value for the LVBR.

$$\varepsilon = 1.25$$
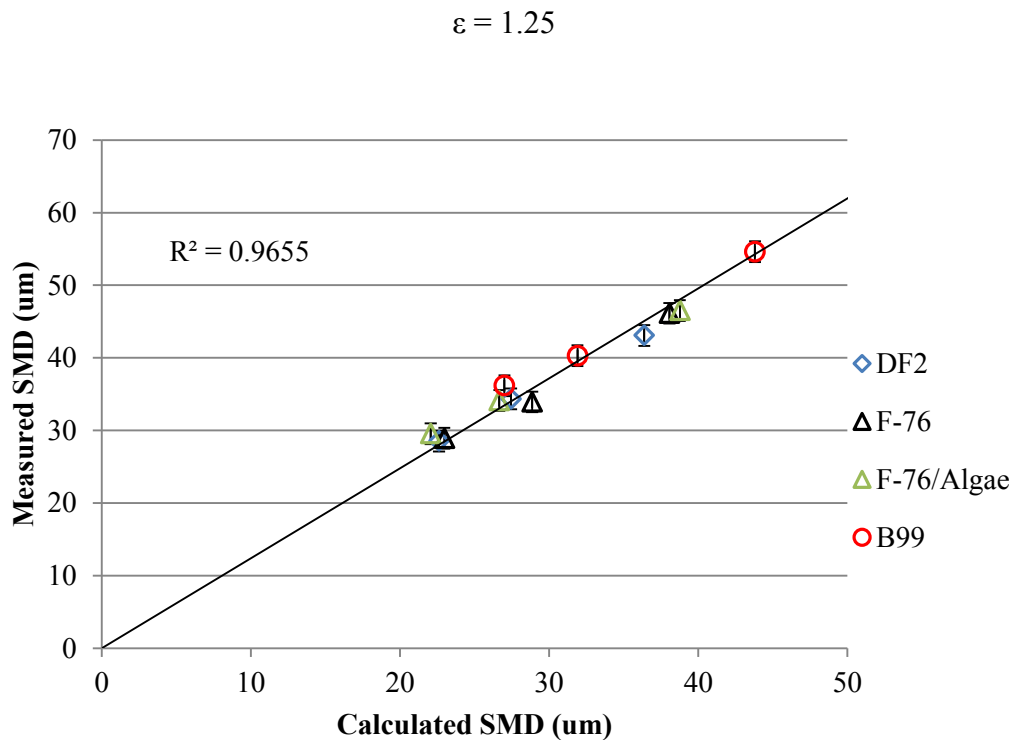
Figure 39: Measured vs Calculated SMD for Four Fuels

5.3.4. High Speed Shadowgraphy

High speed videos captured for each spray provide important qualitative insight to the behavior observed in data captured by the PDPA system. Stills from these videos are displayed

85

for the high ΔP case for which combustion tests took place. In these videos, shown in Figure 40, one is able to observe the liquid emerging from the nozzle orifice and propogating downstream.
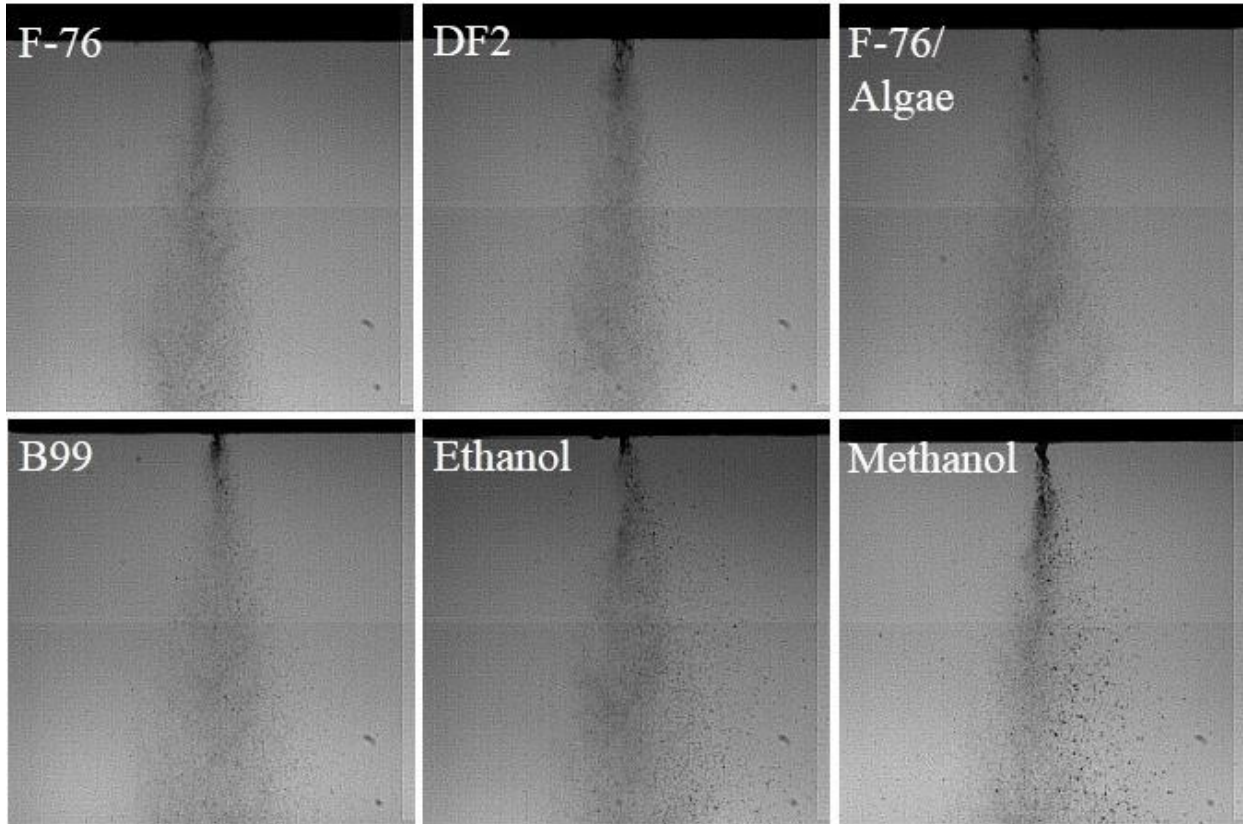
Figure 40: Shadowgraph Stills of Spray Plume

As observed in the LDV measurements, the three petroleum based fuels and B99 emerge from the nozzle at a slight angle. High speed recordings depict the fuel emerging from the nozzle in pre-formed droplets, indicating prompt atomization dominated by aerodynamic forces. Most notable from these images are the large droplets expelled into the spray plume by ethanol and methanol. Recalling that ethanol and methanol require roughly 60% and 115% more mass flow than F-76 in order to meet the 2.4 kW demand, significant reductions in ALR are observed. This reduction enables large amounts of fluid buildup at the nozzle exit. This fluid not atomized in the primary atomization stage is then shed off in ligaments in a secondary atomization phase.

These ligaments are atomized by the air flow following the primary liquid-air momentum exchange occurring near the liquid orifice inside the nozzle, leading to large droplets shed off to the right plane of the spray plume. The ethanol does experience a region of fine atomization to the left; however the larger droplets from accumulation are shed off to the right, increasing in a linear fashion across the spray. Methanol never experiences any region of finer atomization like ethanol and has poor overall droplet break up. Normalized volumetric flow distributions for the high ΔP case are displayed in Figure 41 where each data point is normalized by the sum of the volume flux data collected across each traverse. This figure displays how the fluid is dispersed into the spray plume. For the alcohols, the large droplets shed off to the right hand side demonstrate majority holding of the volumetric flow into the combustion chamber. These data, along with size distributions effectively explain the large drop in combustion efficiency for the alcohols. Studies on practical usage of alcohols in gas turbine systems demonstrate inability to competently perform well at full load, but observe improvements at part load near 60%. This conclusion would seem to carry over well to this small scale burner, wherein increased ALR for these fuels could dramatically improve atomization efficiency and spray symmetry.
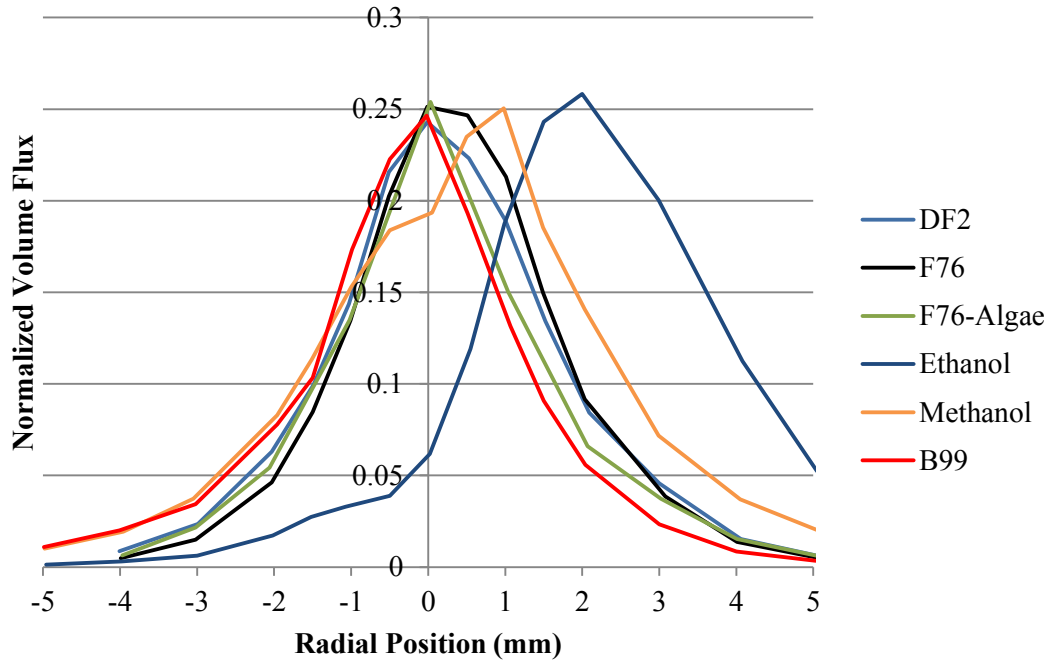
Figure 41: Normalized Volume Flux Distributions

5.4.   B99-Ethanol Hybrid Fuels

Blending strategies for B99 and ethanol are explored as a means to create a hybrid mixture that imparts performance behaviors from each fuel in an effort to enable a more balanced. Previous results determine that ethanol and B99 each entail certain drawbacks and benefits. B99 atomizes to form large droplets that become centers for high NO_x production, yet requires similar flow rates to meet power demands. Ethanol atomizes poorly as a result of low ALR, but higher oxygen content enables improved mixing and locally lower reaction zone temperatures for minimizing NO_x. Thus four B99-ethanol blends are studied to determine the effects of blending ratios on atomization and combustion performance.

88

5.4.1. Effect on Fuel Properties

The notion of ethanol blending to fuels creates a way to tailor fuels for combustion systems designed for conventional petroleums. The physical properties change with ethanol addition is measured in the same fashion as for the six base fuels.
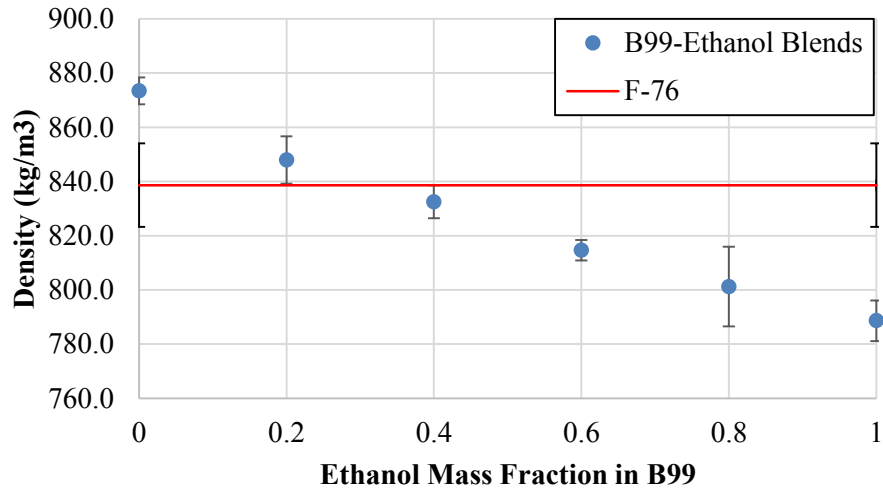
Figure 42: Density for various B99-Ethanol Blending Ratios
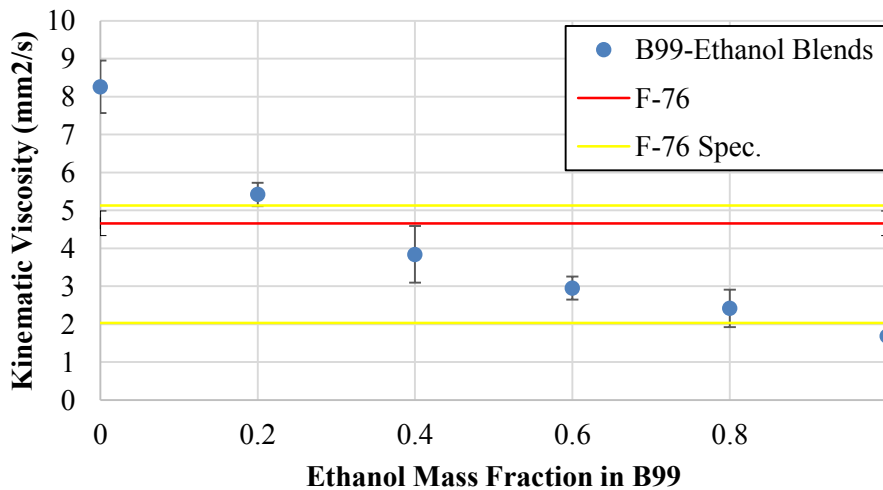
Figure 43: Viscosity for various B99-Ethanol Blending Ratios
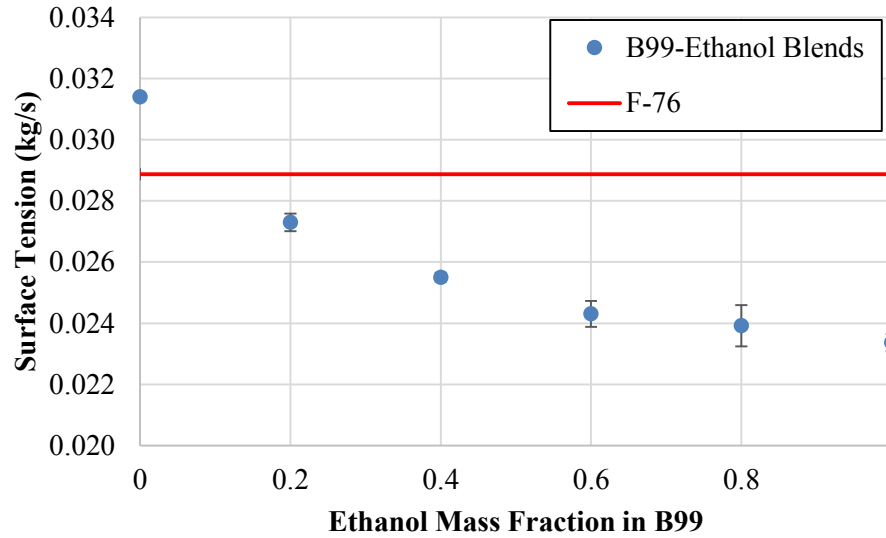
Figure 44: Surface Tension for various B99-Ethanol Blending Ratios

Ethanol is effective at lowering the physical properties associated with B99 for all mass fractions. Density decreases linearly for all fuel blends, as expected. This can positively influence the system by improving fuel preparation, however this drop will increase droplet sizes according to equation 5-3 (Bolszo 2007). In contrast to the linear change in density, viscosity and surface tension decrease more exponentially with a significant drop in both properties from B99 to the BE80 blend. It is observed that all four blends fall in between the viscosity range for the F-76 distillate, and all blends have lower surface tension values than the F-76. These gains, including increased oxygen content, come at the cost of increased flow rates, or an overall range reduction for transportation applications as depicted in Table 12. The pros and cons associated with each blend are explored in further sections.

Table 12: Changes in Composition and Flow Rates for B99-Ethanol Blends

	F-76	B99	BE80	BE60	BE40	BE20	Ethanol
C-H Ratio	0.481	0.542	0.497	0.454	0.412	0.372	0.333
Oxygen Mass Fraction (%)	0	10.9	15.7	20.4	25.1	30.0	34.7
Increase in Flow Rate (%)	-	6.8	18.8	29.0	39.7	52.3	67.3

5.4.2. Evaporation Behavior

Although ethanol and B99 are miscible with one another, it is critical to ascertain the stability limits of the mixtures as it pertains to long term storage in vehicles. Fuels could experience prolonged periods of time in which phase separation could occur, leading to an unknown change in composition and homogeneity. As such, fuel mixtures were created to be monitored over a length of time in order to observe any separation. The first test entailed observation of the blends in sealed graduated cylinders. 25 ml of each blend were left to sit undisturbed for one week, with photographs taken every day. No separation was observed in this time period, making these fuels stable in closed storage environments.
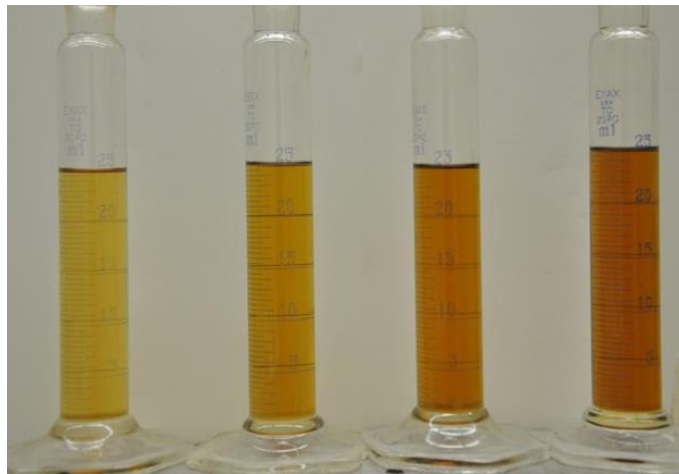
Figure 45: From Left to Right, BE20, BE40, BE60, BE80 Fuels in Sealed Containers

91

A secondary experiment was performed to determine B99-ethanol mixture stability when left in an open room environment at 20° C. In this test, photographs captured the weight readout of each solution on a scale, as well as the liquid itself in order to monitor evaporation and separation rates. In this, samples were monitored for 120 hours, with photographs captured in 4 hour increments.
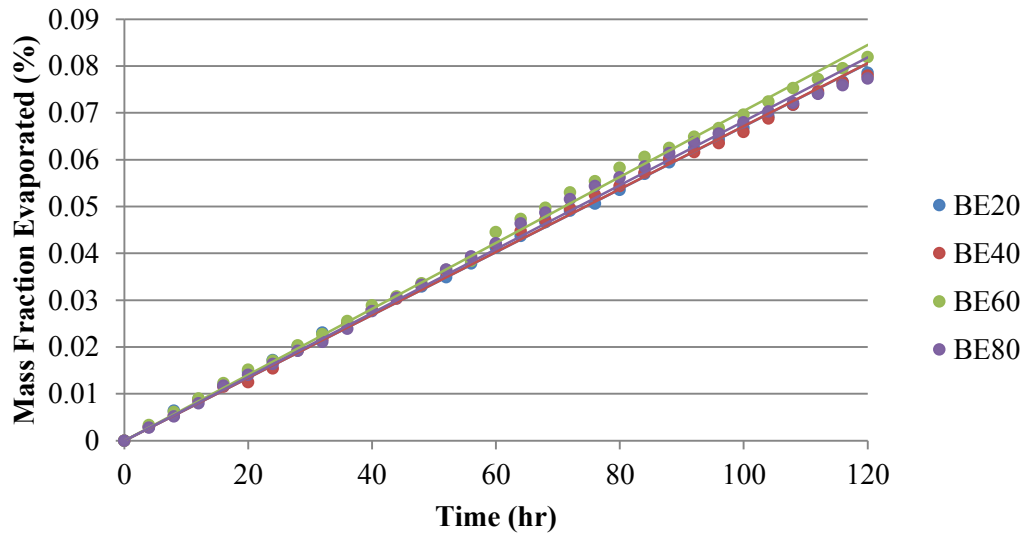
Figure 46: Mass Evaporation Rates for B99-Ethanol Blends

Results displayed in Figure 46 show little evaporation occurring for all blend types. The evaporation rates captured are all in linear fashion with roughly equivalent slopes. The one exception being the BE60 blend was the only fuel with noticeable separation that began to occur near hour 88 of the experiment. However, it was expected to observe exponentially decaying mass reduction rates as the ethanol is expected to evaporate out of the mixture as it generally has a higher vapor pressure than biodiesel varieties. Freitas et al. experimentally determined vapor pressures for 10 biofuels commonly found in Brazil, Europe, and the United States: soybean, sunflower, rapeseed, palm, and a variety of blends. At a temperature of 500K, recorded vapor

pressures were between 3.85 – 5.17 kPa (Freitas et al. 2012). In order to contrast with ethanol, the Antoine equation (5-4) is used to predict vapor pressures for the given temperature:

$$\log_{10}(P) = A - (B/(T+C)) \tag{5-4}$$

The NIST database for ethanol provides values for the constants A, B, and C (NIST 2011). The Antoine equation yields a vapor pressure of 4529.53 kPa, a result three orders of magnitude larger than those of the various biodiesels.

5.4.3. B99-Ethanol Combustion Performance

5.4.3.1. Sooting and Blow off

Analysis on soot precursors indicated by flame luminosity was again conducted for the B99-ethanol blends in the same manner as for the six base fuels. Reduction in emissions of particulate matter from non-premixed combustion, such as in this study, generally receive more attention than for premixed systems (Turns 2012). Reduction in levels of these particulates is of importance for all usages of hydrocarbon fuels. Typically, factors governing soot, or smoke, are combustor inlet temperatures, pressure, and fuel spray characteristics. Optimization of these contributions will lead to better overall fuel-air mixing (Ballal & Lefebvre 2010). Results for the B99/ethanol mixtures are not what is expected by intuition, shown in Figure 47 below. In this figure, again soot levels are approximated according to the total flame luminosity for an averaged image over 1 second imaged at 400 fps.
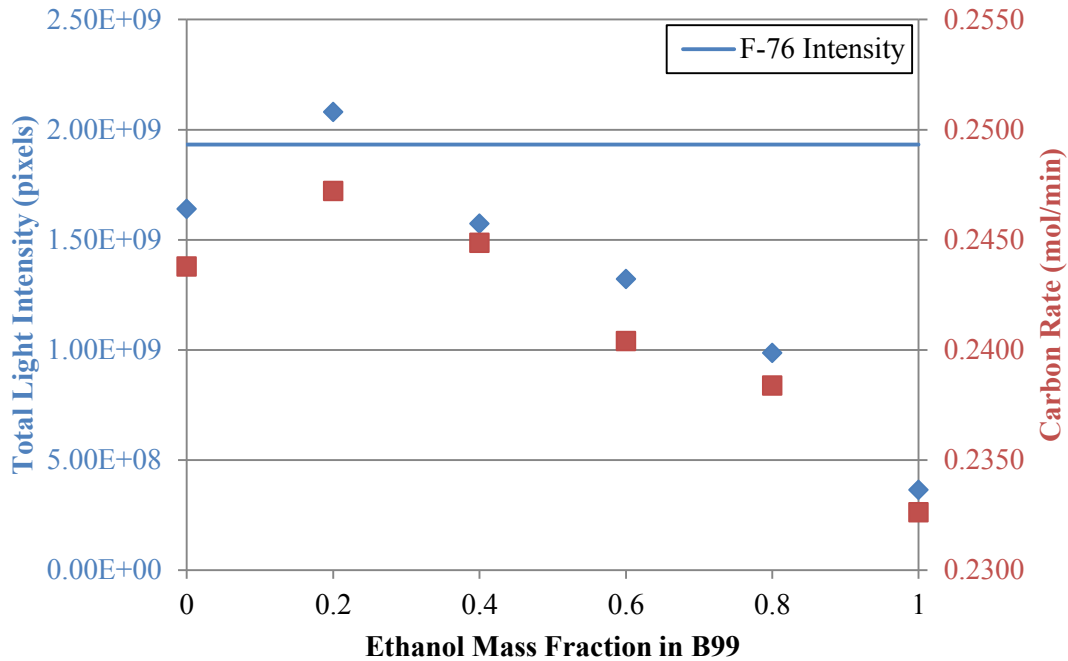
Figure 47: Flame Luminosity vs. Carbon Rate into Combustor

In adding ethanol to B99, each subsequent mixture linearly reduces the carbon to hydrogen ratio while linearly increasing the oxygen mass fraction. This, along with better fluid properties for atomization would lead one to expect smaller drop sizes and increased mixing rates typical for soot reductions. However, Figure 47 shows that this is not the case, and that flame luminosity peaks with the BE80 blend and subsequently provides less luminous flames for the remaining mixtures. While soot is comprised of solid carbon compounds, it appears logical that the levels found here mimic the behavior of the rate at which carbon is injected to the combustion environment. This trend between carbon rate and soot collapses to a linear fit, seen in Figure 48 for B99, ethanol, and their blends but does not form such a clear relationship for methanol and the non-oxygenated fuels.
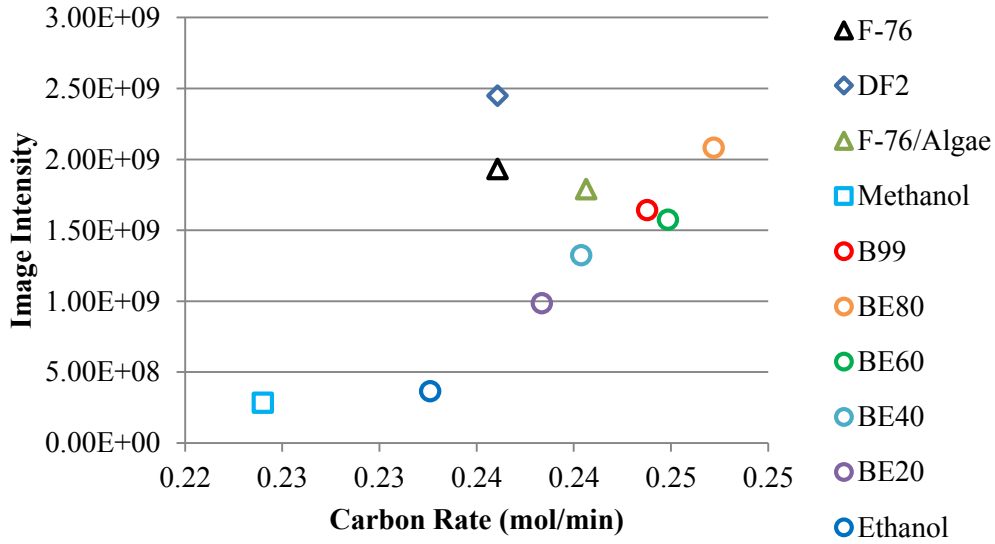
Figure 48: Carbon Feed Rate Plotted Against Average Flame Luminosity

Along with reducing PM levels, it is sought to provide a "drop in" fuel that may provide a wide range of operation for a gas turbine system with similar turn down ratios as compared with conventional fuels.
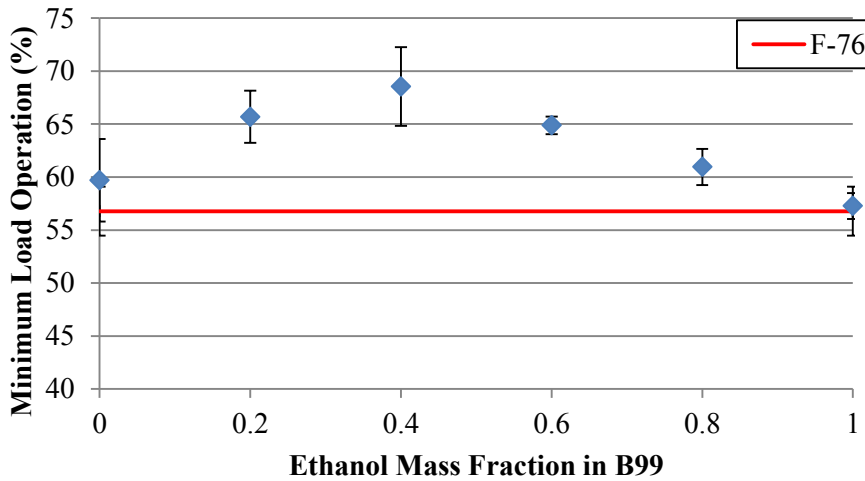
Figure 49: Minimum Load Operation for B99/Ethanol Blends

All blending ratios between B99 and ethanol exhibit decreased performance in regards to load operating range. Neat B99 and ethanol display statistically equivalent load ranges as F-76,

95

while BE80, BE60, and BE40 fuels all have ranges roughly 8% smaller. While mass flow must be increased with ethanol concentration, fuel volatility increases as well. The process of extinction in flames is a function of the equivalence ratio, fuel-air mixture temperature, and the fuel chemistry (Sivasegaram 2008). Unsaturated hydrocarbons such as ethanol experience less susceptibility to extinction than saturated hydrocarbons such as B99 and F-76. However this effect is mitigated by ethanol's relatively large flow rate. Additionally, exhaust temperatures for B99/ethanol blends were lower than for pure B99, thus providing less pre-vaporized fuel entering the combustion environment.

5.4.3.2. NO_x, CO, & UHC Emissions

In this blending strategy, one expects to create fuels that are able to create a balanced emission output between the ethanol and B99 extremes. Figure 50 displays the effect of added ethanol in B99, where NO_x steadily decreases for all ethanol concentrations. In contrast with the design fuel, F-76, all of the blended oxygenated fuels produce less ppm of NO_x. This effect is partially driven by increased oxygen content and lowered C-H ratios, as compared with B99. Furthermore, ethanol addition to B99 increases fuel volatility, enabling the fuel blends to evaporate much faster. Improved evaporation and lower local reaction temperatures yields less NO_x produced via the thermal pathway. In regards to the other 3 available NO_x formation pathways, the fuel bound NO route can be neglected as B99 and ethanol contain no nitrogen. Of the remaining two, the Fenimore pathway is likely more prevalent than the N_2O intermediate mechanism due to the ultra-lean operating conditions with $\Phi < 0.5$. However, this study does not mean to address the specific modes of NO_x formation, hence these conclusions are simply of speculation.
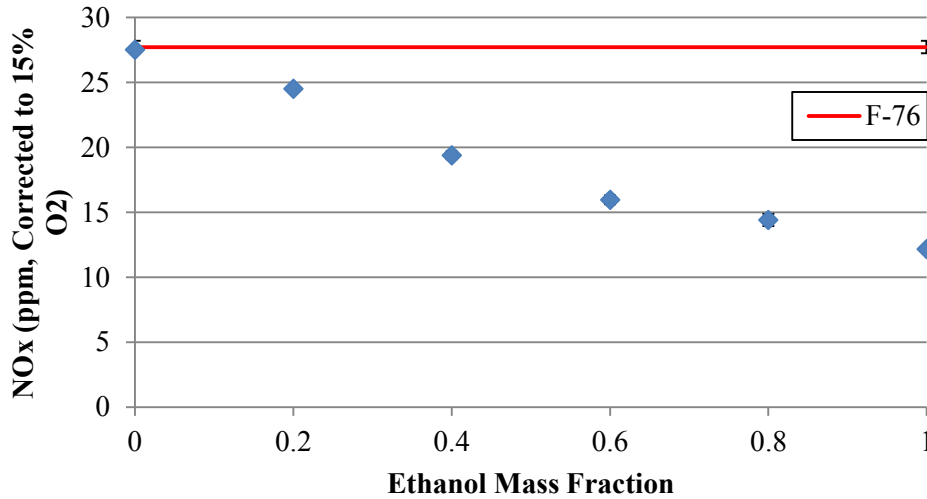
Figure 50: NO$_x$ Emissions for B99-Ethanol Blends

These NO$_x$ results are also strongly tied to combustion temperatures found in the main reaction zone. Reported temperatures for each respective exhaust stream were monotonically lower with increasing ethanol blending ratios. This temperature decrease is again related to the combustion efficiency which, depicted in Figure 51, is tied to the amount of unburned carbon monoxide and hydrocarbons.
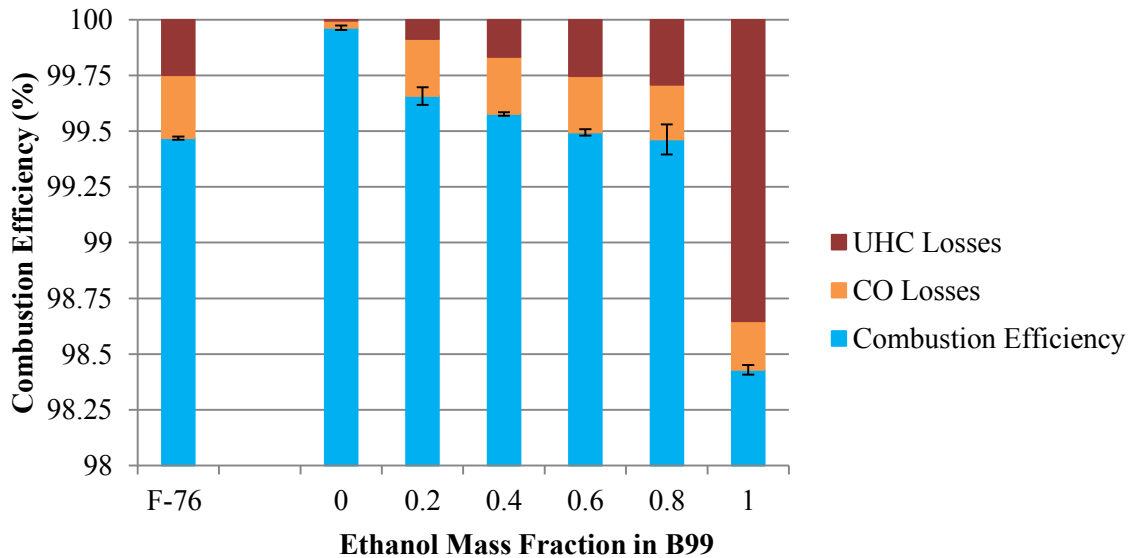
Figure 51: Combustion Efficiencies for B99-Ethanol Blends

The above figures definitively show that B99 dramatically outperforms ethanol and all four of the blends in terms of most complete combustion, while all of the blends perform equally or superior to F-76. Ethanol addition to B99 requires higher mass flow rates in order to meet the power demand, resulting in lower ALR. However, increased fuel flow rates coupled with increased oxygen content result in nearly identical global equivalence ratios for these six fuels ranging from 0.476 – 0.468, with B99 operating at the most lean Φ. It appears that in increasing the mass flow rates for each subsequent blend, less fuel is able to be consumed at the allotted equivalence ratio due to low temperatures inhibiting reaction kinetics. This finding is contrary to expected results for yielding more complete combustion for higher oxygenated fuels. Here, CO levels are similar for each fuel blend, however unburnt hydrocarbon levels, nearing 0 ppm for B99, consistently rise with increasing ethanol. Non-premixed flames add great complexity to the problem of pollutant formations as combustion occurs in both premixed modes when fuel is quickly evaporated and mixed with surrounding air, or in the diffusion mode for large droplets not yet gasified. This complexity yields the entire reaction zone to be comprised of non-homogeneous mixing and localized spots of varying equivalence ratio and temperatures. Further insight on the reported emissions is revealed during atomization analysis in the following section. In total, the creation of these fuel blends aims to create a substitute fuel for F-76 with the possibility of superior performance. In terms of emissions, this constitutes striving for a simultaneous reduction in NO_x, CO, and UHC compounds in a trend that deviates from the typical tradeoff previously shown in Figure 31. With the blends' results plotted on the same figure, it is demonstrated that while the modified curve still exhibits a negative slope, all of the B99/ethanol blends are shifted closer to the origin.
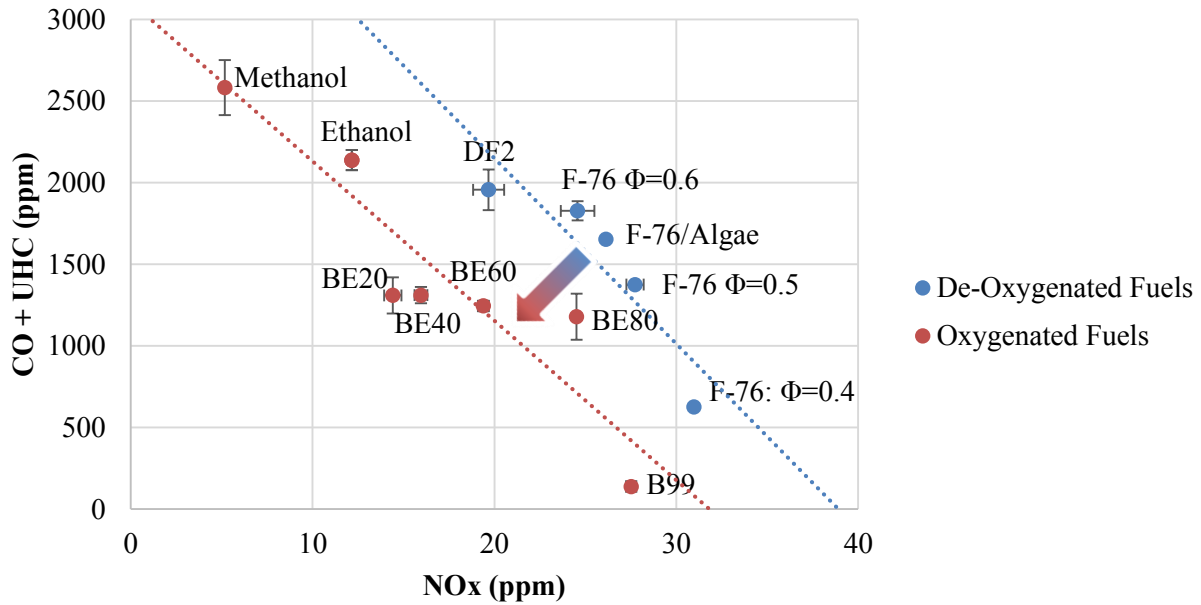
Figure 52: NO$_x$ vs. CO & UHC for All Fuels

5.4.4. Hybrid Fuel Atomization

Results on combustion performance and emissions cannot be fully explained without detailed information on the cold flow sprays. With this burner operating on diffusion flames, droplet sizes and distributions play key roles on emission outputs. The first of such cold flow aspects addressed is with regards to the Sauter mean diameters downstream of the nozzle. In the same fashion as earlier, SMD values were captured across a 10 mm width of the spray plume. As determined by previous results, atomization performance is optimal at the highest of the three chosen pressure drops, thus the B99/ethanol blends were only tested at 40.6 kPa. Previous results for F-76 are plotted again to provide comparison against the base operation.
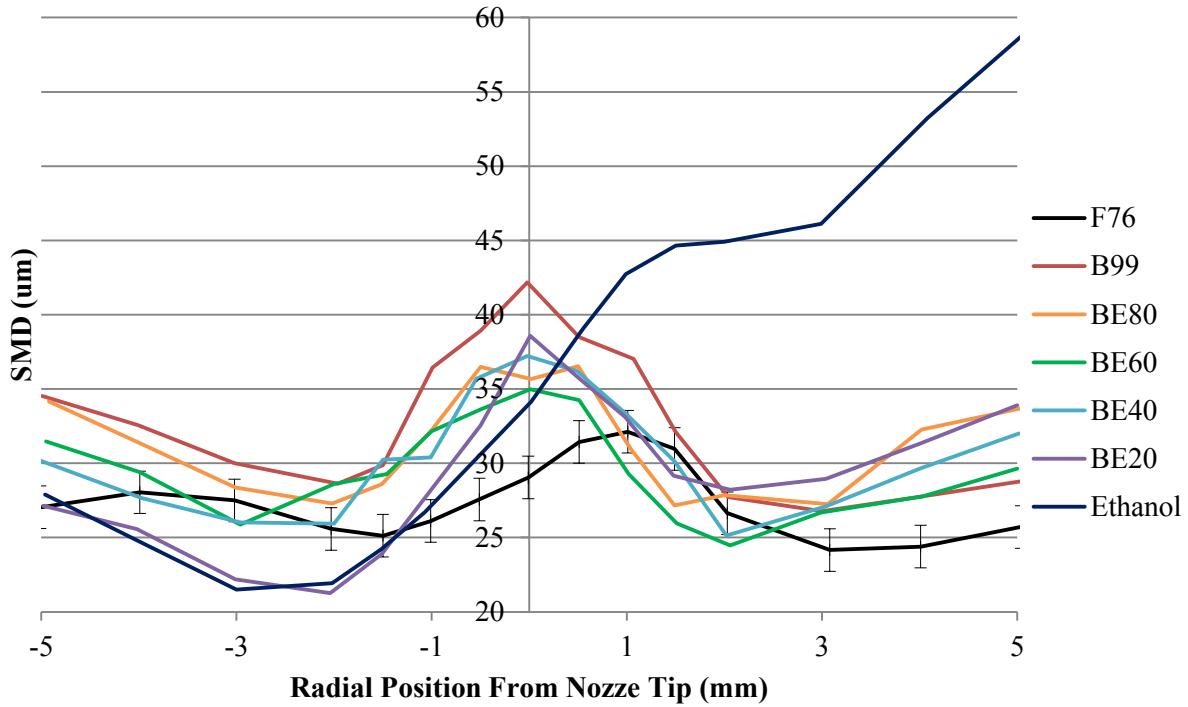
Figure 53: SMD Profiles for B99/Ethanol Blends for Air-blast Atomizer

With the B99/Ethanol blends in Figure 53, one notes the level of symmetry for the BE80, BE60, and BE40 blends. Symmetry of spray patterns produced in atomization is of considerable importance as the fuel must be distributed uniformly as possible throughout the combustion zone to achieve high combustion efficiency, low pollutant formation, and uniform temperature distribution (Ballal & Lefebvre 2010). These blends, along with B99, atomize to produce the largest droplets along the centerline of the spray whereas the F-76 deviates 1 mm to the right. This serves as one possible explanation for their increased combustion efficiency. The BE20 blend, with 80% ethanol, begins the asymmetry trend towards ethanol as smaller droplets are biased towards the left hand side of the traverse. Perhaps with more fuel samples at higher ethanol concentrations near 90% one would observe this effect increasing as more fluid builds up at the orifice exit as seen with pure ethanol. Additionally, it is seen that the fuel blends

100

www.manaraa.com

experience an overall decrease in droplet size as ethanol is added to B99. Given the appropriate error bars, blends BE80, BE60, and BE40 appear to be close in size. Using equation 5-3, weighted SMD values for each fuel are plotted against values calculated using Lefebvre's equation 5-2 for an air-blast atomizer with the previous modifying coefficient $\varepsilon = 1.25$.
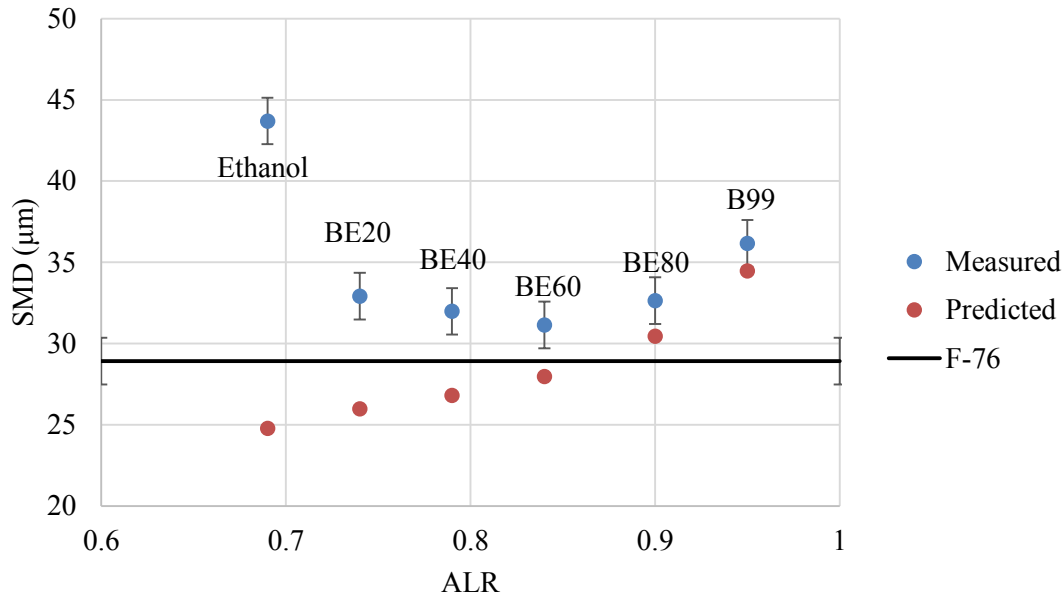
Figure 54: Measured and Calculated SMD Values Plotted Against ALR

First inspection of Figure 54 displays the improved atomization in contrast with both the B99 and ethanol pure fuels. Blends at all ethanol concentrations yield statistically identical drop sizes. These blends are able to be atomized more efficiently due to their decreased viscosity and surface tension, even while operating at lower air to liquid ratios. However the decreasing drop size trend does not continue across all blending ratios. Thus with increasing mass flows less fuel is oxidized sufficiently, leading to increased numbers of UHC compounds and consequently steadily decreasing combustion efficiencies (see Figure 51).

Using the prescribed equation for an air-blast atomizer used by Lefebvre, it is seen that the prediction does not follow well for all the fuels. Drawing upon previous results for methanol, it is seen that this empirical correlation does not hold for sufficiently low ALR below 0.9. The phenomena of liquid buildup at the nozzle exit seen with ethanol and methanol does not appear as blatantly as with methanol and ethanol, but precursors for it are seen through high speed footage. High speed footage indicates the fuels blends all emerging from the nozzle having undergone the prompt atomization mode, however at increasing ethanol saturations sprays ejected from the nozzle begin to sputter more, producing a less continuous spray. In the high speed still displayed in Figure 55, one is faintly able to see clusters of fuel held as the nozzle exit.
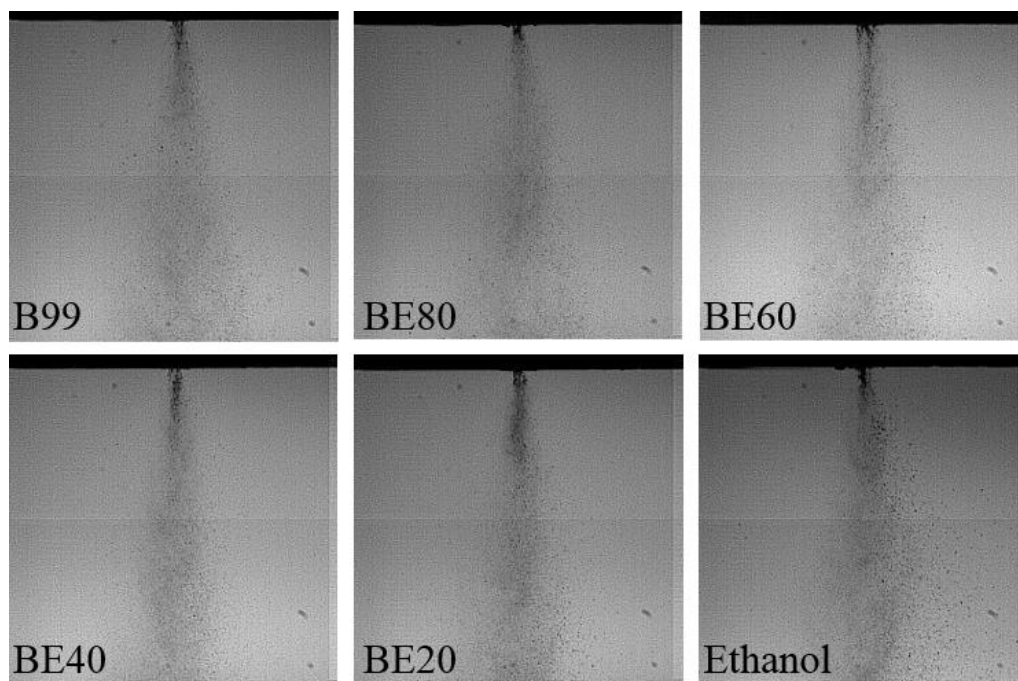
Figure 55: High Speed Stills of the B99-Ethanol fuels for the Air-blast Atomizer

Volume flux data provides additional support to the spray patterning across the spray plume. Here the sprays are show to be symmetric, excluding the case with pure ethanol. Slight

deviations to the right half of the plane for BE40 and BE20 contribute additionally to their

decreases in combustion efficiency.
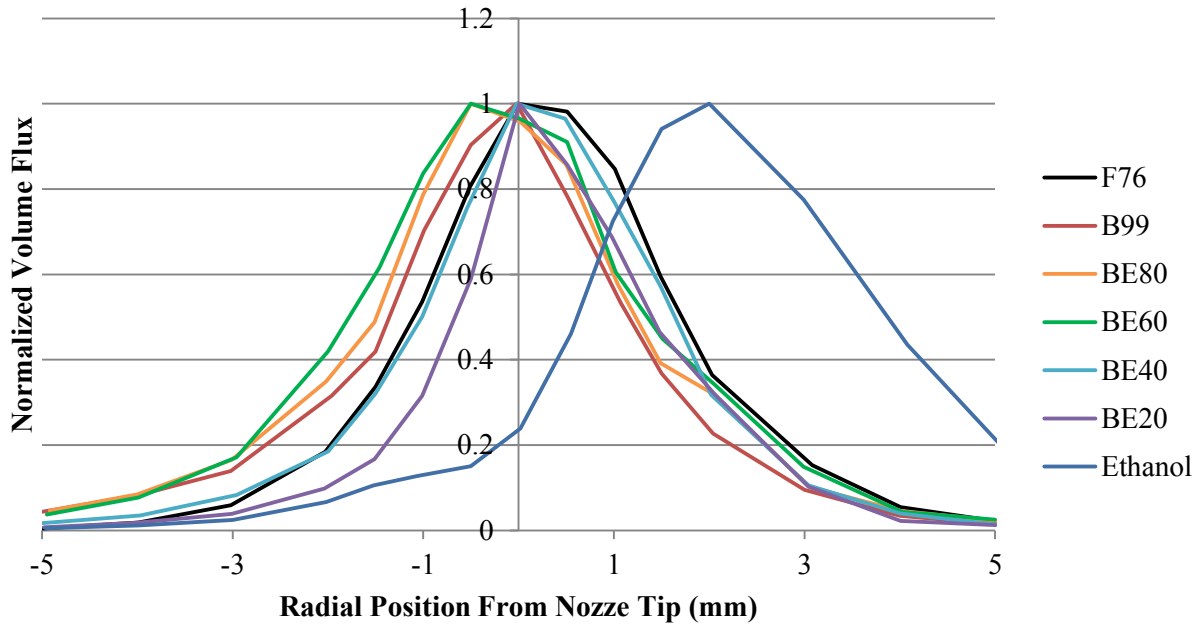
Figure 56: Normalized Volume Flux Data for B99-Ethanol Fuels

6. Summary, Conclusions, & Recommendations

6.1 Summary

This study examined the combustion performance of a variety of alternative fuels in a low velocity experimental burner utilizing a plain air-blast atomizer. A range of renewable fuels were studied including those derived from edible and non-edible feedstocks (B99 and ethanol), advanced algae cultivation (Hydrotreated Renewable Diesel), as well as from CO_2 capture and syngas conversion methods (methanol). Combustion performance of each fuel was analyzed for steady state combustion simulating a "drop in" gas turbine scenario with fuel type being the single variable. Gaseous emissions readings, lean stability limits, as well as flame imaging techniques to characterize soot formation were studied for each fuel and compared with the baseline F-76 naval distillate. In order to gain deeper insight to reacting flow results, the cold-flow atomization performance was investigated using phase Doppler interferometry and high speed shadowgraphy methods. These measurements provided detailed information of droplet size, velocity, and volume flux distributions across a section of the spray plume. Initial results for pure renewables shed light on the advantages and shortcomings associated with each. The Algae HRD is physically and chemically similar to F-76, enabling matched performance with similar emission making it a likely candidate as a "drop in" fuel for exiting gas turbines. In substituting B99 for F-76, only slight mass flow rate increases are required. However, less than optimal atomization and high hydrocarbon ratios lead to increased levels of NO_x. On the contrary, dramatic flow rates for ethanol and methanol yield poor combustion efficiency coupled with lowered NO_x production. These findings lead to the creation and similar testing of four B99-ethanol hybrid fuels in order to explore the effects on fuel chemistry and physical properties

in order to create a fuel with balanced emissions and operability. It was found that each fuel optimizes certain performance characteristics, and that few trends scoping the range of fuels from B99 to pure ethanol behaved in a linear fashion. These results hope to provide precursors to the combustion performance of renewable fuels in a real gas turbine.

6.2 Conclusions

In compiling and observing the results of this study, the following key observations were made:

- The F-76/Algae blend requires no system modifications and could serve as a "drop in" fuel with nearly identical performance to the baseline F-76 fuel.

    This is to be expected base on the physical properties of the F-76/Algae fuel which closely match that of the conventional fuels F-76 and DF2. Complemented with a similar air to liquid ratio, the F/76/Algae atomized to produce a nearly identical sizing and spatial SMD distribution and to the baseline fuels. It was observed that the F-76/Algae blend did reduce NO_x and sooting propensity compared to the base fuels, however this was also accompanied by slightly lower combustion efficiency based on measured CO and hydrocarbon levels.

- In this experimental burner, the B99 yields the highest combustion efficiency (lowest levels of CO and UHC compounds) and exhaust temperatures.

    Concomitantly, B99 also produces the highest NO_x levels thus exhibiting typical combustion performance tradeoffs between NO_x and CO. Examination of the

www.manaraa.com

atomization performance indicates large droplets are produced with B99 which is consistent with the observed NO_x behavior. However, the presence of the larger droplets would also tend to give rise to higher levels of incomplete combustion products – yet this is not observed. Apparently the high local temperatures responsible for high NOx is also leading to more complete combustion in the present system through enhanced evaporation or higher reaction rates.

- <u>Ethanol and methanol both effectively reduce NO_x emissions at the expense of substantially larger flow rates and high levels of CO and UHCs.</u>

    For these fuels, atomization results reflect the relatively low ALR for the air-blast atomizer due to the higher liquid flows with constant air flow. This also results in asymmetric spray spatial distributions for both the volume flux and Sauter mean diameters. The breakup of these fuels is inhibited by a secondary mode of atomization wherein accumulations of fuel are periodically shed from the nozzle exit; contrary to the other fuels that undergo the intended prompt atomization prior to entering the combustion environment. Less than ideal atomization, inhibiting combustion efficiencies and peak temperatures, combined with fuel bound oxygen for improved local mixing served to reduce NO_x emissions.

- <u>The rate of carbon addition to the reaction zone strongly correlates to flame luminosity for B99, ethanol, and their blends. This relationship does not hold as strong for the other fuels F-76, DF2, F-76/Algae, & Methanol.</u>

Conventional fuels F-76 and DF2 produce flames with the highest levels of soot. The F-76/Algae blend generates less soot particulate which is attributed to lack of aromatic compounds in the algae portion. All three of the oxygenated fuels yield flames with greater blue hues than yellow, and overall lowest average luminosity in, decreasing in order respectively, B99, ethanol, and methanol. Sooting propensity peaks and exceeds that of F-76 for the BE80 fuel, while the other three blends show decreased PM production. The amount of carbon introduced to the combustion environment linearly predicts soot levels for B99, ethanol, and their blends.

- <u>Lean flame extinction limits varied depending largely on exhaust temperatures and fuel composition, with methanol displaying the widest range of operation.</u>

  DF2, F-76, B99, and ethanol have statistically identical lean extinction limits in terms of power turn down capacity. The F-76/Algae blend results in greater combustion stability than the conventional fuels. Results for ethanol are somewhat unexpected as methanol, another alcohol, has the widest range of operation limits. However, with ethanol having the lowest combustion efficiency of any fuel, lower combustion temperatures are achieved which inhibit droplet gasification.

- <u>In terms of viability of storage of a B99-ethanol blend, time lapse analysis indicates that B99-ethanol blends are miscible and stable in a closed volume, but are subject to phase separation and evaporation when exposed to the ambient environment.</u>

  Ambient evaporation rates for the hybrid fuels are independent of ethanol mass fraction and are governed by surface area open to the environment. In practical systems,

pre-mixed B99-ethanol blends must be stored in closed containers to conserve fuel mixture ratios and control evaporation.

- The blending of B99 and ethanol resulted in consistent reductions in NO_x as compared with B99 and F-76.

    Ethanol addition resulted in similar CO levels and increased UHCs giving rise to decreased combustion efficiencies. Even so, efficiencies for the fuel blends all exceed or closely match that for F-76. Emissions results for the hybrid fuels display effective reductions in CO, UHC, and NO_x as compared with all non-oxygenated fuels.

- Even with lower ALR, all B99-ethanol blends display improvements in atomization as compared with B99.

    With a significant decrease in SMD from B99 to BE80, droplet size reductions are not as ample for the remaining blends as increased liquid flow rates counteract the effects of decreased viscosity and surface tension. Within experimental uncertainty, the BE60 blend produces droplet sizes matching closest with that of the F-76. In regards to spray symmetry, increasing ethanol content gradually skews spray distributions beginning with BE40 however this effect does not manifest itself in reacting conditions.

- Lefebvre's empirical SMD correlations for the air-blast atomizer do not accurately predict droplet sizes for the B99-ethanol blends.

Lefebvre's correlation for the air-blast atomizer does not hold for methanol and ethanol where a secondary mode of atomization takes place following prompt atomization in the nozzle. Additionally, increasing ethanol mass fraction in the fuel blends produces larger deviations from the predicted SMD values. Even while undergoing normal atomization modes from the nozzle and using the measured physical properties, the SMD correlation does not hold for these fuels, thus a new correlation is required.

- Table 13 presented below displays each fuel's relative performance in various aspects in comparison with the baseline F-76.

Table 13: Performance Summary For All Fuels Compared With F-76

Worsened	Comparable	Improved
(red)	(yellow)	(green)

	NO$_x$	CO	UHC	η_c	Soot	Blowoff	SMD	Spray Symmetry
F-76	-	-	-	-	-	-	-	-
DF2	Improved	Worsened	Comparable	Worsened	Worsened	Comparable	Comparable	Comparable
F-76/Algae	Improved	Worsened	Worsened	Comparable	Improved	Improved	Comparable	Comparable
Methanol	Improved	Worsened	Worsened	Worsened	Improved	Improved	Worsened	Worsened
B99	Comparable	Improved	Improved	Improved	Improved	Comparable	Worsened	Comparable
BE80	Improved	Improved	Improved	Improved	Worsened	Worsened	Worsened	Comparable
BE60	Improved	Improved	Comparable	Improved	Improved	Worsened	Comparable	Comparable
BE40	Improved	Improved	Worsened	Comparable	Improved	Worsened	Worsened	Comparable
BE20	Improved	Improved	Worsened	Worsened	Improved	Worsened	Worsened	Worsened
Ethanol	Improved	Improved	Worsened	Worsened	Improved	Comparable	Worsened	Worsened

6.3 Recommendations

As this thesis accomplished the stated goal, more work can be done to provide a wider range of performance predictability for the alternative fuels of interest. For this reason, the following recommendations are made:

- Create an extensive distillation curve to characterize the evaporation and volatility behavior of the B99-ethanol blends.

- Develop an advanced atomization model that predicts behavior for the non-conventional hybrid fuels.

- Study effectiveness of in line mixing for B99 and ethanol in order to provide simplifications to storage and refueling processes.

- Conduct a more broad study in emissions by considering various equivalence ratios, namely the effect of wall cooling air, and the effect of nozzle pressure drop as it relates to both droplet sizes and their velocities.

- Employ the renewable fuels in an existing gas turbine system to study the effects of elevated pressure, and pre-heated air/fuel on overall emissions. In this process, extract the control strategies for moderating fuel flows.

- Explore the extent to which the conclusions here apply to other types of fuel injectors such as pressure atomizers. This would have implications for a broader array of combustion systems.

References

Agarwal, A.K. "Biofuels (alcohols and biodiesel) applications as fuels for internal combustion engines." Prog Energy Combust Sci, 33 (2007), pp. 233–271

Agency for Toxic Substances and Disease Registry (ATSDR). 1995, "Toxicological Profile for Fuel Oils." Atlanta, GA: U.S. Department of Health and Human Services, Public Health Service

Agency, I. E. (2014). "Fossil Fuel Energy Consumption."

Ahmad, A. Y., N. Mat, H. Derek, C. J. C. Lim, J. K. (2011). "Microalgae as a sustainable energy source for biodiesel production: A review." Renewable and Sustainable Energy Reviews **15**(1): 584-593.

Alfaro-Ayala, J. A., A. Gallegos-Munoz, et al. (2013) "Use of bioethanol in a gas turbine combustor." Applied Thermal Engineering **61**(2): 481-490.

Arifin, Y. M. and M. Arai (2010). "The effect of hot surface temperature on diesel fuel deposit formation." Fuel **89**(5): 934-942.

ASTM, 2009a. D1655-09, "Standard Specification for Aviation Turbine Fuels." ASTM International: West Conshohocken, Pennsylvania.

ASTM, 2009b. D7566-09, "Standard Specification for Aviation Turbine Fuel Containing Synthesized Hydrocarbons." ASTM International: West Conshohocken, Pennsylvania.

Ballal, D. R., Lefebvre, A. H. (2010). "Gas Turbine Combustion: Alternative Fuels and Emissions." Florida, Taylor and Francis Group.

Balat, M. and H. Balat (2010). "Progress in biodiesel processing." Applied Energy **87**(6): 1815-1835.

Becker, W. (1994). "Microalgae: Biotechnology and Microbiology", Cambridge University Press.

Belot GT, "An Evaluation and Economic Study of Alternative Jet Fuel from Jatropha Curcas Oil." (Thesis) The Pennsylvania State University 2009.

Berkooz, G., P. Holmes, et al. (1993). "The Proper Orthogonal Decomposition in the Analysis of Turbulent Flows." Annual Reviews: Fluid Mechanics **25**: 539-575.

Bolszo, C., V. McDonell, et al. (2007). "Impact of Biodiesel on Fuel Preparation and Emissions for a Liquid Fired Gas Turbine Engine." ASME Conference Proceedings 2007(47918): 493-502.

Bolszo, C. D. (2008). "Operation and Optimization of a Biodiesel Fired Gas Turbine." <u>MAE</u>. Irvine, University of California, Irvine. **M.S.:** 116.

Bolszo, C. D. and V. G. McDonell (2009). "Emissions optimization of a biodiesel fired gas turbine." <u>Proceedings of the Combustion Institute</u> **32**(2): 2949-2956.

Board, C. A. R. (2010). "RULE 1134 Stationary Gas Turbines." 10.

Brennan L, Owende P. "Biofuels from microalgae--A review of technologies for production, processing, and extractions of biofuels and co-products." Renewable and Sustainable Energy Reviews. 2010; 14:557-577.

Bryden., K. W. R. K. M. (2011). "Combustion Engineering." NW, Taylor & Francis Group.

Butnark, S, Rudnick LR, Schobert HH. "Thermally stable coal-based jet fuel: Chemical composition, thermal stability, physical properties and their relationships." ACS, Div Pet Chem, Preprints, 2004; 49:145-146.

California Air Resources Board (CARB), (2004) "Health Effects of Particulate Matter and Ozone Air Pollution." USA.

M. Canakci, C. Sayin, M. Gumus. "Exhaust emissions and combustion characteristics of a direct injection (DI) diesel engine fueled with methanol–diesel fuel blends at different injection timings." Energy Fuel, 22 (2008), pp. 3709–3723

Chiaramonti, D., A. M. Rizzo, et al. (2013) "Exhaust emissions from liquid fuel micro gas turbine fed with diesel oil, biodiesel and vegetable oil." <u>Applied Energy</u> **101**(0): 349-356.

Christensen, E. and R. L. McCormick (2014). "Long-term storage stability of biodiesel and biodiesel blends." <u>Fuel Processing Technology</u> **128**(0): 339-348.

De Nevers, N, (2000) "Air Pollution Control Engineering." 2nd Ed. McGraw Hill Publishing. Pp. 443, 537.

"Diesel Fuel." Environmental Protection Agency. Oct. 2012.

Dragone, G. F., B. Antonio, V. Taixeira, J. (2010). "Third Generation Biofuels From Microalgae." <u>Institute for Biotechnology and Bioengineering</u>. Braga, University of Minho.

EIA (Energy Information Administration), 2014a. "International Energy Statistics – Petroleum & other liquids – Annual Consumption Web page with data through 2012."

Environmental Protection Agency (EPA), (2012) "Diesel Fuel." USA.

Environmental Protection Agency (EPA), (2012) "Six Common Air Pollutants." USA.

Freitas, S., M. Oliveira, et al. (2012). "Measurement and Prediction of Biodiesel Volatility." <u>Energy and Fuels</u> **26**: 3048-3053.

GE (2001). "Feasiblity of Methanol as Gas Turbine Fuel." <u>GE Position Paper</u>.

GE Energy. (2010). "Ethanol Fires Gas Turbine to Produce Power, AG Annex." http://www.agannex.com/biofuels/ethanol-fires-gas-turbine-to-produce-power

Goodger, E. M., "Combustion Calculations, Theory, Worked Examples, and Problems." MacMillan Press, London, 1977.

Gupta, K. K., A. Rehman, et al. "Bio-fuels for the gas turbine: A review." <u>Renewable and Sustainable Energy Reviews</u> 14(9): 2946-2955.

Haggstrom, C., U. Rova, et al. (2014) "Chapter 8 - Integration of Ethanol Fermentation with Second Generation Biofuels Technologies." <u>Biorefineries</u>. Amsterdam, Elsevier**:** 161-187.

Hain, Y. Chudnovsky, B. Rappoport, N. Reshef, M. Baitel, S. (2012). "Methanol as a low cost alternative fuel for emission reduction in gas turbines."

Hileman, J. I. and R. W. Stratton "Alternative jet fuel feasibility." 2014. <u>Transport Policy</u> 34(0): 52-62.

Huang, Z. H.B. Lu, D.M. Jiang, K. Zeng, B. Liu, J.Q. Zhang, X.B. Wang. "Engine performance and emissions of a compression ignition engine operating on the diesel/methanol blends.**"** Proc. Instn Mech. Engrs, Part D: J. Automobile Engineering, 218 (2004), pp. 435–447

Kallenberg, A. (2013). "Liquid Bio Fuels for Gas Turbines." <u>Energy Sciences</u>. Lund, Lund University. Engineering Physics: 90.

Kumar, N., Varun, et al. (2013) "Performance and emission characteristics of biodiesel from different origins: A review." <u>Renewable and Sustainable Energy Reviews</u> **21**(0): 633-658.

Khalil, A. E. E. and A. K. Gupta "Fuel flexible distributed combustion for efficient and clean gas turbine engines." <u>Applied Energy</u> 109(0): 267-274.

Kim, H. J., H. K. Suh, et al. (2008). "An Experimental and Numerical Investigation of Atomization Characteristics of Biodiesel, Dimethyl Ether, and Biodiesel Ethanol Blended Fuel." <u>Energy & Fuels</u> 22(3): 2091-2098.

M. Lapuerta, O. Armas, J. Rodríguez-Fernández. "Effect of biodiesel fuels on diesel engine emissions." Prog Energ Combust Sci, 34 (2008), pp. 198–223

Lavoie J.-M., Beauchet R., Berberi V., Chornet M.. 2011. "Biorefining lignocellulosic biomass via the feedstock impregnation rapid and sequential steem treatment." In: *Biofuel's Engineering Process Technology*. Bernardes M., ed. Intech publishing, Croatia. p. 685–714

Law, K. Rosenfeld, J., Jackson, M. (2013). Methanol as a Renewable Energy Resource**:** 18.

Lee, R. H. Louvie, J. (2013). "From First to Third Generation Biofuels: Challenges of Producing a Commodity from a Biomass of Increasing Complexity." Animal Froniters.

Lefebvre, A. H. (1989). "Atomization and Sprays." Indiana, Hemisphere Publishing Corporation.

Lefebvre, A. L., G. (1977). "Measurements od Drop Size on a Plain-Jet Aiblast Atomizer." AIAA **15**(7): 5.

Legg, J. A. A. N., and McDonell, V. (2011). "Performance of Alternative Liquid Fuels in a Swirl-Stabilized Research Combustor."

Legg, J. (2012). "Experimental Investigation of Physical Combustion Characteristics for Alternative Liquid Fuels." MAE. Irvine, University of California, Irvine. M.S.: 127.

Li, H. Altaher, M. Andrews, G. (2010). "Evaluation of Combustion and Emissions Using Biodiesel and Blends with Kerosene in a Low NO_x Gas Turbine Combustor." ASME Turbo Expo

Lieuwen, T. Y., V (2013). "Gas Turbine Emissions." New York, Cambridge University Press.

V. Lupandin, A. Nikolayev and R. Thamburaj (2005). "Test Results of the OGT2500 Gas Turbine Engine Running on alternative Fuels: Biooil, Ethanol, Biodiesel and Crude Oil," Paper GT2005-68488, ASME Turbo Expo, Reno-Tahoe, Nevada, USA, June.

Mattingly, J. D., W. H. Heiser, et al. (2002). "Aircraft Engine Design."

Nascimento, M. A. R., E. S. Lora, et al. (2008). "Biodiesel fuel in diesel micro-turbine engines: Modelling and experimental evaluation." Energy **33**(2): 233-240.

Nasr, Yule and Bending, "Industrial Sprays and Atomization", Springer, 2002.

Nigam, P. S., Singh, A (2011). "Production of liquid biofuels from renewable resources." Progress in Energy and Combustion Science 37(1): 52-68.

NIST (2011). "Chemistry WebBook." U.S. Secretary of Commerce.

Odger, J. Kretschmer, D (1986). "Gas Turbine Fuels and their Influences on Combustion." Abacis Press, Cambridge Massachusetts, USA.

OTAQ (2012). "Fuels and Fuel Additives: Diesel Fuels." Environmental Protection Agency.

Park, S. H., H. K. Suh, et al. (2009) "Nozzle flow and atomization characteristics of ethanol blended biodiesel fuel." Renewable Energy **35**(1): 144-150.

S Pinzi, IL Garcia, FJL Gimenez, MDL Castro, G Dorado, MP. Dorado. "The ideal vegetable oil-based biodiesel composition: a review of social, economical and technical implications." Energy & Fuels (2009), pp. 232325–232341.

Pucher, G., W. Allan, et al. (2011). "Emissions From a Gas Turbine Sector Rig Operated With Synthetic Aviation and Biodiesel Fuel." Journal of Engineering for Gas Turbines and Power **133**(11): 111502-8.

Rashid, N., M. S. Ur Rehman, et al. (2014) "Current status, issues and developments in microalgae derived biodiesel production." Renewable and Sustainable Energy Reviews **40**(0): 760-778.

Rehman, A., D. R. Phalke, et al. (2013) "Alternative fuel for gas turbine: Esterified jatropha oil diesel blend." Renewable Energy **36**(10): 2635-2640.

Y. Ren, Z.H. Huang, D.M. Jiang, W. Li, B. Liu, Wang Xibin. "Effects of the addition of ethanol and cetane number improver on the combustion and emission characteristics of a compression ignition engine." Proc. Instn Mech. Engrs, Part D: J. Automobile Engineering, 222 (2008), pp. 1077–1088

Services, N. H. D. o. E. (2007). "Carbon Monoxide: Health Information Summary." Environmental Fact Sheet.

Sivasegaram, S. (2008). "Lean Combustion: Technology and Control - Chp. 7." Elsevier Inc.

Sung, M. (2014). "Influence of Steam Injection and Water-in-Oil Emulsions on Diesel Fuel Combustion Performance." Mechanical and Aerospace Engineering. Irvine, University of California, Irvine. **M.S.:** 112.

TSI Inc. (2011). "Phase Doppler Particle Analyzer (PDPA)/Laser Doppler Velocimetry (LDV) Operations Manual." Revision G, Shoreview, MN.

Turns, S. R. (2012). "An Introduction to Combustion: Concept and Applications." New York, McGraw Hill.

U.S. DOE (2006). "Gas Turbine Handbook." Editor, Richard Dennir, http:/netl.doe.gov/technologies/coalpower/turbines/refself/handbook.

U.S. DOE (2014). "Biomass Energy Data Book: Ethanol Overview." http://cta.ornl.gov/bedb/biofuels/ethanol/Ethanol_Overview.shtml

U.S. DOE (2015). "Alternative Fuels Data Center." http://www.afdc.energy.gov/vehicles/diesels_emissions.html

U. S. Energy Information Administration. (2012). "Crude Oil Distillation and the Definition of Refining Capacity." Today in Energy, U.S. Department of Energy.

Wang B, Li Y, Wu N, Lan C. "CO2 bio-mitigation using microalgae." Applied Microbiology and Biotechnology. 2008; 79:707-718.

Appendix A: Measurement Volume Calculations

For all measurement volume calculations, the following diagram will be referred to.
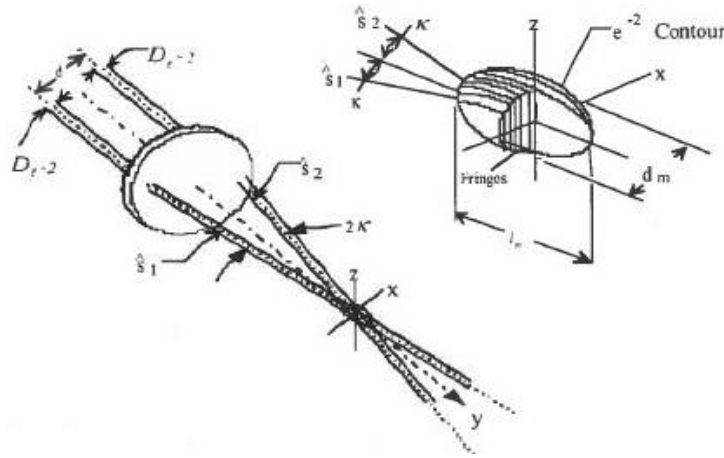
Figure 57: Measurement Volume Dimensions (TSI Inc. 2011)

The first step of calculations required the beam half angle κ. After inputting the transmitter lens focal length into the PDPA/LDV software, the fringe spacing (d_f) is automatically calculated and displayed for both channel 1 and channel 2.

$$d_{f, Ch.1} = 12.8651 \ \mu m \qquad d_{f, Ch.2} = 12.2024 \ \mu m$$

All calculations in Appendix A are provided by TSI Inc. and are shown for only channel 1, the same procedure was used for channel 2 calculations. The fringe spacing is calculated using the following formula.

$$d_f = \frac{\lambda}{2 \sin(\kappa)} \tag{A-1}$$

116

$$\kappa = \sin^{-1}\left(\frac{\lambda}{2d_f}\right) = \sin^{-1}\left(\frac{0.5145 \ \mu m}{(2)12.8651 \ \mu m}\right) = 1.145^o$$

Next, the beam waist ($d_{e^{-2}}$) that corresponds to the diameter on which the light intensity is $1/e^2$ of the maximum intensity. This is a function of the lens focal length, beam wavelength, and initial beam diameter ($D_{e^{-2}}$).

$$d_{e^{-2}} = \frac{4f\lambda}{\pi D_{e^{-2}}} \tag{A-2}$$

$$d_{e^{-2}} = \frac{4(500mm)(514.5x10^{-6} \ mm)}{\pi(1.77 \ mm)} = 0.185 \ \text{mm}$$

The measurement volume diameter (D_m) and length (L_m) is just a geometric function of the beam waist.

$$D_m = \frac{d_{e^{-2}}}{\cos(\kappa)} \tag{A-3}$$

$$D_m = \frac{0.185 \ mm}{\cos(1.145^o)} = 0.185 \ mm$$

$$L_m = \frac{d_{e^{-2}}}{\sin(\kappa)} \tag{A-4}$$

$$L_m = \frac{0.185 \ mm}{\sin(1.145^o)} = 9.254 \ mm$$

Equation A-5 is used to calculate the volume of the measurement volume.

$$V_m = \frac{\pi d_{e^{-2}}^3}{6 \ cos^2(\kappa)\sin(\kappa)}$$

117

$$V_m = \frac{\pi(0.185 \; mm)^3}{6 \; cos^2(1.145^o)sin(1.145^o)}$$

Appendix B: Flame Image Averaging

```matlab
close all
clear
clc

% This MatLab code creates a gray-scale
% By: Adam Silver, 9/2014

% Construct a multimedia reader object associated with file 'xylophone.mpg' with
% user tag set to 'myreader1'.
    readerobj = VideoReader('F76_HighDp.avi');
    % Read in all video frames.
    vidFrames = read(readerobj);
     % Get the number of frames.
    nFrames = 400;
    % Define colormap
     map = [(0:255)' (0:255)' (0:255)']/255;

    % Preallocate movie structure.
mov(1:nFrames) = struct('cdata', zeros(256, 256, 'uint8'),'colormap', map);

% Read one frame at a time and converts video into gray scale.
for k = 1 : nFrames
    mov(k).cdata = rgb2gray(read(readerobj, k));
end

% Prepare the new file.
vidObj = VideoWriter('F76_HighDp_gray.avi','Uncompressed AVI');
open(vidObj);
% Write video
writeVideo(vidObj, mov);
% Close video writer object
close(vidObj);

    % Create a MATLAB movie struct from the video frames.
    for k = 1 : nFrames
        mov(k).cdata = vidFrames(:,:,:,k);
        mov(k).colormap = [];
    end
```

118

```matlab
obj = mmreader("F76_HighDp _gray.avi');
info = read(obj);
frame = read(obj, 1);

Sum = im2double(frame);

for fr = 2:nFrames
    thisframe = im2double(read(obj,fr));
    Sum = Sum + thisframe;
end

%Calculates the mean image from the selected frames
Mean = (Sum / nFrames);
mean_new=im2uint16(Mean); %convert back to uint16
cropped= imcrop(mean_new,[70 50 1024 160]); %Crops image to be displayed
figure(1);
imshow(cropped);
colormap (map); %Displays gray-scale colorbar
xlabel('X (Pixels)');
ylabel('Y (Pixels)');
colorbar;

%Summation of each pixel intensity for the entire image to provide
% an approximate magnitude for overall flame luminosity.
Imsum = sum(cropped(:))
```

Appendix C: Spray Breakup Point

```
clc;
clear all;
close all;

%Calculate the spray breakup point from video frames to assess spray stability
%By: Meagan Sung 2/2014
sum=0;
count=0;
array=0;
total = 0;
%%% load video
mov=mmreader('F76_mass&power.avi'); %reads video file, must be in same path as .mfile
nFr = get (mov, 'numberOfFrames'); %gets the data of the properties from 'number of Frames'
pic=read(mov,15); %reads 5th frame, for test purposes
test=rgb2gray(pic);%converts image from rgb to gray scale

%%% intensity profile position
[x,y]=size(test); %defines x,y as size of matrix
x2=131; % location of line intensity
thresh = .4;
y2=6; %start point
xline=[x2,x2];
yline=[y2,x];

%%% double check location of line intensity
 imshow(test)
 hold on;
 plot(xline,yline);
 figure()
 improfile(test,xline,yline)

%%% calculation time
final_plots=zeros(1,50); %double check please, creats matrix of all 0
array=0;
startframe=10;
framecount=1;
endframe=900;
for i=startframe:framecount:endframe %must be the same as br_x!!! (line 78)
```

```matlab
        frame_1=read(mov,i);
        frame=rgb2gray(frame_1);
        sum=0;
        count=0;
% average vertical line data
        for k=1:20
            left=x2-10;
            x_position=left+k;
            xlineavg=[x_position,x_position];
            A=improfile(frame,xlineavg,yline); %improfile computes the intensity values along  line
            sum=sum+A;
%           count=count+1;
        end
%     avg_sub=sum/count; %new y values
%     avg=avg_sub/max(avg_sub); %normalization   \\\ removed
        avg=sum/max(sum); %normalize your sum matrix
        yplot=(x-length(avg)+1):x; %51:x
%     figure()
%     plot(yplot,avg)

        %determine breakup point coming from right
        y_break= length(avg); %180
        y_read=1;
            while y_read>=thresh %values that defines intensity of break up or not
            y_break=y_break-1;
            y_read=avg(y_break); % take reading from avg vector (above) at
                        % point y_break
            end
        y_read;
        y_record=y_break;
        y_final=y_record+y2; %+(number of pixels that the nosel protrudes)
        array=array+1;
        final_plots(array)=y_final;

        total = total + avg;
end
figure()
imshow(test);
hold on;
plot(x2,y_final,'x','MarkerEdgeColor','r','MarkerSize',10)

br_x=startframe:framecount:endframe;
plotavg=mean(final_plots);
plotstd=std(final_plots);
coeff=polyfit(br_x,final_plots,6);
x_coeff=linspace(min(br_x),max(br_x),200);
```

```matlab
y_coeff=polyval(coeff,x_coeff);

 %make sure this is the same as i
figure();
hold on;
plot(br_x,final_plots);
ylim([10,200]);
xlabel('Frame');
ylabel('Breakup Point from Nozzle(pixel)');
hold on;
plot(x_coeff,y_coeff);
breakup_average=mean(final_plots)

figure();
total_avg = total/endframe;
H = linspace(1,length(total_avg),length(total_avg));
plot(H,total_avg);
```

Appendix D: Combustion Efficiency Calculations

Though a number of different methods are available for calculating efficiency of the combustion process, the one selected for this report is provided below (Goodger, 1977). The selected equation for the combustion efficiency is advantageous since it only requires information on the amount of the effluents of CO and UHC. As the equation for combustion efficiency shows, reductions in the emissions of CO or UHC will translate into improvements in the overall combustion efficiency of the system. The following calculations are completed for F-76 with the following variables:

- η_C = Combustion efficiency (%)

- L_{CO} = Energy loss due to CO (%/100)

- L_{HC} = Energy loss due to HC (%/100)

- $\%CO_2$ = Measured exhaust of CO_2 (% volume) = 6.42%

- $\%CO$ = Measured exhaust of CO (% volume) = 1250.91 ppm = 0.125%

- $\%UHC$ = Measured exhaust of UHC (% volume)) = 125.21 ppm = 0.0125%

- $\%C_{FUEL}$ = Carbon in fuel (% mass) = 85.24%

- HV_{FUEL} = Lower heating value of fuel (Btu/lb) = 89041 Btu/lb

- $h_{rC/CO2}$ = Heat of reaction for C ➔ CO_2 (Btu/lb) = 14540 Btu/lb

- $h_{rC/CO}$ = Heat of reaction for C ➔ CO (Btu/lb) = 4380 Btu/lb

The heats of reaction are taken from the ASME Power Test Code 4.1, *Steam Generating Units*

The efficiency loss due to CO products is calculated with equation C-1.

$$L_{CO} = \left(\frac{\%CO}{\%CO_2 + \%CO + \%HC}\right) * \%C_{FUEL} * \left(\frac{h_{rC/CO2} - h_{rC/CO}}{HV_{FUEL}}\right) \qquad (C\text{-}1)$$

$$L_{CO} = 100 * \left[\left(\frac{0.125}{6.42 + 0.125 + 0.0125}\right) * 85.24 * \left(\frac{14540 - 4380}{89041}\right)\right] = 0.283\%$$

Efficiency losses from unburned hydrocarbon compounds is calculated via equation C-2.

$$L_{HC} = \left(\frac{\%HC}{\%CO_2 + \%CO + \%HC}\right) * \%C_{FUEL} \qquad (C\text{-}2)$$

$$L_{HC} = 100 * \left(\frac{0.0125}{6.42 + 0.125 + 0.0125}\right) * 85.24 = 0.248\%$$

Lastly, the overall efficiency can be estimated by subtracting the losses from 100% efficiency:

$$\eta_c = 100 - L_{CO} - L_{HC} \qquad (C\text{-}3)$$

$$\eta_c = 100 - 0.283 - 0.248 = 99.46\%$$

This process was repeated for each fuel using information provided by the MSGC analysis.

Appendix E: F-76 Specifications and Fuel Analysis

Test	Parameter	Method	Units	Minimum	Maximum	F-76	Algae HRD/ F-76 Blend	Pure Algae HRD F-76
Appearance at 25°C		D4176	-----	Clear & Bright		Clear & Bright	Clear & Bright	Clear & Bright
Demulsification at 25°C		D1401	minutes		10	3	2	1
Density at 15°C		D4052	kg/m3		876	830	817	776
Distillation	10% Recovered	D86	°C	Report		217	225	248
	50% Recovered		°C	Report		261	273	280
	90 % Recovered		°C		357	316	300	292
	End Point		°C		385	343	327	307
	Reside + Loss		Volume %		3	2	2.1	2
Cloud Point		D5773	°C		-1	-20	-12	-4
Color		D1500	-----		3	0.6	< 0.5	< 0.5
Flash Point		D93	°C	60		72	72	78
Particulate Contamination		D6217	mg/L		10	0.1	0.1	0.9
Pour Point		D5949	°C		-6	-30	-18	-6
Viscosity at 40°C		D445	mm2/s	1.7	4.3	2.8	2.8	2.8
Acid Number		D974	mg KOH/g		0.3	0.04	0.02	0.01
Ash		D482	Mass %		0.005	0	0	0
Carbon Residue	10% Bottom	D524	Mass %		0.2	0.18	0.04	0.04
Copper Strip Corrosion at 100 °C		D130	-----		1	1A	1A	1B
Hydrogen Content		D7171	Mass %	12.5		13.1	13.9	15.1
Ignition Quality	Cetane Index	D976	-----	43		44	60	78
Storage Stability	Total Insolubles	D5304	mg/100 mL		3	1.1	0.1	0.4
Sulfur Content		D4294	Mass %		0.5	0.1	0.1	< 0.1
Trace Metals	Ca	D7111	mg/kg		1	< 0.1	< 0.1	< 0.1
	Pb	D7111	mg/kg		0.5	< 0.1	< 0.1	< 0.1
	Na + K	D7111	mg/kg		1	< 0.1	< 0.1	< 0.1
	V	D7111	mg/kg		0.5	< 0.1	< 0.1	< 0.1